Global Distribution, Radiative Forcing, and Climate Impact of Carbonaceous Aerosols

Thesis by

Serena Hsin-Yi Chung

In Partial Fulfillment of the Requirements

for the Degree of

Doctor of Philosophy

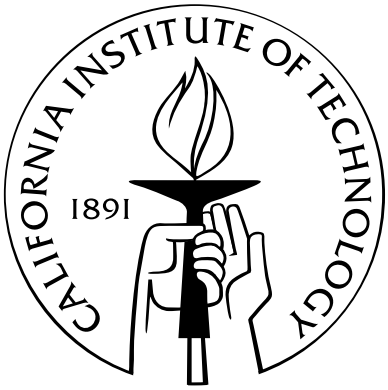

California Institute of Technology

Pasadena, California

2005

(Submitted January 19, 2005)

Acknowledgments

The past six years have been a maturing process for me both scientifically and personally. I would like to take this opportunity to express my sincere gratitude to those who have contributed along the way.

First and foremost, I would like to thank John Seinfeld for being such a wonderful advisor. He provided strong guidance but also allowed me the independence to follow my own intuition. His mentorship made the process challenging and rewarding.

The camaraderie within the entire Seinfeld research group, past and present, has made the grad school experience even more enjoyable. The computer lab with Peter Adams, Miao-Ling Lu, and Thanos Nenes was a scholarly but also cheerful environment. I am indebted to Peter for patiently helping me started on my project when I did not know anything about global modeling and for being a good sport even when I unintentionally deleted his data (more than once). Thanos welcomed me into the group and made me feel like a family member. He also inspired me to pick up my cello again. With Miao-Ling, we took this journey together and she has been a great colleague and friend. To Roya, thank you for playing "tennis" with me even though I always made you overwork. And to the rest of gang, Bill Conant, Song Gao, Melita Keywood, Brian Mader, Sally Ng, Tracey Rissmann, Tomtor Varutbangkul, and Jian Wang, thank you for all the joyful moments we had together; I particularly liked the restaurant expeditions.

I would also like to thank members of the administrative staff. Kathy Babush was tremendously resourceful that I never had to go to the graduate student office. Ann Hilgenfeldt was incredibly helpful and efficient whenever and whatever paperwork needed to be done; in addition, she always had an open door and often made an otherwise tough day brighter.

To Mom, Dad, and Ted, thank you for almost thirty years of unconditional support and encouragement. I would not have made it without you.

Finally, I would like to thank my loving husband, Tim. Your ceaseless devotion and friendship have made these years the best of my life.

Abstract

This thesis is motivated by the need to better understand and quantify the climate effects of carbonaceous aerosols, i.e., black carbon (BC) and organic carbon (OC). Global three-dimensional distribution of carbonaceous aerosols is simulated online in a general circulation model (GCM). The carbonaceous aerosol model includes primary BC, primary OC, five groups of biogenic volatile organic compounds (BVOCs), and fourteen semi-volatile products of BVOC oxidation by O_3, OH, and NO_3, which condense to form secondary organic aerosols (SOAs) based on an equilibrium partitioning model. Human activities since the preindustrial period are predicted to have increased global burdens of BC and OC by an order of magnitude and almost tripled the SOA production rate. Based on an older emission inventory for BC, the direct radiative forcing of increased atmospheric BC burden is estimated to warm the atmosphere by 0.51 to 0.8 W m^{-2}, depending on how BC is mixed with other tropospheric aerosols. For OC , the estimated anthropogenic direct radiative forcing at top of the atmosphere (TOA) is -0.1 to -0.2 W m^{-2}, depending on the water-uptake property of OC. When BC, OC and sulfate are combined, the estimated direct radiative forcing at TOA is -0.39 to -0.78 W m^{-2}. Using an updated emission inventory, direct radiative forcing of anthropogenic BC at TOA is estimated to be +0.33 and +0.6 W m^{-2}, for BC mixed externally and internally with present-day level of sulfate, respectively. Using a GCM coupled to a mixed-layer ocean model, these estimated forcings for BC are

predicted to warm surface air temperature by 0.2 to 0.37 K. The temperature increase is the largest over northern high latitutdes during winter and early spring. Even though the predicted global-averaged warming due to BC is less than that of greenhouse gases, significant regional differences do exist, such as substantial warming in central and eastern Russia predicted for BC. In addition to temperature increase, direct radiative forcing of anthropogenic BC is also predicted to lead to a change in the hydrological cycle by shifting the intertropical convergence zone northward.

.

Contents

List of Figures

List of Tables

Chapter 1

Preface

1.1 Introduction

In the past, studies have shown that airborne particulate matter, or aerosols, is an important component of the earth's climate system. One mechanism by which tropospheric aerosols affect the climate is by direct interaction with solar radiation. Aerosols can cool the atmosphere by scattering incoming solar radiation back to space, or they can warm the atmosphere by absorbing solar radiation. The scattering or absorbing of solar radiation is termed direct radiative effect. In contrast to greenhouse gases (GHGs), which warm the atmosphere by trapping outgoing infrared radiation, most tropospheric aerosols are too small in size to affect longwave radiation.

Since the preindustrial period, anthropogenic activities have increased the atmospheric abundance of aerosols. The increase is estimated to make significant contributions to perturbing the radiative energy balance of the earth-atmosphere system. The magnitude of the radiative perturbation is termed radiative forcing, which is the first-order estimate of the climate impact. By convention, positive radiative forcing indicates a tendency to warm the atmosphere. Figure 1.1 shows the estimated radiative forcing of various atmospheric constituents. Even though Figure 1.1 indicates that the radiative forcings of GHGs and

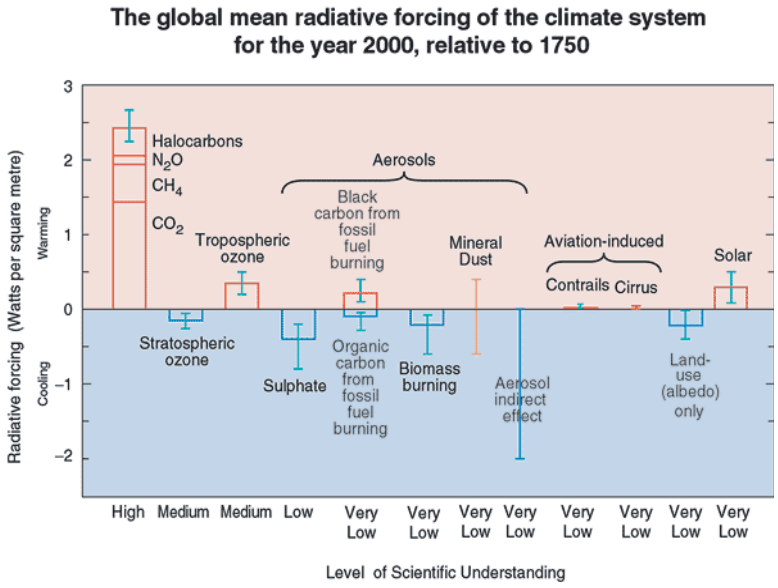

Figure 1.1: Estimated anthropogenic contribution to global and annual mean radiative forcing (W m^{-2}) of various atmospheric constituents. Reference: *The Third Assessment Report of the Intergovernmental Panel on Climate Change (IPCC)* [2001].

aerosols more or less cancel each other, the global-averaged cancellation is misleading given that the spatial patterns of GHG forcing and those of aerosol forcing are very different. Because GHGs have long atmospheric lifetimes, their spatial and temporal distributions are relatively uniform. Tropospheric aerosols, however, have lifetimes on the order of one week, and their distribution is inhomogeneous. Even if global-averaged radiative forcing of aerosols is small, regional effects are important. Figure 1.1 also indicates that the level of scientific understanding for tropospheric aerosols is very low, in comparison to high for GHGs.

There are two classes of tropospheric aerosols that are predominantly anthropogenic in origin: sulfate and carbonaceous aerosols. Sulfate aerosols are purely scattering, and therefore their direct radiative effect is to cool the atmosphere. Carbonaceous aerosols are more complicated in that they both scatter and absorb solar radiation. Of the two, climate impact of the direct radiative effect of the former has been studied more extensively.

Much less is understood about the climate impact of carbonaceous aerosols. Improved understanding of the radiative and climate effects of carbonaceous aerosols is important to the larger goal of determining the impact of anthropogenic activities on global climate.

Carbonaceous particles consist of a complex mixture of organic compounds with low content of hydrogen and oxygen. They are usually divided into two categories: black carbon (BC) and organic carbon (OC). BC (or soot) is the main light-absorbing component of atmospheric aerosols and has similar properties as graphitic carbon. In contrast, aerosol organic carbon represents an aggregate of hundreds of individual compounds with a wide range of chemical and thermodynamic properties. The only source of atmospheric BC is direct emission from combustion of fossil fuel and biomass burning. In addition to being emitted directly from fossil fuel combustion or biomass burning, organic carbon aerosols can also be formed in the atmosphere as products of gas-phase oxidation of volatile organic compounds (VOCs). These organic aerosols are labeled secondary organic aerosols (SOAs).

Given the nature of their origins, anthropogenic activities, such as increased fossil fuel usage, lead to increase in atmospheric concentrations of primary BC and OC. For SOAs, even though most of the precursor VOCs are biogenic in origin, anthropogenic activities can still lead to increased atmospheric concentrations of SOAs by increasing concentrations of oxidants, such as ozone, that react with VOCs and by increasing emission of primary OC, which serves as a medium to absorb more of the oxidation products into the aerosol phase.

1.2 Organization of Thesis

The motivation of this thesis is to improve the understanding of the global distribution and the climate impact of anthropogenic carbonaceous aerosols. As mentioned earlier, distributions of carbonaceous aerosols are spatially and temporally inhomogeneous due to

their short atmospheric lifetimes. The first part of Chapter 2 is focused on the online simulation of global three-dimensional distributions of carbonaceous aerosols in a general circulation model (GCM). The focus of second half of Chapter 2 is to use the predicted distributions from the first part to estimate the direct radiative forcing of carbonaceous aerosols. Given the relatively large direct radiative forcing of BC, Chapter 3 studies the climate impact due to direct radiative forcing of anthropogenic BC. Finally, a summary of the thesis is presented in Chapter 4.

Chapter 2

Global Distribution and Climate Forcing of Carbonaceous Aerosols

Reference: Chung, S. H., and J. H. Seinfeld, (2002), Global distribution and climate forcing of carbonaceous aerosols, *J. Geophy. Res.*, 107(D19),4407,doi:10.1029/2001JD001397.

2.1 Abstract

The global distribution of carbonaceous aerosols is simulated online in the Goddard Institute for Space Studies general circulation model II-prime (GISS GCM II-prime). Prognostic tracers include black carbon (BC), primary organic carbon (POA), five groups of biogenic volatile organic compounds (BVOCs), and fourteen semi-volatile products of BVOC oxidation by O_3, OH, and NO_3, which condense to form secondary organic aerosols (SOA) based on an equilibrium partitioning model and experimental observations. Estimated global burdens of BC, POA, and SOA are 0.21, 1.2, and 0.19 Tg with lifetimes of 6.4, 5.3 and 6.3 days, respectively. The predicted global production of SOA is 11.2 Tg yr^{-1}, with 91% due to O_3 and OH oxidation. Globally averaged, top of the atmosphere (TOA) radiative forcing by anthropogenic BC is predicted as +0.51 to +0.8 W m^{-2}, the former being for BC in

an external mixture and the latter for BC in an internal mixture of sulfate, OC, and BC. Globally averaged, anthropogenic BC, OC, and sulfate are predicted to exert a TOA radiative forcing of -0.39 to -0.78 W m^{-2}, depending on the exact assumptions of aerosol mixing and water uptake by OC. Forcing estimates are compared with those published previously.

2.2 Introduction

Anthropogenic-induced changes in the atmospheric abundance of tropospheric greenhouse gases and aerosols are estimated to make significant contributions to climate change over the next century [*Intergovernmental Panel on Climate Change (IPCC)*, 2001]. A number of studies have focused on the global distribution of sulfate aerosols [*Langner and Rodhe*, 1991; *Luecken et al.*, 1991; *Penner et al.*, 1994; *Benkovitz et al.*, 1994; *Chin et al.*, 1996; *Feichter et al.*, 1996; *Pham et al.*, 1996; *Roelofs et al.*, 1998; *Adams et al.*, 1999; *Lohmann et al.*, 1999; *Koch et al.*, 1999; *Barth et al.*, 2000; *Rasch et al.*, 2000] and their direct radiative forcing [*Charlson et al.*, 1991; *Kiehl and Briegleb*, 1993; *Taylor and Penner*, 1994; *Chuang et al.*, 1997; *Feichter et al.*, 1997; *Penner et al.*, 1997, 1998; *Koch et al.*, 1999; *Kiehl et al.*, 2000; *Tegen et al.*, 2000; *Adams et al.*, 2001]; fewer corresponding global three-dimensional studies of carbonaceous aerosols exist [*Liousse et al.*, 1996; *Cooke and Wilson*, 1996; *Penner et al.*, 1998; *Cooke et al.*, 1999; *Kanakidou et al.*, 2000]. Several studies have addressed the direct radiative forcing of carbonaceous aerosols [*Haywood and Shine*, 1995; *Haywood et al.*, 1997; *Schult et al.*, 1997; *Haywood and Ramaswamy*, 1998; *Myhre et al.*, 1998; *Penner et al.*, 1998; *Jacobson*, 2000; *Tegen et al.*, 2000; *Jacobson*, 2001a,b; *Koch*, 2001].

Carbonaceous particles consist of a complex mixture of chemical compounds. Such particles are usually divided into two fractions, black (or elemental) carbon (BC) and organic carbon (OC). Black carbon is a strong absorber of visible and near-IR light; therefore,

black carbon concentrations are traditionally determined by light-absorption measurements of particles collected on filters [*Lindberg et al.*, 1999]. In contrast, aerosol organic carbon represents an aggregate of hundreds of individual compounds with a wide range of chemical and thermodynamic properties, making concentration measurements difficult using any single analytical technique. Instead, aerosol OC content is usually determined from the difference between total carbon and black carbon contents [*Turpin et al.*, 2000].

Organic carbon can be emitted directly into the atmosphere as products of fossil fuel combustion or biomass burning. This is called primary organic aerosol (POA). By contrast, secondary organic aerosol (SOA) is formed in the atmosphere as the oxidation products of certain volatile organic compounds (VOCs) condense on pre-existing aerosols. Both anthropogenic and biogenic VOCs can lead to SOA; on a global scale, biogenic hydrocarbons are estimated to be the predominant source (except isoprene, which does not form aerosol upon oxidation [*Pandis et al.*, 1991]). Experimental studies indicate that the aerosol yield (ratio of the mass of SOA formed to that of VOC reacted) exhibits a wide range of values for different parent hydrocarbons [*Hoffmann et al.*, 1997; *Odum et al.*, 1997; *Griffin et al.*, 1999b,a].

Among global modeling studies on carbonaceous aerosols, only *Liousse et al.* [1996], *Griffin et al.* [1999a], and *Kanakidou et al.* [2000] have considered SOA. *Liousse et al.* [1996] estimated the global burden of SOA by assuming a constant aerosol yield of 5% for all biogenic species. On the basis of compound-specific, laboratory-derived aerosol yields, *Griffin et al.* [1999b] estimated the global production of biogenic SOA to lie in the range of 13-24 Tg yr^{-1}, but their work did not directly employ a global three-dimensional transport model and did not include explicit calculation of the gas-particle partitioning of SOA into POA. *Kanakidou et al.* [2000] used a global chemical transport model with α- and β-pinene

as representative of all biogenic hydrocarbons and considered only oxidation of the pinenes by O_3 as a source of SOA. While they allowed for the partition of semi-volatile oxidation products into the organic aerosol phase, they did not include transport of semi-volatile products that remain in the gas phase. *Kanakidou et al.* [2000] estimated the production of SOA to be 17-28 Tg yr^{-1} for preindustrial times and 61-79 Tg yr^{-1} for present day. One issue, therefore, is understanding the relatively large discrepancy between the global SOA production estimates of *Griffin et al.* [1999b] and *Kanakidou et al.* [2000].

In this work, we simulate the three-dimensional, global distribution of present-day and preindustrial carbonaceous aerosols, including BC, POA, and SOA. Oxidation of the five most important classes of biogenic hydrocarbons by O_3, OH, and NO_3 is included to account for the different aerosol yield potentials of the reaction products of the parent molecules. The global distributions of BC, POA, and SOA are then used to estimate annual direct radiative forcing by all three classes of carbonaceous aerosols. Previous work has shown that the direct radiative forcing of aerosol BC depends importantly on the manner in which that BC is mixed with non-absorbing aerosols such as sulfate (e.g., *Jacobson* [2000]; *Myhre et al.* [1998]; *Haywood et al.* [1997]). Therefore, effects of the mixing state of the aerosol are considered.

2.3 Model Description

Three-dimensional global transport of tracers is simulated on-line in the Goddard Institute for Space Studies General Circulation Model II-prime (GISS GCM II-prime) [*Hansen et al.*, 1983; *Rind and Lerner*, 1996], together with imported fields of OH (C. Spivakovsky personal communication, 1998) , O_3, and NO_3 [*Wang et al.*, 1998a].

2.3.1 Tracer Model

The model includes a total of 37 prognostic species as tracers: 4 classes of primary carbonaceous aerosols, 5 reactive hydrocarbon groups, and 28 organic oxidation products.

2.3.1.1 Primary carbonaceous aerosols

Black carbon (BC) and primary organic aerosol (POA) are included as tracers in the model. For the purpose of representing wet scavenging, each of these two classes of aerosol is divided into hydrophobic and hydrophilic categories, for a total of 4 primary carbonaceous aerosol classes. Increased solubility of carbonaceous particles is generally considered to result from coating of the aerosol by soluble species such as sulfuric acid or sulfate. Accurate modeling of solubility would require knowledge of the rate at which ambient carbonaceous aerosols acquire a coating of hydrophilic material and also the hygroscopic behavior of the resulting particles, information that is not generally available. In the absence of such information, we adopt the estimate from *Cooke et al.* [1999], that ambient conversion of carbonaceous aerosol from hydrophobic to hydrophilic occurs with an exponential decay lifetime of 1.15 days.

2.3.1.2 Reactive hydrocarbons

In order to represent the formation of SOA, the parent hydrocarbons that, upon atmospheric oxidation, lead to semi-volatile products that form aerosol must be included as tracers in the model. Hydrocarbons with potential to form aerosols include monoterpenes and sesquiterpenes, which are biogenic in origin, as well as aromatics, long-chain carbonyls, and high-molecular weight alkenes, all of which are predominantly anthropogenic. Based on measured aerosol yield parameters [*Wang et al.*, 1992; *Hoffmann et al.*, 1997; *Odum et al.*,

Table 2.1: Classes of Reactive Terpenes

Hydrocarbon class	Composition
I	α-pinene, β-pinene, sabinene, Δ^3-carene, terpenoid ketones
II	limonene
III	α-terpinene, γ-terpinene, terpinolene
IV	myrcene, terpenoid alcohols, ocimene
V	sesquiterpenes

1997; *Griffin et al.*, 1999b,a], reaction rate constants with O_3, OH, and NO_3 [*Atkinson*, 1994; *Atkinson et al.*, 1995; *Shu and Atkinson*, 1995; *Atkinson*, 1997], and estimated global emissions [*Piccot et al.*, 1992; *Guenther et al.*, 1995; *Griffin et al.*, 1999b], only hydrocarbons of biogenic origin are found to contribute significantly to global SOA formation. Table 2.1 lists the reactive hydrocarbons included as tracers, grouped into five categories according to the values of their experimentally-measured aerosol yield parameters [*Griffin et al.*, 1999a]. Because of lack of explicit experimental data, aerosol yield parameters of terpenoid ketones are assumed, because of their structural similarities, to be the same as those of sabinenes.

2.3.2 Oxidation Products

While explicit molecular product identification of secondary organic aerosols has shown that the number of products formed for each reaction can be large [*Yu et al.*, 1999; *Calogirou et al.*, 1999], *Hoffmann et al.* [1997] and *Griffin et al.* [1999a] have shown that a two-product model is sufficient for the purpose of representing experimentally observed SOA yields. Because the contributions of O_3 and OH oxidation to SOA formation cannot generally be separated experimentally, oxidation by O_3 and OH is considered together for the purpose of assigning aerosol products. Because of lack of experimental data on NO_3 oxidation for all the terpenes, NO_3 oxidation of β-pinene is used to represent NO_3 oxidation of all hydrocarbons; in this case, a one-product model is sufficient [*Griffin et al.*, 1999a].

For each of the first four primary reactive hydrocarbons listed in Table 2.1, there are therefore three oxidation products, two for combined O_3 and OH oxidation and one for NO_3 oxidation. In the case of sesquiterpenes, only two products are required (one for combined O_3 and OH oxidation and one for NO_3 oxidation)[*Griffin et al.*, 1999b,a]. All products are semi-volatile and partition between the gas and aerosol phases; consequently, each product requires two tracers, one gas-phase and one aerosol-phase, for a total of 28 tracers in this group.

2.3.3 Gas-Phase Chemistry and SOA Formulation

The chemical representation of SOA formation is based on *Hoffmann et al.* [1997] and *Griffin et al.* [1999a]. A parent hydrocarbon, HC_i, reacts in the gas phase with an oxidant, OX_j, either OH, O_3, or NO_3, to form a set of products, $G_{i,j,k}$,

$$HC_i + OX_j \longrightarrow \alpha_{i,j,1}G_{i,j,1} + \alpha_{i,j,2}G_{i,j,2} + \cdots$$

where $\alpha_{i,j,k}$'s are mass-based stoichiometric coefficients. Monthly-average three-dimensional O_3 and NO_3 fields are imported from the Harvard Chemical Transport Model (CTM) [*Wang et al.*, 1998a,b,c]. Three-dimensional fields of 5-day average OH radical concentrations are from C. Spivakovsky (personal communication, 1998). To account for the diel variation in OH and O_3 concentrations, the instantaneous value is obtained by scaling with the cosine of the solar zenith angle. Daily NO_3 concentrations are converted from monthly averages based on the number of dark hours during the day and are considered to be nonzero only during hours of no sunlight.

Group-averaged reaction rate constants for O_3, OH, and NO_3 oxidation are listed in

Table 2.2: Reaction Rate Constants for Hydrocarbon Oxidation (cm^3 $molecule^{-1}$ s^{-1} at 298 K)

Hydrocarbon class	$k_{O_3} \times 10^{18}$	$k_{OH} \times 10^{12}$	$k_{NO_3} \times 10^{12}$
I	56	84	7
II	200	171	12
III	7700	255	89
IV	423	199	15
V	11650	245	27

Sources: *Atkinson et al.* [1995], *Shu and Atkinson* [1995], *Atkinson* [1997]. Rate constants for each hydrocarbon class are computed based on the arithmetic mean for the compounds listed in Table 2.1. The temperature dependence of reaction rate constants is given by

$$\frac{k(T_2)}{k(T_1)} = \exp\left[-\frac{E}{R}\left(\frac{1}{T_2} - \frac{1}{T_1}\right)\right]$$

where T_1 and T_2 are temperatures in K, E is the activation energy, and R is the ideal gas constant. In the absence of explicit activation energy data for all the individual hydrocarbons, E/R for the oxidation of α-pinene is used for all hydrocarbons: 732 K, -400 K, and -490 K for O_3, OH, and NO_3 reactions, respectively [*Atkinson*, 1994].

Table 2.2. β-Caryophyllene and α-humulene are used to represent all sesquiterpenes. Laboratory-derived values for the mass-based stoichiometric coefficients $\alpha_{i,j,k}$ are listed in Table 2.3. Again, for each reactive hydrocarbon group, the stoichiometric coefficient is taken as the arithmetic average of the values of the compounds in that group, as listed in Table 2.1. Properties of β-caryophyllene and α-humulene are used to represent those of all sesquiterpenes.

Once formed in the gas phase, the semi-volatile reaction products $G_{i,j,k}$ will partition between the gas and aerosol phases. We consider this partitioning to occur to the entire organic aerosol phase. Particles will generally contain some water, and water-soluble organic compounds do parition to the aqueous portion of the aerosol as well [*Seinfeld et al.*, 2001]; however, we do not consider that process here. This should not lead to an appreciable error

Table 2.3: Mass-based Stoichiometric Coefficients for Semi-Volatile Products from the Oxidation of Hydrocarbons

Hydrocarbon class	O_3+OH oxidation		NO_3 oxidation[a]
	$\alpha_{i,1,1}$	$\alpha_{i,1,2}$	$\alpha_{i,2,1}$
I	0.067	0.354	1.0
II	0.239	0.363	1.0
III	0.069	0.201	1.0
IV	0.067	0.135	1.0
V	1.0		1.0

[a] Based on value of β-pinene for all compounds.
Sources: *Griffin et al.* [1999a,b]. Stoichiometric coefficients for each hydrocarbon class are computed based on the arithmetic mean for the compounds listed in Table 2.1.

in estimating global SOA formation. The fraction of each product that partitions to the organic aerosol phase is governed by an equilibrium partition coefficient $K_{om,i,j,k}$ [*Pankow*, 1994a,b],

$$[\mathrm{G}]_{i,j,k} = \frac{[\mathrm{A}]_{i,j,k}}{K_{om,i,j,k} M_o} \tag{2.1}$$

where $[\mathrm{G}]_{i,j,k}$ is the product concentration in the gas phase, $[\mathrm{A}]_{i,j,k}$ is the product concentration in the aerosol phase, and M_o is the concentration of total organic aerosol, i.e.,

$$M_o = [\mathrm{POA}] + \sum_{i,j,k} [\mathrm{A}]_{i,j,k} \tag{2.2}$$

where [POA] is the concentration of primary organic aerosol. The partition coefficients $K_{om,i,j,k}$ corresponding to $\alpha_{i,j,k}$ in Table 2.3 are listed in Table 2.4.

The partition coefficient can be expressed as follows [*Pankow*, 1994b]:

$$K_{om,i,j,k} = \frac{760 RT}{10^6 M_o \zeta_{i,j,k} p^0_{L,i,j,k}} \tag{2.3}$$

where $\zeta_{i,j,k}$ is the activity coefficient of compound $\mathrm{G}_{i,j,k}$ in the organic aerosol phase, and

Table 2.4: Equilibrium Gas-Particle Partition Coefficients of Semi-Volatile Compounds (m^3 μg^{-1})

Hydrocarbon	O_3+OH oxidation		NO_3 oxidation[a]
	$K_{om,i,1,1}$	$K_{om,i,1,2}$	$K_{om,i,2,1}$
I	0.184	0.0043	0.0163
II	0.055	0.0053	0.0163
III	0.133	0.0035	0.0163
IV	0.224	0.0082	0.0163
V	0.0459		0.0163

[a] Based on value of β-pinene for all compounds.
Sources: *Griffin et al.* [1999a,b]. Partition coefficients for each hydrocarbon class are computed based on the arithmetic mean for the compounds listed in Table 2.1.

$p^0_{L,i,j,k}$ (torr) is the vapor pressure of the compound at the temperature of interest (subcooled, if necessary). Using the Clausius-Clapeyron equation and assuming that $\zeta_{i,j,k}$ is constant, the temperature dependence of $K_{om,i,j,k}$ is given by

$$\frac{K_{om,i,j,k}(T_2)}{K_{om,i,j,k}(T_1)} = \frac{T_2}{T_1} \exp\left[\frac{\Delta H_{i,j,k}}{R}\left(\frac{1}{T_2} - \frac{1}{T_1}\right)\right] \tag{2.4}$$

where $\Delta H_{i,j,k}$ is the enthalpy of vaporization. From the *CRC Handbook of Chemistry and Physics* [*Lide*, 2001], $\Delta H/R \approx 5 \times 10^3$ K for organic compounds, and this value is used for all compounds considered. This value translates into a range of values of $K_{om,i,j,k}$ over about 3 orders of magnitude for tropospheric temperatures.

As gas-phase reaction proceeds in each GCM grid cell, the semi-volatile products repartition to establish equilibrium over a GCM time step. Using Equation 2.1 and mass balance on each product, M_o can be determined from

$$\sum_{i,j,k}\left[\frac{K_{om,i,j,k}\left(\alpha_{i,j,k}\Delta \mathrm{HC}_{i,j} + [\mathrm{A}]^o_{i,j,k} + [\mathrm{G}]^o_{i,j,k}\right)}{(1 + K_{om,i,j,k}M_o)}\right] + \frac{[\mathrm{POA}]}{M_o} = 1 \tag{2.5}$$

where $\Delta\mathrm{HC}_{i,j}$ is the concentration of hydrocarbon i that reacts with oxidant j, over the time step and $[\mathrm{A}]^o_{i,j,k}$ and $[\mathrm{G}]^o_{i,j,k}$ are the gas- and aerosol-phase concentrations at the beginning of the time step. The left hand side of Equation 2.5 is a monotonically decreasing function of M_o. If [POA]=0, for example, and

$$\sum_{i,j,k} \left[K_{om,i,j,k} \left(\alpha_{i,j,k} \Delta\mathrm{HC}_{i,j} + [\mathrm{A}]^o_{i,j,k} + [\mathrm{G}]^o_{i,j,k} \right) \right] < 1 \tag{2.6}$$

then $M_o = 0$, and all products stay in the gas phase. Otherwise, M_o is determined implicitly from Equation 2.5, and $[\mathrm{A}]_{i,j,k}$ is determined by

$$[\mathrm{A}]_{i,j,k} = \frac{K_{om,i,j,k} M_o \left(\alpha_{i,j,k} \Delta\mathrm{HC}_{i,j} + [\mathrm{A}]^o_{i,j,k} + [\mathrm{G}]^o_{i,j,k} \right)}{(1 + K_{om,i,j,k} M_o)} \tag{2.7}$$

Then, $[\mathrm{G}]_{i,j,k}$ is obtained from Equation 2.1.

2.3.4 Emissions

Anthropogenic emissions of carbonaceous aerosols are mainly from fossil fuel and biomass burning. Monthly emissions of black carbon and primary organic aerosols are taken from the emission IPCC scenario A2 for the year 2000. Emissions are based on the work of *Liousse et al.* [1996] for biomass POA and BC and fossil fuel POA and the work of *Penner et al.* [1993] for fossil fuel BC. Globally averaged, 45% of BC and 55% of POA emitted are from fossil fuel burning. Annual emissions are shown in Figures 2.1 and 2.2. Of the total black carbon emitted, 80% is assumed to be hydrophobic, while 50% of the primary organic aerosol is assumed be to hydrophobic; the remaining portions are assumed to be hydrophilic [*Cooke et al.*, 1999].

While *Liousse et al.* [1996] provide the only inventory of carbonaceous aerosols from

biomass burning, other emission inventories of carbonaceous aerosols from fossil fuel are also available, including those of *Cooke and Wilson* [1996] (BC), *Cooke et al.* [1999] (BC and POA), and *Bond* [2000] (BC). The emission inventory we use is that designated as IPCC scenario A2 for the year 2000. The emission factors, which relate the mass of fuel burned to mass of aerosol emitted, vary by several orders of magnitude for different fuel types and burning efficiency and are highly uncertain. The BC inventory for fossil fuel used here from the work of *Penner et al.* [1993] is approximately a quarter of the emissions given by *Cooke and Wilson* [1996] and about half of those of *Cooke et al.* [1999] and *Bond* [2000] for North America. Primary emission of OC from fossil fuel is even more uncertain, as the OC inventory is inferred from the BC inventory. Also, the inventory used here was developed using data from the Food and Agriculture Organization for 1980 [*Liousse et al.*, 1996], and increases in emissions would have occurred since then.

Global monthly emission inventories of total monoterpenes and other reactive volatile organic compounds (ORVOCs) from biogenics are obtained from the Global Emissions Inventory Activity (GEIA) and are based on the work of *Guenther et al.* [1995]. Global annual emission distributions are shown in Figures 2.3 and 2.4. By determining the predominant plant species associated with the ecosystem types and the specific monoterpene and ORVOC emissions from these plant species, the contributions of individual compounds can be estimated. The percent contribution of each compound to total monoterpene and ORVOC emissions is reported in *Griffin et al.* [1999b] and is assumed to be constant geographically. Emissions of monoterpenes and ORVOCs vary diurnally as emission rates change with the light and leaf temperature [*Guenther et al.*, 1995]. For simplicity, to obtain the instantaneous emission rate of biogenic hydrocarbons, monthly averages are scaled by the solar zenith angle. A summary of emissions used in the current work is given in Table 2.5.

Table 2.5: Estimated Annual Emissions of SOA Precursors, POA, and BC

Tracer	Compound	Emission (Tg yr^{-1})
I[a]		109
	α-Pinene	50
	β-Pinene	33
	Sabinene and Terpenoid Ketones	20
	$^3\Delta$-Carene	6
II[a]	Limonene	33
III[a]		4.3
	α- and γ-Terpinene	1.4
	Terpinolene	2.9
IV[a]		40
	Myrcene	7
	Terpenoid Alcohols	30
	Ocimene	3
V[a]	Sesquiterpenes	15
POA[b]		81
BC[b,c]		12

[a] *Guenther et al.* [1995]; *Griffin et al.* [1999b].
[b] *Liousse et al.* [1996].
[c] *Penner et al.* [1993].

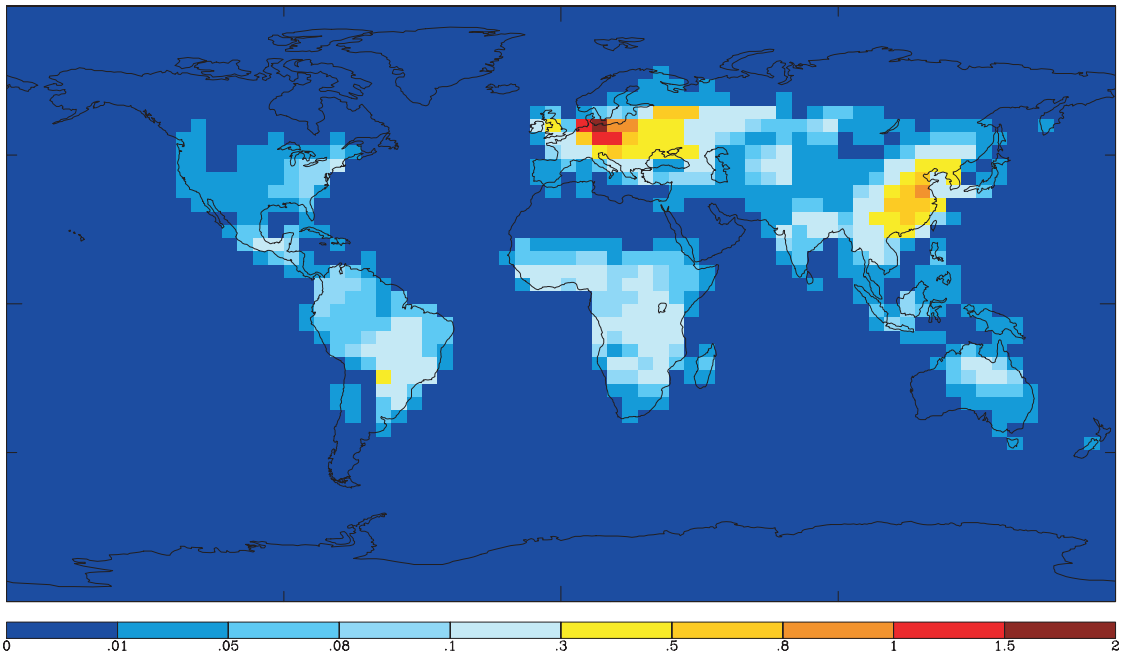

Figure 2.1: Estimated annual black carbon emissions (g C m^{-2}) [*Liousse et al.*, 1996; *Penner et al.*, 1993].

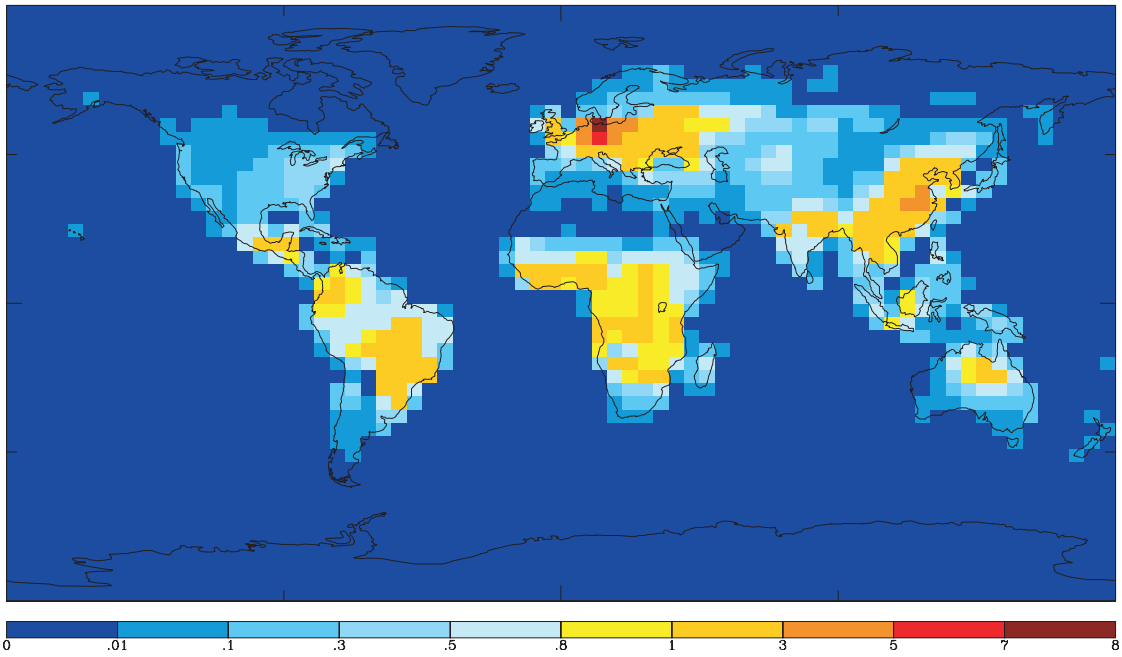

Figure 2.2: Estimated primary organic carbon emissions (g C m^{-2}) [*Liousse et al.*, 1996].

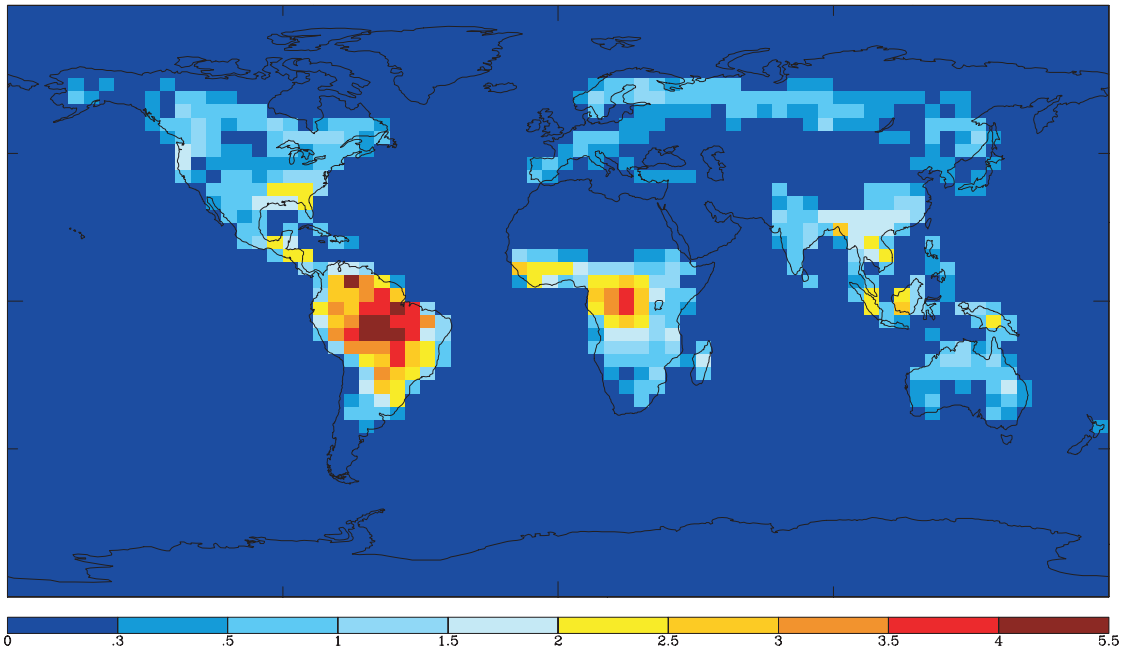

Figure 2.3: Estimated annual monoterpene emissions (g C m^{-2}) [*Guenther et al.*, 1995].

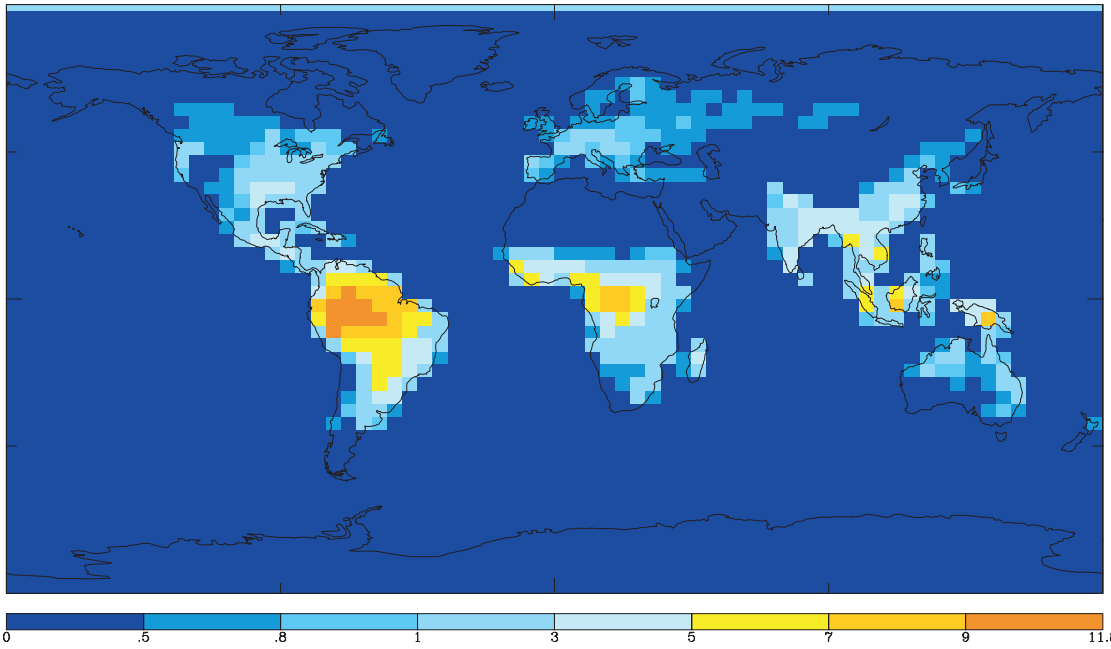

Figure 2.4: Estimated annual emissions of natural ORVOCs (g C m^{-2}) [*Guenther et al.*, 1995].

2.3.5 GISS GCM II-Prime

Tracer processes are handled online in the Goddard Institute for Space Studies General Circulation Model II-prime (GISS GCM II-prime) [*Hansen et al.*, 1983; *Rind and Lerner*, 1996]. Recent improvements relevant to the GISS GCM II-prime are discussed by *Rind and Lerner* [1996]. The resolution is 4° latitude by 5° longitude, with nine σ layers in the vertical direction, from the surface to 10 mbar. The vertical layers are centered approximately at 959, 894, 786, 634, 468, 321, 201, 103, and 27 mbar. The model surface layer is 50 mbar thick. The top one or two layers are situated in the stratosphere. The boundary layer parameterization uses a new scheme that incorporates a finite modified Ekman layer [*Hartke and Rind*, 1997]. The dynamic time step for tracer processes is 1 hour. The GCM utilizes a fourth-order scheme for momentum advection. Tracers, heat, and moisture are advected each time step by the model winds using the quadratic upstream scheme, which

is mathematically equivalent to the second-order moment method of *Prather* [1986].

2.3.5.1 Wet deposition

Wet deposition of dissolved tracers generally follows the GCM treatment of liquid water, which is described by *Del Genio and Yao* [1993] and *Del Genio et al.* [1996]. The GCM distinguishes between large-scale (stratiform) and convective clouds. During in-cloud scavenging, gas-phase species dissolve into cloud water according to their Henry's law coefficients (Table 2.6), and aerosol-phase species dissolve according to their scavenging efficiencies [*Koch et al.*, 1999]. When data are available, Henry's law coefficients for the SOA precursor hydrocarbons represent averages for species in that group. Since the Henry's law coefficients for the parent hydrocarbons are relatively small, wet scavenging of these species proves to be insignificant. Indeed, the dominant sink for the reactive hydrocarbons is oxidation by O_3, OH, and NO_3. Biogenic hydrocarbon oxidation products are expected to consist of multi-functional oxygenated compounds with a large fraction being carboxylic acids and dicarboxylic acids [*Saxena and Hildemann*, 1996; *Calogirou et al.*, 1999]. From the compilation of Henry's law coefficients by *Sander* [1999], $H \approx 10^3 - 10^4$ M atm^{-1} for carboxylic acids, and $H \approx 10^6 - 10^8$ M atm^{-1} for dicarboxylic acids; therefore, 10^5 M atm^{-1} is a reasonable value to represent those of the gas-phase products. By similar reasoning, $\Delta H_A/R = -12$ K is used to represent the temperature dependence of H:

$$\frac{d \ln H}{dT} = \frac{\Delta H_A}{RT^2} \tag{2.8}$$

where ΔH_A is the heat of dissolution. Temperature dependence of Henry's law coefficients need not be considered for the reactants.

Hydrophobic aerosols are assumed to be insoluble; hydrophilic aerosols are assumed to be infinitely soluble. For secondary organic aerosols, 80% are assumed to dissolve into clouds, consistent with findings of *Limbeck and Puxbaum* [2000].

Transport of dissolved chemical tracers follows the convective air mass transport, and scavenging is applied only to species within or below the cloud updraft. Moist convection includes a variable mass flux scheme determined by the amount of instability relative to the wet adiabat, two plumes, one entraining and one non-entraining, as well as compensating subsidence and downdrafts [*Del Genio and Yao*, 1993]. All liquid water associated with convective clouds either precipitates, evaporates, or detraines within the 1-hour GCM time step, and the dissolved chemical tracers are either deposited (in case of precipitation) or returned to the air (in case of evaporation or detrainment) in corresponding proportions. All water condensed above a certain level (typically 550 mbar) is detrained into cirrus anvils and added to the large-scale cloud liquid water content, which is carried as a prognostic variable in the GCM. For large-scale, in-cloud scavenging, tracers are re-dissolved into cloud water (using Henry's law coefficients or scavenging efficiencies) and scavenged according to a first-order rate loss parameterization that depends on the rate of conversion of cloud into rainwater. Below both types of clouds, aerosols and soluble gases are scavenged according to a first-order parameterization that depends on the amount of precipitation [*Koch et al.*, 1999]. Dissolved tracer is returned to the atmosphere if precipitation from either type of cloud evaporates.

2.3.5.2 Dry deposition

Dry deposition of all gas-phase species is based on a resistance-in-series parameterization [*Wesely and Hicks*, 1977]. Aerodynamic resistances are computed as a function of

Table 2.6: Henry's Law Coefficients for Gas-Phase SOA Parent Hydrocarbons and Oxidation Products

Tracer	H (M atm^{-1}) @ 298 K	Reference
I	0.023	*Falk et al.* [1990]; *Li et al.* [1998] *Sander* [1999]
II	0.07	*Falk et al.* [1990]
III	0.067	*Li et al.* [1998]
IV	54	*Li et al.* [1998]
V[a]	0.049	*Sander* [1999]
oxidation products[b]	10^5	*Sander* [1999]

[a] Using value of β-pinene.
[b] See text for explanation.

GCM surface momentum and heat fluxes. Surface resistances are scaled to the resistance of SO_2, which is parameterized as a function of local surface type, temperature, and insolation [*Wesely*, 1989]. The scaling uses the Henry's law coefficients in Table 2.6, ratio of molecular diffusivities of the species in air to that of water vapor (estimated using the ratios of molecular weights), and a surface reactivity factor f_0. All tracers are assumed to be nonreactive at the surface; therefore, $f_0 = 0$. For all aerosols, the deposition velocity of 0.1 cm s^{-1} is used [*Liousse et al.*, 1996].

2.4 Simulated Global Distributions of BC, POA, and SOA

This section presents simulated aerosol concentration fields. We also present comparisons to observations and previous work. The GCM predictions are averaged over a three year perdiod after 11 months of initial spin-up.

2.4.1 Global Distributions and Lifetimes

Figure 2.5 shows the predicted annual global distributions of BC, POA, and SOA. Distributions of BC and POA exhibit maxima near source regions over the continents,

especially in Europe and eastern Asia. The transport of biomass burning aerosols from tropical Africa and South America to the Atlantic and Pacific Oceans, respectively, is also evident. On average, the BC burden is predicted to be about 10 times larger in the Northern Hemisphere (NH) than in the Southern Hemisphere (SH) because of the predominance of fossil fuel sources. For the same reason, NH abundance of POA is also about 10 times as large as that in the SH. SH POA is dominated by biomass burning sources in South America and Africa, whereas NH POA is dominated by fossil fuel emissions in the US, Europe, and eastern Asia, as well as biomass burning in the former U.S.S.R. Surface concentrations of SOA follow similar trends to those of POA, since regions of high biogenic emissions tend to overlap with regions of high concentrations of POA, which provide the absorptive medium into which the semi-volatile products can condense.

Figures 2.6 to 2.8 show the predicted zonal annual average global distribution of BC, POA, and SOA. For both BC and POA the surface concentration is predicted to be highest at northern mid-latitudes, indicating the importance of fossil fuel sources. High concentrations in the tropics reflect the significance of biomass burning. Concentrations drop rapidly with height, as distance from the sources increases. The low concentration in the tropical upper troposphere is evidence of removal by convective scavenging. Similar to BC and POA, SOA surface concentrations are predicted to be highest in the tropics and northern mid-latitudes. Unlike the primary aerosols, however, SOA concentration is predicted to exhibit a secondary peak around 400 mbar in extreme northern latitudes. The quantities at higher altitudes result from the transport of gas-phase oxidation products to the upper troposphere, where colder temperatures favor condensation of the semi-volatile gases into the aerosol phase. The peak is not as strong in the SH because POA concentrations are lower in the SH, resulting in less absorptive aerosol into which the semi-volatile gas condense. Even

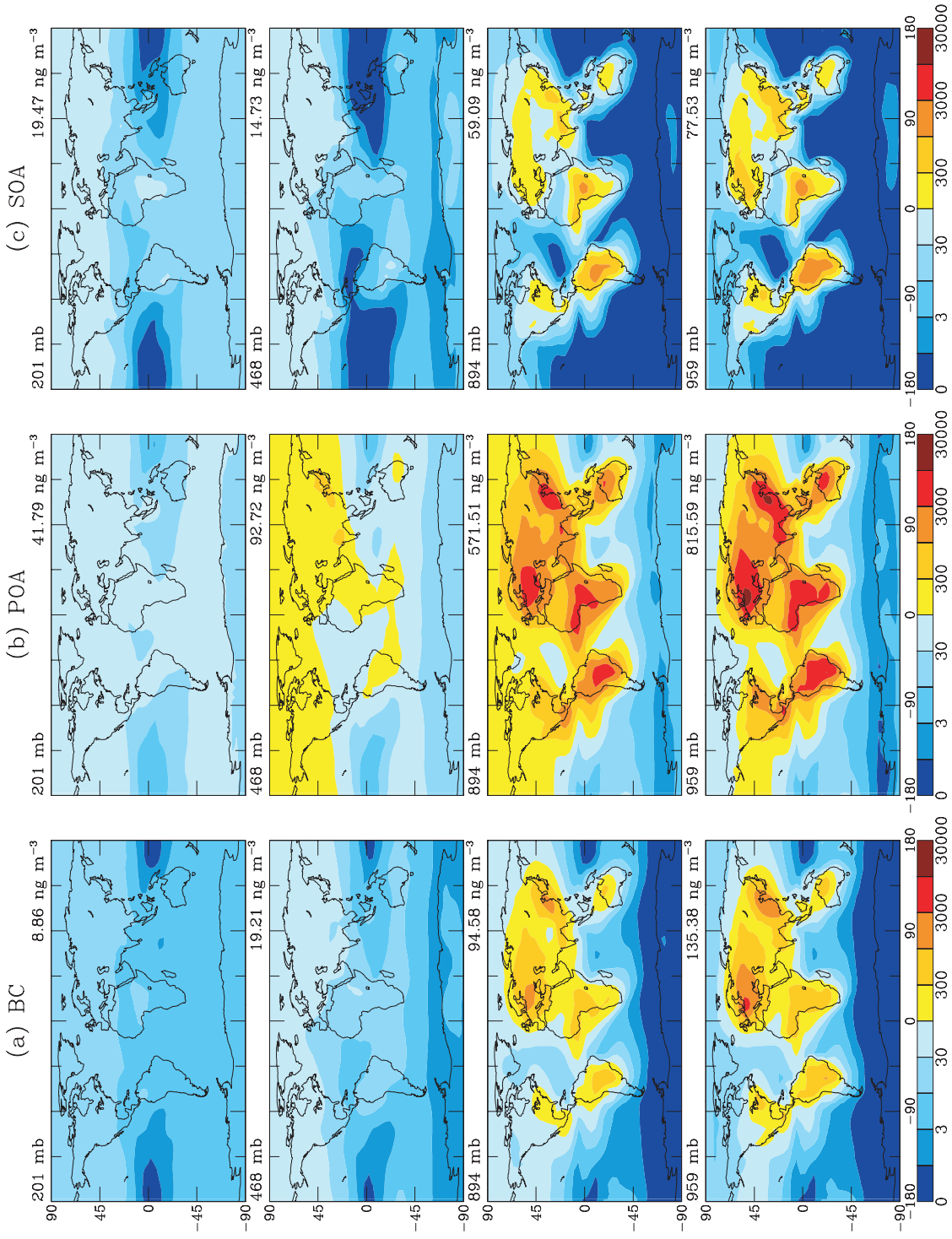

Figure 2.5: (a) Simulated annual average BC concentrations. (b) Simulated annual average POA concentrations. (c) Simulated annual average SOA concentrations. Units are ng m^{-3}.

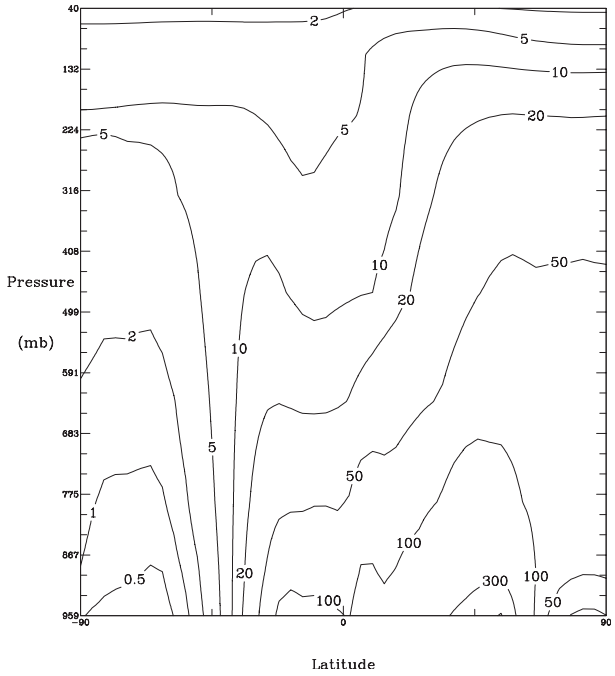

Figure 2.6: Predicted zonal annual average global black carbon distribution (ng m^{-3}).

for products with small partition coefficients, K_{om}, at 298 K (see Table 2.4), K_{om} increases by 3 orders of magnitude (Section 2.3.3) from the temperatures of the surface to those of the upper troposphere, and eventually gas-phase products condense as temperature decreases sufficiently. Figure 2.9 shows the percentage of organic aerosol that is SOA. Near the surface, OC is dominated by POA, but SOA is predicted to contribute approximately one-half of the organic aerosol in the upper troposphere. Again, SOA contribution is predicted to be highest near the polar regions of the upper troposphere. Such predictions of secondary maxima of SOA levels in the cold regions of the upper troposphere have not been verified observationally, although the physics leading to this phenomenon is quite evident.

Simulated global burdens and estimated lifetimes of BC, POA, and SOA are summarized in Table 2.7. In all cases, the dominant sink is wet deposition, estimated to contribute 66%, 69%, and 77% to the total removal of BC, POA, and SOA, respectively. The lifetime of BC is predicted to be longer than that of POA because a higher percentage of BC is assumed

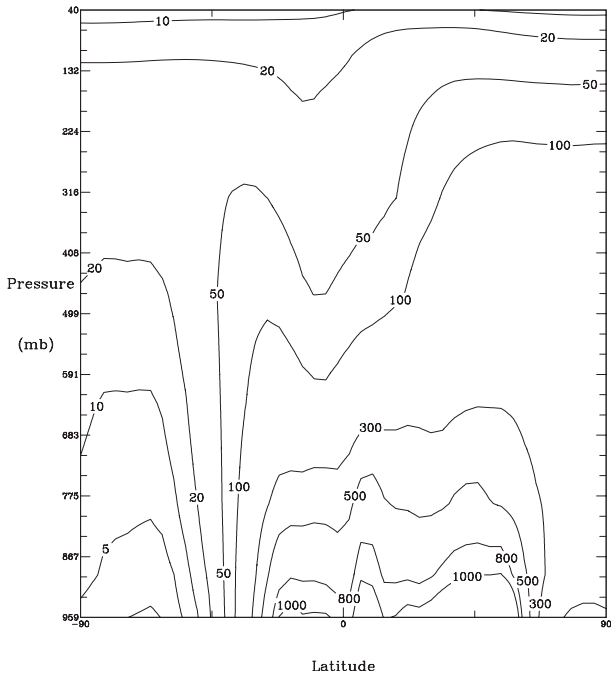

Figure 2.7: Predicted zonal annual average global primary organic aerosol distribution (ng m^{-3}).

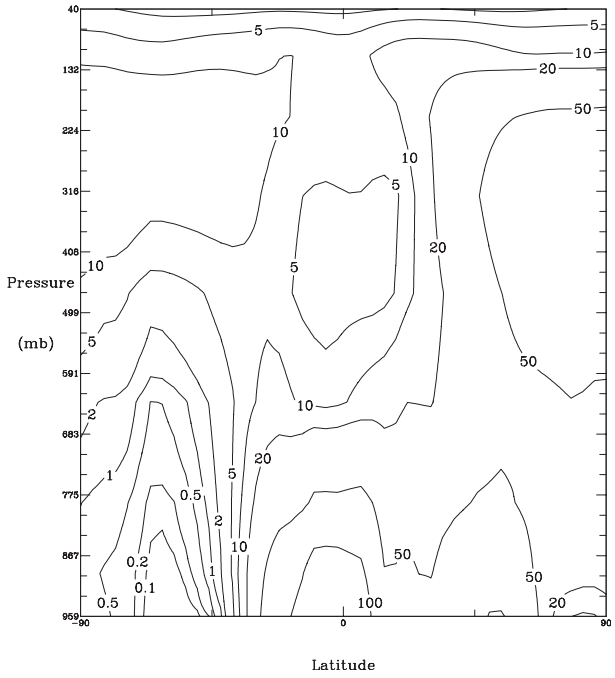

Figure 2.8: Predicted zonal annual average global SOA distribution (ng m^{-3}).

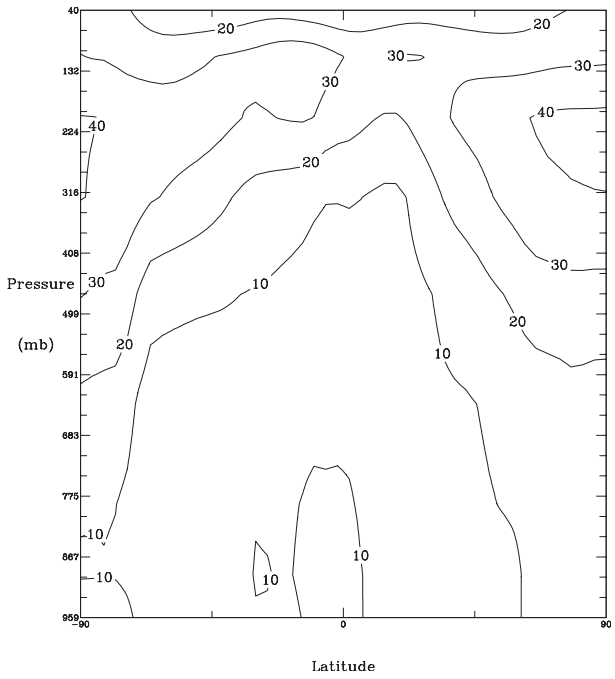

Figure 2.9: Predicted zonal annual average of the SOA global percentage of total organic aerosol (SOA+POA).

Table 2.7: Predicted Global Burdens and Lifetimes (τ)

Aerosol		Burden (Tg)	τ (days)
BC		0.22	6.4
	hydrophobic	0.03	1.0
	hydrophilic	0.19	6.4
POA		1.2	5.3
	hydrophobic	0.1	1.0
	hydrophilic	1.1	5.2
SOA		0.19	6.2

to be hydrophobic, which limits wet scavenging. As noted in Section 2.3.5.1, hydrophobic aerosols are treated as completely insoluble; therefore, they are not removed by in-cloud wet scavenging (they are removed by below-cloud scavenging, dry deposition, and conversion to hydrophilic aerosols). The lifetime of SOA is predicted to be larger than that of POA because only 80% of SOA is considered to be soluble. As seen from Table 2.7, the lifetime of hydrophilic BC is larger than that for hydrophilic POA even though the dry and wet scavenging schemes are the same for both aerosols; the reason is that a higher percentage of hydrophilic BC is converted to the hydrophilic state in regions away from the source and in regions of less precipitation.

The estimated global production of SOA is 11.2 Tg yr^{-1}. Table 2.8 lists the contribution of each class of reactive hydrocarbons to the global SOA production. Tables 2.5 and 2.8 indicate that emission rates are not correlated with SOA production. For example, while sesquiterpenes (class V) contribute only about 8% to the total annual emissions of biogenic hydrocarbons, this class contributes to 22% of the total SOA. This result emphasizes the need for compound-specific biogenic emission inventories and aerosol yield parameters. Table 2.8 also indicates that the contribution from group III (α- and γ- terpinene and terpinolene) is insignificant.

On a global average, NO_3 is predicted to be responsible for only about 2% of the chemical sink of the parent hydrocarbons, while NO_3 oxidation products are estimated to contribute about 9% to total SOA. The small contribution from NO_3 is a result of the fact that biogenic hydrocarbons are emitted during daylight hours and are rapidly oxidized by O_3 and OH. The error introduced by assuming that all NO_3 oxidation products behave the similarly to those of β-pinene oxidation by NO_3 is, consequently, negligible.

Table 2.8: Parent Hydrocarbon Contributions to Global Average SOA

Hydrocarbon class	% Contribution to SOA
I	45
II	21
III	1
IV	11
V	22

2.4.2 Comparison with Observations

In this section we compare the predicted fields of carbonaceous aerosols with observations. Observational data for carbonaceous aerosols are limited, especially for organic aerosols. Most available data were taken over a short period of time at specific locations, making comparison to monthly averages in a GCM grid cell difficult as a basis from which to draw wide-ranging conclusions about the adequacy of the global simulation. To convert to organic carbon mass, which is measured experimentally, we assume that the ratio of organic aerosol mass to organic carbon mass is 1.3 [*Liousse et al.*, 1996]. The assumption of a single value for this conversion factor is, of course, a source of uncertainty.

Table 2.4.2 compares the simulation results to the Interagency Monitoring of Protected Visual Environments (IMPROVE) database [*Malm et al.*, 2000]. The IMPROVE network consists of aerosol and optical measurements at approximately 140 rural sites in the United States. Twenty-four hour aerosol samples were taken twice a week (on Wednesdays and Saturdays). The observation data are averaged over three years from March, 1996 to February, 1999. Related scatter plots are also shown in Figures 2.10 and 2.11. The comparison indicates that the GCM simulation consistently underpredicts both BC and OC concentrations at this set of locations by about a factor of 3 to 4. The underprediction is probably the result of averaging over large grid cells as well as uncertainties in the emission inventory

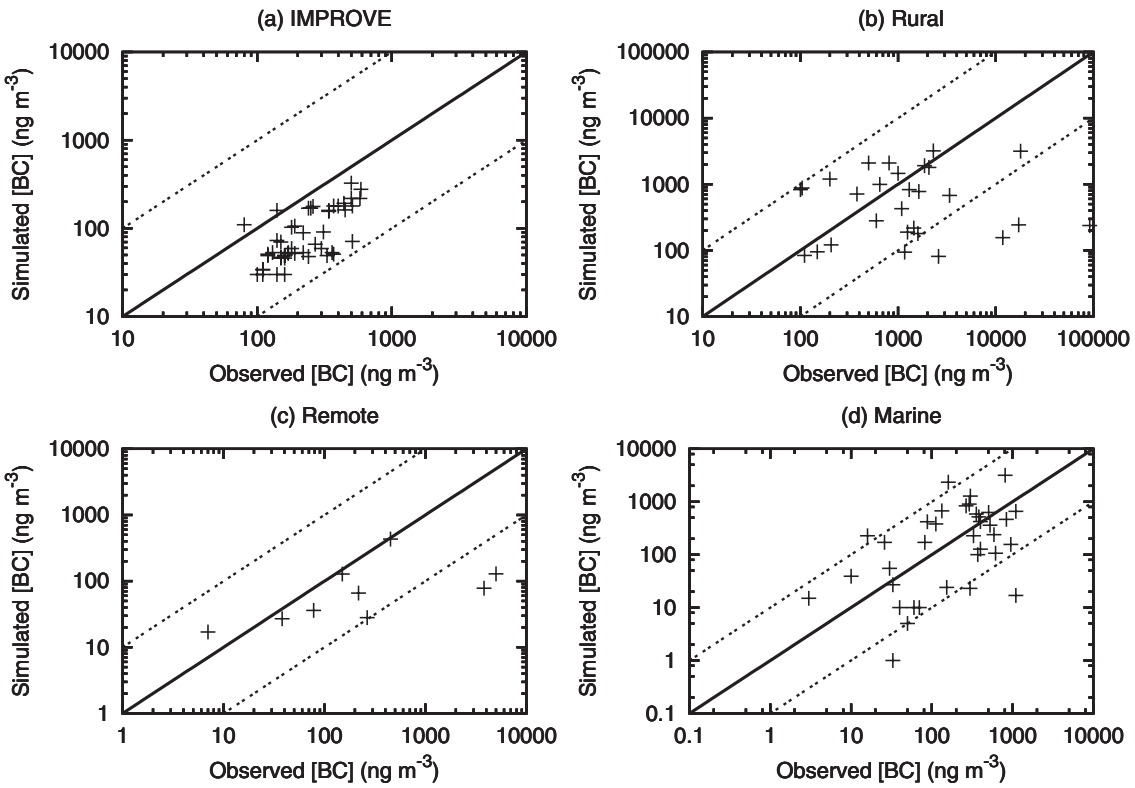

Figure 2.10: Simulated BC concentrations versus observations for (a) IMPROVE sites; (b) rural sites; (c) remote sites; and (d) marine sites. The dashed lines indicate 10:1 and 1:10 ratios.

itself. As discussed in Section 2.3.4 earlier, the BC emissions from fossil fuel used here are less than those of *Cooke and Wilson* [1996], *Cooke et al.* [1999], and *Bond* [2000].

Tables 2.10 to 2.15 show comparison of BC and OC concentrations at various rural, remote, and marine sites, with the corresponding scatter plots in Figures 2.10 and 2.11. Overall, both OC and BC concentrations are underpredicted by about a factor of 2, except at remote sites, for which there are too few data points to draw definitive conclusions. The consistent underestimation suggests that either emissions are too low or wet scavenging is too high.

Table 2.9: Comparison of Simulated and Observed Aerosol Concentrations from the IMPROVE Database

Location	Longitude	Latitude	Elevation	[BC] (ng m^{-3})		[OC] (ng C m^{-3})	
			(m)	Obs	Sim	Obs	Sim
Acadia National Park, Maine	-68.26	44.37	129	240	169	1470	706
Badlands National Park, South Datoka	-101.94	43.74	736	140	73	1130	301
Bandelier Naional Monument, New Mexico	-106.27	35.78	1987	170	53	1140	249
Big Bend National Park, Texas	-103.18	29.30	1075	180	103	1450	519
Boundary Waters Canoe Area, Minnesota	-91.50	47.95	524	190	106	1470	468
Bryce Canyon Natonal Park, Utah	-112.17	37.42	2477	140	30	990	120
Bridger Wilderness, Wyoming	-109.76	42.98	2627	110	34	940	133
Brigantine National Wildlife Refuge, New Jersey	-74.45	39.47	9	510	179	2390	692
Canyonlands National Park, Utah	-109.82	38.46	1799	150	46	820	200
Chassahowitzka National Wildlife, Florida	-82.55	28.75	2	580	218	2780	989
Chiricahua National Monument, Arizona	-109.39	32.01	1570	130	53	920	249
Crater Lake National Park, Oregon	-122.14	42.90	1963	190	52	1100	178
Denali National Park, Alaska	-148.97	63.72	658	100	30	670	102
Dolly Sods/Otter Creek Wilderness, West Virgina	-79.43	39.11	1158	400	179	2440	762
Glacier Natinal Park, Montana	-114.00	48.51	979	360	53	2520	229
Great Basin National Park, Nevada	-114.22	39.01	2068	160	49	1030	191
Hopi Point (Grand Canyon), Arizona	-112.15	36.07	2164	160	49	730	191
Great Sand Dunes National Monument, Colorado	-105.52	37.72	2504	110	30	920	131
Great Smokey Mountains National Park, Tennessee	-83.94	35.63	815	450	162	2910	753
Guadalupe Mountains National Park, Texas	-104.81	31.83	1674	150	70	1010	369
Jarbidge Wilderness, Nevada	-115.43	41.89	1882	120	51	1070	191
Lassen Volcanic National Park, California	-121.58	40.54	1755	170	52	1380	178
Lone Peak Wilderness, Utah	-111.71	40.44	1768	330	49	1560	190
Lye Brook Wilderness, Vermont	-73.12	43.15	1010	260	177	1520	725
Mammoth Cave National Park, Kentucky	-86.15	37.13	248	500	325	2830	1455
Mesa Verde National Park, Colorado	-108.49	37.20	2177	160	46	910	200
Moosehorn National Wildlife Refuge, Maine	-67.26	45.12	76	250	169	1700	706
Mount Rainier National Park, Washington	-122.12	46.76	427	310	91	2050	375
Mount Zirkel Wilderness, Colorado	-106.73	40.47	3243	110	34	820	133
Okefenokee National Wildlife Refuge, Georgia	-82.13	30.74	49	500	218	2990	989
Petrified Forest National Park, Arizona	-109.77	35.08	1767	220	53	1070	249
Pinnacles National Monument, California	-121.16	36.49	317	340	160	1780	609
Point Reyes National Seashore, California	-122.90	38.12	38	140	160	1230	609
Redwood National Park, California	-124.08	41.56	245	80	110	980	472
Cape Romain National Wildlife Refuge, South Carolina	-76.99	32.94	3	440	192	2800	781
Rocky Mountain National Park, Colorado	-105.55	40.28	2400	150	47	1020	191
San Gorgonio Wilderness, California	-116.90	34.18	1712	370	51	2040	193
Sequoia National Park, California	-118.82	36.50	549	510	71	3280	274
Shenandoah National Park, Virgina	-78.43	38.52	1098	370	179	2200	762
Shining Rock Wilderness, North Carolina	-82.77	35.39	1621	270	66	1790	293
Sipsy Wilderness, Alabama	-87.31	34.34	279	590	277	3400	1298
Snoqualamie Pass, Washington	-121.43	47.42	1160	300	59	1450	249
Three Sisters, Oregon	-122.04	44.29	885	180	59	1490	249
Tonto National Monument, Arizona	-111.11	33.65	786	220	89	1280	371
Upper Buffalo Wilderness, Arkansas	-93.20	35.83	723	340	156	2350	750
Weminuche Wilderness, Colorado	-107.80	37.66	2765	160	30	760	131
Yellowstone National Park, Wyoming	-110.40	44.57	2425	120	49	1320	210
Yosemite National Park, California	-119.70	37.71	1615	240	48	2280	180

NP=National Park; NWR=National Wildlife Refuge.
Reference: *Malm et al.* [2000]

Table 2.10: Comparison of Simulated and Observed BC Concentrations in Rural Areas

Location	Longitude	Latitude	Elevation (km)	Season	Observed (ng m^{-3})	Simulated (ng m^{-3})	Reference
Abisko, Sweden	18.5E	68.3N	0	Mar-Apr	206	157	*Noone and Clarke* [1988]
Allegheny Mt, Pennsylvania	79W	39N	0.82	Aug	1250	196	*Japar et al.* [1986]
Anadia, Portugal	8.4W	40.3N	0	Aug	1594	147	*Castro et al.* [1999]
Aspvreten, Sweden	17.4E	58.8N	0	Jun-Jul	100	1196	*Zappoli et al.* [1999]
Aveiro, Portugal	8W	40N	0	Annual	11800	141	*Nunes and Pio* [1993]
Bridgewater, Canada	64.5W	44.4N	0	Aug-Nov	2600	87	*Chýlek et al.* [1999]
Central Africa	17-19E	2-12N	0	Nov-Dec	3363	718	*Ruellan et al.* [1999]
Chebogue Point, Canada	66W	43N	0	Aug-Sep	110	104	*Chýlek et al.* [1999]
Cheboygan County, Michigan	84.7W	45.5N	0	Dec-Apr	600	279	*Cadle and Dasch* [1988]
Edgbaston, UK	1W	51 N	0	Annual	380	687	*Smith et al.* [1996]
Guayaquil, Ecuador	79.9W	2.2S	0	Jun	520	662	*Andreae et al.* [1984]
Hemsby, England	1.4E	52.4N	0	Annual	104	947	*Yaaqub et al.* [1991]
Ivory Coast Savannah	5.1W	6.2N	0	Annual	1300	812	*Wolff and Cachier* [1998]; *Cachier et al.* [1990]
				Winter	1867	1921	*Cachier et al.* [1989]
				Fall	200	1131	*Cachier et al.* [1989]
K-puszta, Hungary	19.5E	46.9N	0	Jul-Aug	500	2065	*Molnár et al.* [1999]; *Zappoli et al.* [1999]
				Annual	810	2173	*Heintzenberg and Mészáros* [1985]
Lahore, Pakistan	74 E	31N	0	Annual	17200	235	*Smith et al.* [1996]
Laurel Hill, Pennsylvania	79W	40N	0.85	Aug	1450	217	*Japar et al.* [1986]
Lin-an station, China	119.7E	30.8N	0	Jul-Sep	2070	1814	*Parungo et al.* [1994]
Melpitz, Germany	12E	51N	0	Annual	2300	3314	*Heintzenberg et al.* [1998]
Mt Kanobili, Georgia	42.7E	41.5N	2.00	Jul	1088	423	*Dzubay et al.* [1984]
Nylsvley Natural Reserve, So	28.4E	24.7S	1.10	May	850	141	*Puxbaum et al.* [2000]
Orogrande, New Mexico	106W	34.3N	0	Dec-Jan	149	87	*Pinnick et al.* [1993]
Petten, the Netherlands	3E	52.9N	0	Apr	1631	940	*Berner et al.* [1996]
Rautavaara, Finland	28.3E	63.5N	0	Dec	650	1215	*Raunemaa et al.* [1994]
San Pietro Capofiume, Italy	11.6E	44.7N	0	Sep-Oct	1000	1327	*Zappoli et al.* [1999]
Tábua, Portugal	17W	33N	0	Jul-Aug	1167	57	*Castro et al.* [1999]
Wageninen, the Netherlands	5.7E	52N	0	Jan	18000	2849	*Janssen et al.* [1997]
West Mountain, China	116E	40N	0	Jul-Sep	91711	251	*Parungo et al.* [1994]

Table 2.11: Comparison of Simulated and Observed BC Concentrations in Remote Areas

Location	Longitude	Latitude	Elevation (km)	Season	Observed (ng m^{-3})	Simulated (ng m^{-3})	Reference
Mt Krvavec, Slovenia	14.5 E	46.3 N	1.74	Dec	150	74	*Bizjak et al.* [1999]
Mt Krvavec, Slovenia	14.5 E	46.3 N	1.74	Jul	450	273	*Bizjak et al.* [1999]
Mt Mitchell, North Carolina	82.3W	35.7N	2.04	Annual	217	74	*Bahrmann and Saxena* [1998]
Mt Sonnblick, Austria	13E	47N	3.10	Jul	5000	79	*Hitzenberger et al.* [1999]
				Sep	3800	51	*Hitzenberger et al.* [1999]
Ostrov Golomyanny, Russia	90.6E	79.5N	0	Mar-May	265	23	*Polissar* [1993]
Spitsbergen, Norway	11.9E	78.9N	0	Oct-May	78	37	*Heintzenberg and Leck* [1994]
				May-Oct	7	18	*Heintzenberg and Leck* [1994]
Wrangle Island, Russia	179.6W	71N	0	Mar-May	38	23	*Hansen et al.* [1991]

Table 2.12: Comparison of Simulated and Observed BC Concentrations in Marine Areas

Location	Longitude	Latitude	Season	Observed ($ng\ m^{-3}$)	Simulated ($ng\ m^{-3}$)	Reference
Arctic Region	15W to 50E	74 to 83 N	Jul-Sep	3	16	*Heintzenberg* [1982]
Areão, Portugal	8.8W	40.5N	Annual	950	141	*Pio et al.* [1996]
Areão, Portugal	8.8W	40.5N	Summer	589	164	*Castro et al.* [1999]
Areão, Portugal	8.8W	40.5N	Winter	370	109	*Castro et al.* [1999]
Atlantic Ocean	7-15W	29-41N	Jun-Jul	400	95	*Novakov et al.* [2000]
Atlantic Ocean (North)	21W to 20E	52-79N	Jul-Sep	88	464	*Polissar* [1992]
Atlantic Ocean (Northeast)	20E to 50W	50-80N	Oct-Nov	112	405	*O'Dowd et al.* [1993]
Sargasso Sea	50W	30N	Jul	60	10	*Chesselet et al.* [1981]
Bermuda	64.5W	32.2N	Jan-Feb	30	51	*Wolff et al.* [1986]
			Aug	40	15	*Wolff et al.* [1986]
Boistö Island	26.5E	60.3N	Jun	525	498	*Raunemaa et al.* [1993]
Corsica, France	9E	42N	Spring	383	593	*Cachier et al.* [1989]
South Uist, UK	7W	57N	Winter	16	313	*Loew et al.* [1996]
			Summer	26	176	*Loew et al.* [1996]
			Winter	328	313	*Loew et al.* [1996]
			summer	82	176	*Loew et al.* [1996]
Western Mediterranean	0-10E	36-46N	Annual	400	427	*Cachier et al.* [1990]
Chichi-jima, Japan	142E	27N	Dec	614	90	*Ohta and Okita* [1984]
Enewetak Atoll	162E	11N	Apr	50	6	*Cachier et al.* [1990]
Hachijo-jima, Japan	139.8E	33.1N	Dec-Jan	838	485	*Ohta and Okita* [1984]
Cheju Island, Korea	127.2E	33.3N	Dec-Mar	300	1267	*Kim et al.* [2000]
			Jul-Oct	290	807	*Kim et al.* [2000]
			Jul-Aug	266	751	*Kim et al.* [1999]
Pacific Ocean	132-139E	32-34N	Dec	1100	612	*Ohta and Okita* [1984]
Pacific Ocean	145-155W	20 N	Aug	1100	16	*Andreae et al.* [1984]
Pacific Ocean	120W	0	Jul	10	38	*Andreae et al.* [1984]
Pacific Ocean	125-128E	28-32N	Dec	133	588	*Parungo et al.* [1994]
Pacific Ocean	124-129E	27-33N	Oct-Nov	505	640	*Parungo et al.* [1994]
Pacific Ocean	126-129E	27-32N	Apr-May	355	464	*Parungo et al.* [1994]
Pacific Ocean	140-165E	0	Jun	9	0	*Parungo et al.* [1994]
Pacific Ocean	165E	10N	Jul	25	0	*Parungo et al.* [1994]
Pacific Ocean	175E	8-18S	Sep	101	4	*Kaneyasu and Murayama* [2000]
Pacific Ocean	175E	8S-25N	Sep-Oct	33	1	*Kaneyasu and Murayama* [2000]
Pacific Ocean	175E	22-8N	Apr-May	70	11	*Kaneyasu and Murayama* [2000]
Pacific Ocean	175E	8-15S	Apr-May	40	0	*Kaneyasu and Murayama* [2000]
Pacific Ocean	175E	30-35N	May-Jun	297	24	*Kaneyasu and Murayama* [2000]
Pacific Ocean	175E	44-48N	May-Jun	153	27	*Kaneyasu and Murayama* [2000]
Pacific Ocean	175E	5.7S	Sep-Oct	29	0	*Kaneyasu and Murayama* [2000]
Pacific Ocean	175E	6.0N	Sep-Oct	37	0	*Kaneyasu and Murayama* [2000]
Pacific Ocean	175E	5.3S	May-Jun	22	0	*Kaneyasu and Murayama* [2000]
China Sea	113E	10N	Jun	33	22	*Parungo et al.* [1994]
Fuji Island, Japan	175 E	15.7S	Sep	113	4	*Kaneyasu and Murayama* [2000]
San Nicolas Island, USA	119.3E	33.15N	Jun-Sep	160	2232	*Chow et al.* [1994]
			Nov-Dec	810	3153	*Chow et al.* [1994]

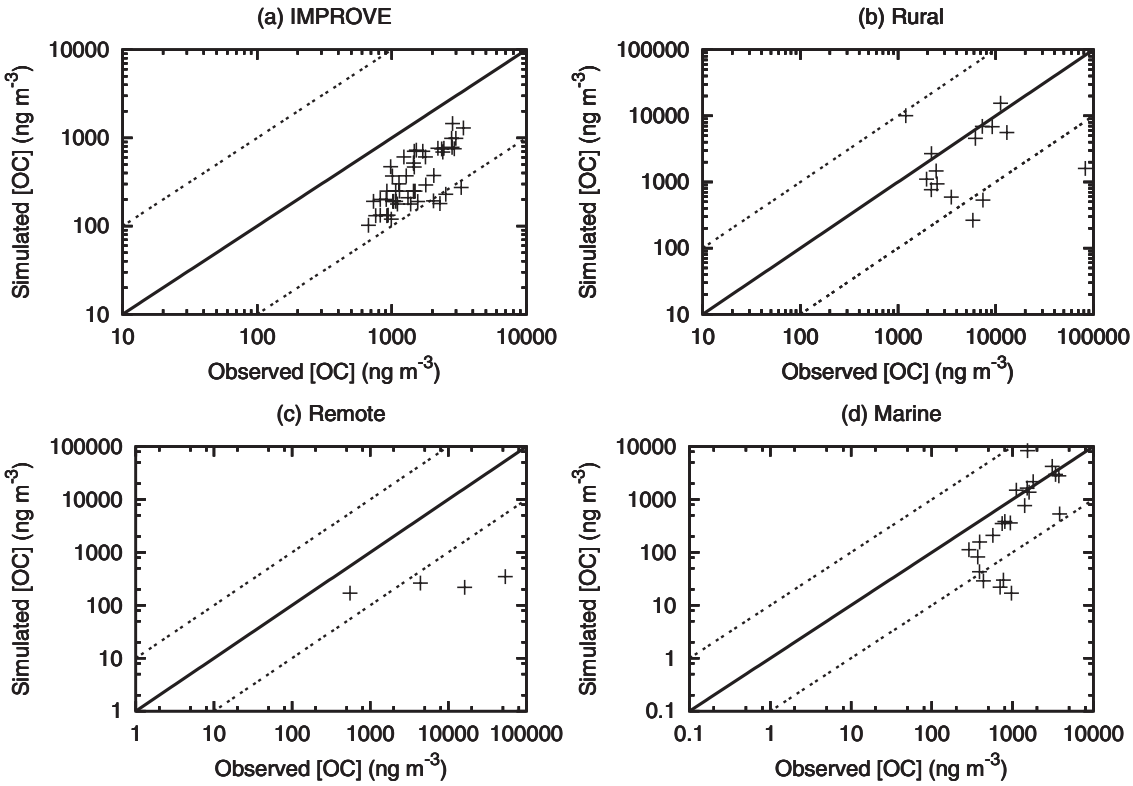

Figure 2.11: Simulated OC concentrations versus observations for (a) IMPROVE sites; (b) rural sites; (c) remote sites; and (d) marine sites. The dashed lines indicate 10:1 and 1:10 ratios.

Table 2.13: Comparison of Simulated and Observed OC Concentrations in Rural Areas

Location	Longitude	Latitude	Elevation (km)	Season	Observed (ng m^{-3})	Simulated (ng m^{-3})	Reference
Allegheny Mt, Pennsylvania	79W	39N	0.82	Aug	2190	763	*Japar et al.* [1986]
Anadia, Portugal	8.4W	40.3N	0	Aug	3506	591	*Castro et al.* [1999]
Aspvreten, Sweden	17.4E	58.8N	0	Jun-Jul	2200	2681	*Zappoli et al.* [1999]
Aveiro, Portugal	8W	40N	0	Annual	7400	531	*Nunes and Pio* [1993]
Central Africa	17-19E	2-12N	0	Nov-Dec	13021	5598	*Ruellan et al.* [1999]
Cheboygan County, Michigan	84.7W	45.5N	0	Dec-Apr	1960	1101	*Cadle and Dasch* [1988]
Guayaquil, Ecuador	79.9W	2.2S	0	Jun	510	6171	*Andreae et al.* [1984]
Ivory Coast savannah	5.1W	6.2N	0	Annual	9200	6852	*Wolff and Cachier* [1998]; *Cachier et al.* [1990]
				Winter	11233	15539	*Cachier et al.* [1989]
				Fall	1200	10044	*Cachier et al.* [1989]
K-puszta, Hungary	19.5E	46.9N	0	Jul-Aug	7300	6924	*Molnár et al.* [1999]; *Zappoli et al.* [1999]
Lahore, Pakistan	74 E	31N	0	Annual	82800	1605	*Smith et al.* [1996]
Laurel Hill, Pennsylvania	79W	40N	0.85	Aug	2510	935	*Japar et al.* [1986]
Mt Kanobili, Georgia	42.7E	41.5N	2.00	Jul	2460	1464	*Dzubay et al.* [1984]
Nylsvley Natural Reserve, So	28.4E	24.7S	1.10	May	14100	1242	*Puxbaum et al.* [2000]
San Pietro Capofiume, Italy	11.6E	44.7N	0	Sep-Oct	6200	4561	*Zappoli et al.* [1999]
Tábua, Portugal	17W	33N	0	Jul-Aug	5833	264	*Castro et al.* [1999]

Table 2.14: Comparison of Simulated and Observed OC Concentrations in Remote Areas

Location	Longitude	Latitude	Elevation (km)	Season	Observed (ng m^{-3})	Simulated (ng m^{-3})	Reference
El Yunque peak, Puerto Rico	65.8W	18.3N	1.00	Apr	552	169	*Chesselet et al.* [1981]
Hotel Everest View, Nepal	86.4E	27.5N	3.90	Dec-Jan	4400	262	*Davidson et al.* [1986]
Mt Sonnblick, Austria	13E	47N	3.10	Jul	53700	348	*Hitzenberger et al.* [1999]
				Sep	16200	219	*Hitzenberger et al.* [1999]

Table 2.15: Comparison of Simulated and Observed OC Concentrations in Marine Areas

Location	Longitude	Latitude	Season	Observed (ng m^{-3})	Simulated (ng m^{-3})	Reference
Areão, Portugal	8.8W	40.5N	Annual	3830	531	*Pio et al.* [1996]
			Summer	1410	764	*Castro et al.* [1999]
			Winter	940	360	*Castro et al.* [1999]
Atlantic Ocean	7-15W	29-41N	Jun-Jul	800	382	*Novakov et al.* [2000]
Sargasso Sea	50W	30N	Jul	435	29	*Chesselet et al.* [1981]
Bermuda	64.5W	32.2N	Jan-Feb	570	209	*Wolff et al.* [1986]
			May	288	112	*Hoffman and Duce* [1974]
			Jun	370	82	*Hoffman and Duce* [1977]
			Aug	770	30	*Wolff et al.* [1986]
Cape San Juan, Puerto Rico	66.1W	18.5N	Feb-May	391	157	*Novakov et al.* [1997]
Corsica, France	9E	42N	Spring	1517	1641	*Cachier et al.* [1989]
Western Mediterranean	0-10E	36-46N	Annual	1600	1369	*Cachier et al.* [1990]
Chichi-jima, Japan	142E	27N	Dec	743	351	*Ohta and Okita* [1984]
Enewetak Atoll	162E	11N	Apr-May	970	17	*Chesselet et al.* [1981]
			Apr	700	22	*Cachier et al.* [1990]
Hachijo-jima, Japan	139.8E	33.1N	Dec-Jan	1113	1501	*Ohta and Okita* [1984]
Cheju Island, Korea	127.2E	33.3N	Dec-Mar	3100	4213	*Kim et al.* [2000]
Cheju Island, Korea	127.2E	33.3N	Jul-Oct	3400	2976	*Kim et al.* [2000]
			Jul-Aug	3734	2792	*Kim et al.* [1999]
Oahu, Hawaii, USA	147.7W	21.4N	Jul-Oct	390	43	*Hoffman and Duce* [1977]
Pacific Ocean (coast of Japan)	132-139E	32-34N	Dec	1800	2173	*Ohta and Okita* [1984]
San Nicolas Island, USA	119.3E	33.15N	Jun-Sep	1530	8360	*Chow et al.* [1994]
			Nov-Dec	100	10912	*Chow et al.* [1994]
Tutuila Island, American Sam	170.6W	14.3S	Jun-Aug	220	10	*Hoffman and Duce* [1977]

2.4.2.1 Seasonal variations of black carbon

An analysis that is perhaps more relevant to judging the accuracy of the GCM simulation that uses averaged climatology over large grid cells is the comparison with long-term observations that smooth out day-to-day variations.

Figure 2.12 shows the observed and simulated BC concentrations at six different sites in the NH. Figure 2.12a shows the comparison in Barrow, Alaska (71.2°N, 156.3°W), a site representative of the Arctic region. The maximum in early spring is indicative of the Arctic haze phenomenon caused by long-range transport from northern mid-latitudes, especially northern Europe and Russia [*Bodhaine*, 1995; *Polissar et al.*, 1999]. Even though the simulation exhibits a small seasonal variation reflected in the observations, the simulated concentrations are as much as a factor of 4 less than observed values. A similar result was obtained by *Liousse et al.* [1996], who used the same BC emission inventory. Underprediction in the polar regions may be the result of underestimation of biomass sources. For example, boreal fires in Russia may contribute 0.02 to 0.5 Tg yr^{-1} of BC [*Lavoué et al.*, 2000], which is not included in the present inventory. Other possible explanations include overestimation of wet scavenging and inaccurate representation of advection to the polar regions by the GCM. Figure 2.12b shows comparison of predictions and observations at Alert, Canada (82.5°N, 62.3°W), another high Arctic site. Observed BC concentrations and seasonality are similar to those of Barrow, Alaska. Again, BC concentrations are underpredicted.

Figure 2.12c compares the BC observations and predictions at Jungfraujoch, Switzerland (46.5°N, 8.0°E, 3.45 km above sea level (asl)), a site that is predominantly in the free troposphere [*Nyeki et al.*, 1998]. Both observations and predictions exhibit a minimum during the winter months and maximum concentrations almost an order of magnitude greater than the minimum. Observations show a peak in April and a larger peak in July. The peaks

are reproduced by the simulations, but offset by one and two months, respectively, possibly because of representation of the atmospheric boundary layers by the GCM. The seasonal cycle results from vertical transport of boundary layer air masses from the Swiss Plateau to the Jungfraujoch due to enhanced thermal convection, which occurs more frequently during spring and summer [*Baltensperger et al.*, 1997; *Lugauer et al.*, 1998; *Lavanchy et al.*, 1999]. During winter, the air mass is decoupled from the boundary layer, resulting in considerably lower BC concentrations indicative of those of the free troposphere.

Figure 2.12d compares the predicted and observed BC concentrations at Mace Head, Ireland (53.3°N, 9.9°W). The data at this site were taken on an almost continuous basis from February 1989 to June 1996. Located on the west coast of Ireland, Mace Head is right on the western border of a GCM grid cell that covers most of Ireland (the grid box covers 5-10°W in longitude); the predictions shown in Figure 2.12d, therefore, include strong anthropogenic influence. The meteorology of Mace Head, however, is dominated by relatively unpolluted westerly and southwesterly winds from over the northern Atlantic Ocean [*Cooke et al.*, 1997]. In Figure 2.12d, observational data from the clean sector and the continental sector are shown separately. BC concentrations from the continental sector are an order of magnitude higher than those from the clean sector and are in better agreement with the simulations; however, the predictions are still too high. One concludes that the BC emission inventory is likely too high in Europe. For example, fossil fuel emissions in Europe from the current inventory are almost three times the amount predicted by *Bond* [2000]. The maximum BC concentration at Mace Head in February is likely the result of increased fossil fuel emission from domestic heating during winter. *Cooke et al.* [1997] have suggested that the BC peak in May observed in both the clean and continental sectors is probably a result of reduced wet scavenging at that time. This secondary peak is not reproduced

by the simulation. Moreover, *Koch* [2001] indicates that BC concentrations at this site are very sensitive to wet scavenging.

Figure 2.12e compares BC predictions and observations at Mauna Loa, Hawaii (19.3°N, 155.4°W, 3.4 km asl). This site is often representative of mid-troposphere conditions, particularly during nighttime downslope winds [*Mendonca*, 1969]. The observed springtime maximum in BC is attributable to long-range transport from the Asian continent, as evidenced by dust levels [*Darzi and Winchester*, 1982; *Harris and Kahl*, 1990]. As compared to the observations, the predicted peak in BC is delayed by two months and is somewhat lower. It has been noted that during strong dust episodes, dust can account for as much as 20% of the total measured absorption, thus contributing to absorption measurements (using an aethalometer) from which BC concentrations are inferred [*Bodhaine*, 1995].

Finally, Figure 2.12f shows the seasonality of BC concentrations at Sapporo, Japan (43°N, 141°E). Here the observations are an order of magnitude higher than predictions. Sapporo is an urban site, whereas GCM grid cell includes the surrounding rural and marine areas as well. The limitations of comparing point observations with grid-cell average GCM predictions are exemplified in this case.

Figure 2.13 shows the comparison between observed and simulated BC concentrations at four different sites in the SH. Figure 2.13a shows BC concentrations at the sub-Antarctic site of Amsterdam Island (38°S, 77°E). Here the seasonal cycle is dominated by biomass burning emissions, which are dominant from June to August, a trend matched by the predictions. The lower-than-expected BC predictions suggest that either emissions are understated or wet-scavenging is overstated.

Figure 2.13b shows the annual cycle of BC concentrations at Amundsen-Scott Station, South Pole (89°S, 102°W, 2.8 km asl). The simulation produces a peak in spring that

appears in the data; however, the simulated peak concentration is three times higher than that observed. The low observed BC concentrations observed is likely a consequence of the measurement technique. Black carbon concentrations were inferred from light attenuation measurements using an aethalometer [*Hansen et al.*, 1982; *Bodhaine*, 1995]. The attenuation cross section can vary by a factor of 3 from that used in the calibration, due to varying particle shape and surface coating. Remote BC particles have on average lower cross sections, implying that concentrations from the aethalometer are lower than the true values [*Liousse et al.*, 1993]. The spring maximum is most likely a result of increased long-range continental transport when the circumpolar vortex breaks down together with simultaneous biomass burning in the SH. Observational data indicate a peak in January that is not evident in the simulation. Advection toward the South Pole might be inaccurately represented. A similar seasonal trend is observed at another Antarctic site, Halley (75.6°S, 26.2°W) (Figure 2.13c). There the observed BC is higher because the location is closer to the source regions, and a smaller cross section is used to infer the aethalometer measurements. The underprediction again suggests either that emissions are too low or that wet deposition is too strong.

Figure 2.13d shows comparison of black carbon concentrations at another remote SH site, the Australian Baseline Atmospheric Pollution Monitoring Station at Cape Grim, Tasmania (40.7°S, 144.7°E). The observation data include only the clean air sector [*Heintzenberg and Bigg*, 1990] and are lower than predicted. The relevant GCM grid cell covers most of Tasmania. According to *Heintzenberg and Bigg* [1990], the seasonality of BC concentrations at Cape Grim is a result of that of biomass mass burning in the SH. However, the observed peak in October occurs two months after the biomass burning peak. The predicted concentration tracks the biomass emission source strength, which peaks during June to August. The reason for this discrepancy is not known.

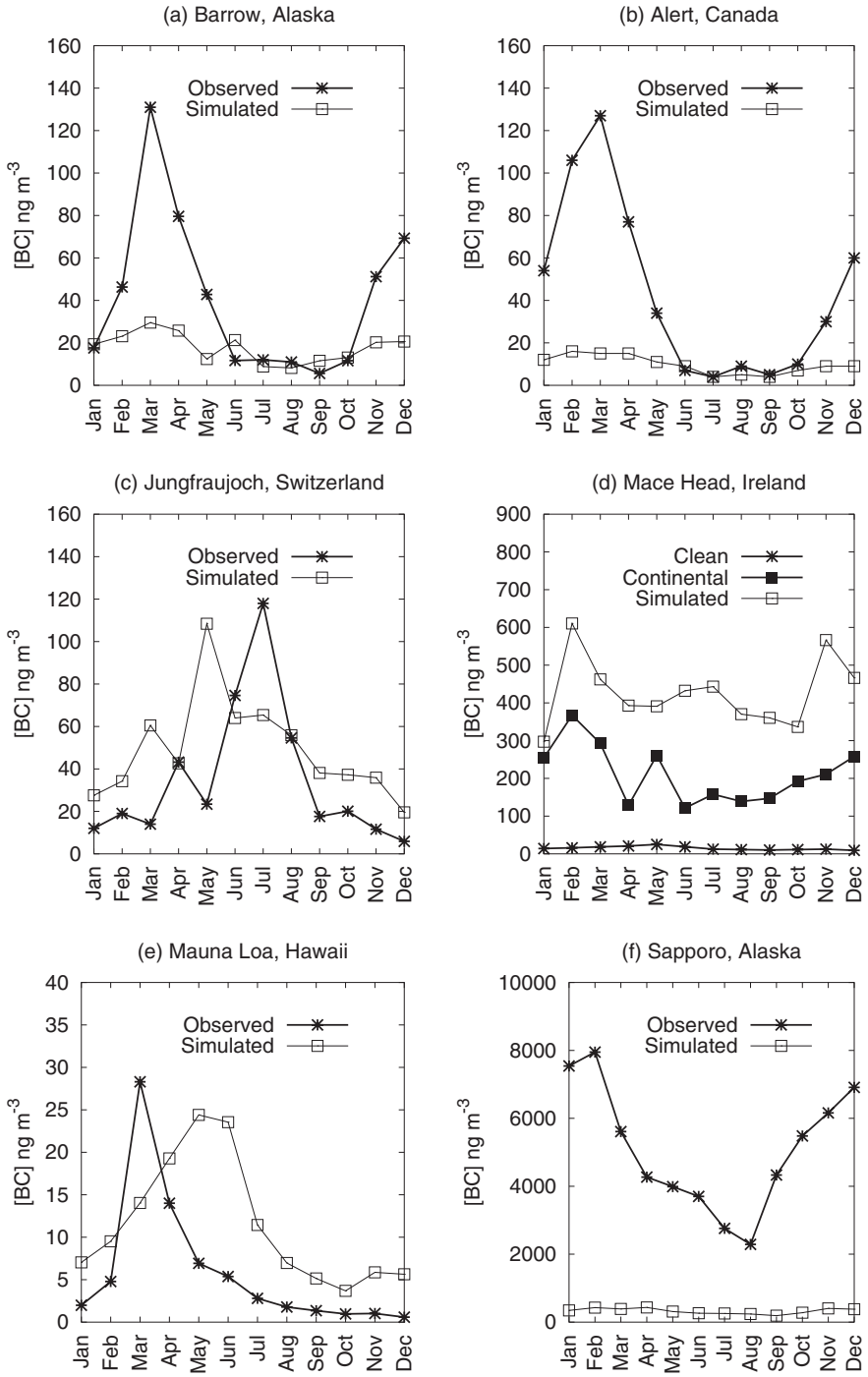

Figure 2.12: Seasonal cycle of black carbon concentrations at various sites in the NH: (a) Barrow, Alaska (71.2°N, 156.3°W) [*Bodhaine*, 1995]; (b) Alert, Canada (82.5°N, 62.3°W) [*Hopper et al.*, 1994]; (c) Jungfraujoch, Switzerland (46.5°N, 9°E, 3.45 km asl) [*Nyeki et al.*, 1998]; (d) Mace Head, Ireland (53.3°N, 9.9°W) [*Cooke et al.*, 1997]; (e) Mauna Loa, Hawaii (19.3°N, 155.4°W, 3.4 km asl) [*Bodhaine*, 1995]; and (f) Sapporo, Japan (43°N, 141°E) [*Ohta and Okita*, 1990].

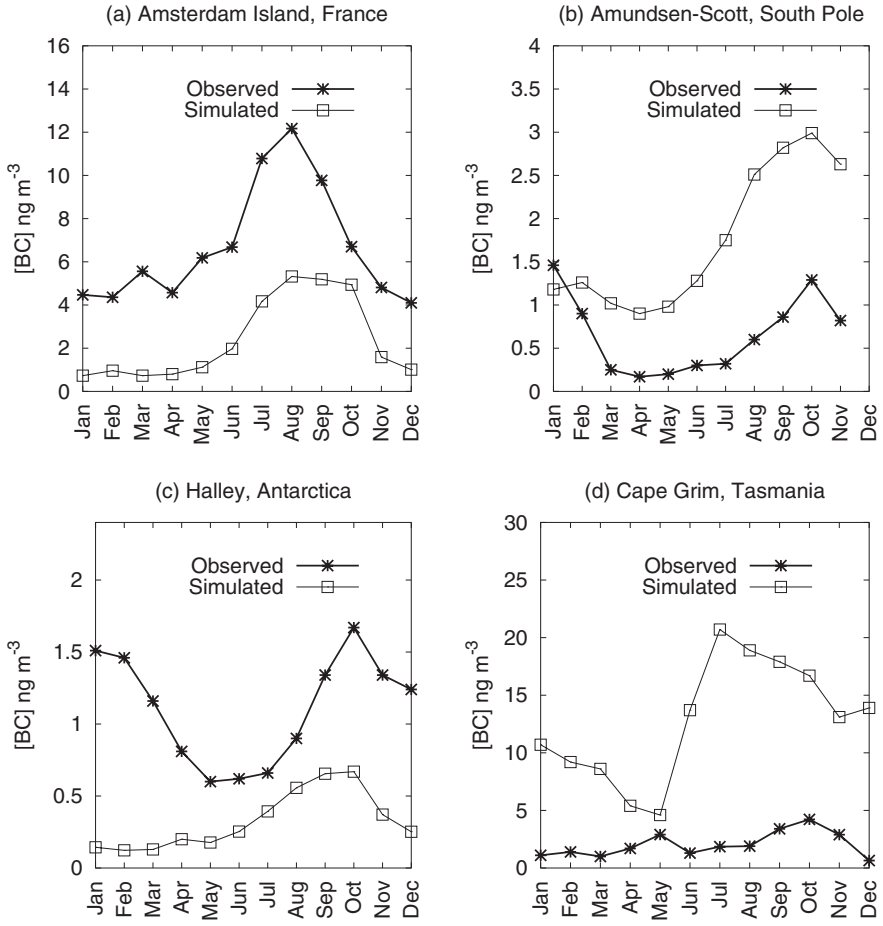

Figure 2.13: Seasonal cycle of black carbon concentrations at various sites in the SH: (a) Amsterdam Island, France (38°S, 77°E) [*Wolff and Cachier*, 1998]; (b) Amundsen-Scott Station, South Pole (89°S, 102°W, 2.84 asl) [*Bodhaine*, 1995]; (c) Halley, Antarctica (75.6°S, 26.2°W) [*Wolff and Cachier*, 1998]; and (d) Cape Grim, Tasmania (40.7°S, 144.7°E) [*Heintzenberg and Bigg*, 1990]

2.4.3 Comparison with Previous Work

2.4.3.1 Black carbon

Table 2.16 compares the global BC burdens and lifetimes predicted here with those of previous work. Among previous studies, *Liousse et al.* [1996] and *Koch* [2001] used the same BC emission inventory as this work. Compared to *Liousse et al.* [1996], the global BC burden predicted here is 0.21 Tg versus 0.13 Tg with a longer lifetime (6.4 versus 4-4.5 days). The difference arises because *Liousse et al.* [1996] assumed all BC to be hydrophilic, leading to more effective wet scavenging. The lower wet deposition rate in the present case leads to higher BC concentrations at high altitudes. The same explanation also accounts for the difference in global burden and lifetime between this work and that of *Koch* [2001], which also used the GISS GCM II-prime. For three cases studied by *Koch* [2001], in which in-cloud convective scavenging removes all soluble and insoluble aerosols, the lifetime of BC is predicted to be 4.28-4.44 days. For the case in which only soluble aerosols are removed, as assumed here, the lifetime is predicted to be 8.42 days. The longer lifetime in the latter case results because all BC is assumed to be emitted as hydrophobic and ages from hydrophobic to hydrophilic as determined by the oxidation of SO_2 by OH. *Koch* [2001] assumed hydrophilic BC to be 90% soluble, as compared to 100% in our case. The global burden of BC as predicted *Cooke and Wilson* [1996] is higher than that predicted here (0.28 Tg versus 0.21 Tg), and their estimated lifetime is longer (6-10 days versus 6.4 days). *Cooke and Wilson* [1996] used a larger emission inventory (14 Tg yr^{-1} compared to the present 12 Tg yr^{-1}) with all (compared to 80% in our case) BC emitted as hydrophobic aerosol and conversion to hydrophilic with a time constant of 0.8-1.6 days instead of 1.15 days. *Cooke et al.* [1999] considered only fossil fuel sources of BC, resulting in an expected lower global

Table 2.16: Comparison of Predicted BC Global Burdens and Lifetimes

Reference	Burden (Tg)	Lifetime (days)
This work	0.22	6.4
Cooke and Wilson [1996]	0.28	6-10
Liousse et al. [1996]	0.13	4-4.5
Cooke et al. [1999]	0.073[a]	5.29[a]
Koch [2001]	0.14-0.29[b]	4.28-8.42[b]

[a] Fossil fuel only.
[b] The range of estimates arises from different wet scavenging schemes.

Table 2.17: Comparison of Predicted POA Global Burdens and Lifetimes

Reference	Burden (Tg)	Lifetime (days)
This work	1.2	5.3
Cooke et al. [1999]	0.11[a]	4.54[a]
Koch [2001]	0.95	3.86

[a] Fossil fuel only.

burden and a shorter lifetime of 5.3 days. They also used a different GCM and different dry deposition velocities.

2.4.3.2 Primary organic aerosol

Table 2.17 compares the global POA burdens and lifetimes of our work and those of *Cooke et al.* [1999] and *Koch* [2001]. The smaller predicted global POA burden and shorter lifetime of *Koch* [2001] are again a result of the different in-cloud convective scavenging schemes. *Cooke et al.* [1999] considered only fossil fuel sources of POA. Their predicted POA lifetime lies between those of our work and *Koch* [2001].

2.4.3.3 Secondary organic aerosol

Estimated SOA production is 11.2 Tg yr^{-1}, which is lower than the estimated range of 13-24 Tg yr^{-1} by *Griffin et al.* [1999b]. Direct comparison is, however, difficult since *Griffin*

et al. [1999b] did not include 3-dimensional transport, partitioning of SOA onto POA, nor oxidation of parent hydrocarbons by NO_3. For these reasons, the estimate of *Griffin et al.* [1999b] might be considered as a lower bound. If so, this suggests that the SOA production rate predicted in the present study is even lower than might have been expected. Indeed, if we neglect partitioning of SOA into POA, the SOA production rate is reduced by an order of magnitude and the global burden by half. The global burden is only a factor of two lower because of a longer lifetime. (In the absence of POA, gas-phase products remain in the gas phase and are transported away from the source region; therefore, more aerosols are formed at the upper troposphere where wet deposition is less prevalent.) If NO_3 oxidation of parent hydrocarbons as a contribution to SOA is ignored, then global SOA production would be approximately 10 Tg yr^{-1}, assuming that the parent hydrocarbons not oxidized by NO_3 are oxidized by O_3 and OH and form SOA at a lower yield.

Our estimate of global SOA production is substantially lower than that of 61-79 Tg yr^{-1} by *Kanakidou et al.* [2000], the global burden corresponding to which is 1.2-1.6 Tg, as compared to 0.19 Tg in the present work. The source of this major discrepancy in global SOA predictions merits discussion.

Kanakidou et al. [2000] made a number of assumptions in calculating SOA yield (see their Equation 1). First, they neglected transport of semi-volatile gas-phase products away from source regions, which can form SOA at higher altitudes. The effect of this assumption is actually to underestimate SOA production. Second, they assumed that all SOA, once formed, remains in the condensed phase until removal by wet or dry deposition (so that the SOA formed from the previous time steps behaves as POA in the current time step). Because of gas-particle equilibrium, however, SOA can re-partition back into the gas phase. For example, if an air parcel originally at equilibrium is advected to a region of higher

temperature, some of the SOA will re-evaporate to establish the new equilibrium state. We calculate that the combined effect of these two assumptions made by *Kanakidou et al.* [2000] is underestimation of SOA production by about 45%.

The emissions inventory used by *Kanakidou et al.* [2000] included 210 Tg C yr^{-1} of biogenic hydrocarbons (127 Tg C yr^{-1} monoterpenes and 83 Tg C yr^{-1} ORVOC), of which they assumed 50% to be α-pinene and 50% β-pinene. Assuming the molecular weight of ORVOCs is equal to that of monoterpenes, a total of 210 Tg C yr^{-1} is equivalent to a total mass of 238 Tg yr^{-1}, which is to be compared with the value of 201 Tg yr^{-1} in our work. The difference arises from a different percent contribution of ORVOCs to SOA formation and molecular weights of ORVOC. The average molar-based stoichiometric coefficient for SOA formation was assumed to be ≈ 0.34, which equals 0.425 in mass-based units by assuming SOA has molecular weight of 170 g $mole^{-1}$. Therefore, assuming all of the α-pinene and β-pinene react, the maximum SOA production possible is $0.425 \times 238 = 101$ Tg yr^{-1}. This is assuming that: 1) all oxidants O_3, OH and NO_3 contribute to SOA formation; and 2) all products condense to the aerosol phase. *Kanakidou et al.* [2000] included O_3, OH, and NO_3 oxidation as sinks for the parent hydrocarbons, but they considered only O_3 reaction as sources of SOA formation. They predicted that O_3 accounted for $\approx 80\%$ of the oxidation of the parent hydrocarbons. Thus the maximum SOA production rate, neglecting any NO_3 or OH contribution, is $101 \times 0.8 = 81$ Tg yr^{-1} . Not all 81 Tg yr^{-1} can be in the aerosol phase since thermodynamic equilibrium requires that

$$\frac{A_{i,j,k}}{A_{i,j,k} + G_{i,j,k}} = \frac{K_{om,i,j,k} M_o}{(1 + K_{om,i,j,k} M_o}) < 1$$

Even under the most favorable conditions for aerosol formation, $K_{om,i,j,k} = 0.2$ μg^{-1} m^3

and M_o=30 μg m^{-3}, the above ratio is 0.86. The predicted production rate of 61-79 Tg yr^{-1} means that the predicted ratio is 0.75 to 0.98. However, M_o is generally on the order of 0.1 to 1 μg m^{-3}, so the above ratio should be about 0.02 to 0.16.

The same analysis above can be applied to our work. Using global annual emissions of 201 Tg yr^{-4} and an average mass-based stoichiometric coefficient of $\bar{\alpha}$=0.7, the maximum SOA production is 140 Tg yr^{-1}, giving the predicted ratio of aerosol-phase products to total products to be about 0.08, which is more reasonable.

Figure 2.14 shows a comparison of the current SOA prediction to that of *Andersson-Sköld and Simpson* [2001] at four sites in the Nordic countries. *Andersson-Sköld and Simpson* [2001] used the Lagrangian EMEP (Co-operative Programme for Monitoring and Evaluation of the Long Range Transmission of Air Pollutants in Europe) oxidant model. The comparison is shown for the three cases studied by *Andersson-Sköld and Simpson* [2001] and for the months of Janaury, April, July, and October for each of the four sites. The first case used the mechanism of *Kamens et al.* [1999] for O_3 oxidation of α-pinene and did not include other terpenes (labelled "Kamens" on Figure 2.14). The second and third cases used similar emission inventory and aerosol parameters as our work. "α-K" on Figure 2.14 uses the aerosol yield parameters of *Griffin et al.* [1999b]. "α-K-T" also uses the parameters given in *Griffin et al.* [1999b], but partition coefficients K_{om} are adjusted for temperature effects. In Figure 2.14 the predictions of *Andersson-Sköld and Simpson* [2001] are plotted against our predictions multiplied by 0.7 to account for the fact that they did not consider NO_3 as a sink for terpenes. The factor of 0.93 approximates the lower aerosol yield of O_3/OH oxidation if one allows the reactive hydrocarbons to be oxidized only by O_3 and OH. The factor of 0.7 represents an annual and global average, so it is only a first-order estimate for the effect of neglecting NO_3 oxidation on SOA concentrations. This estimate also assumes that the

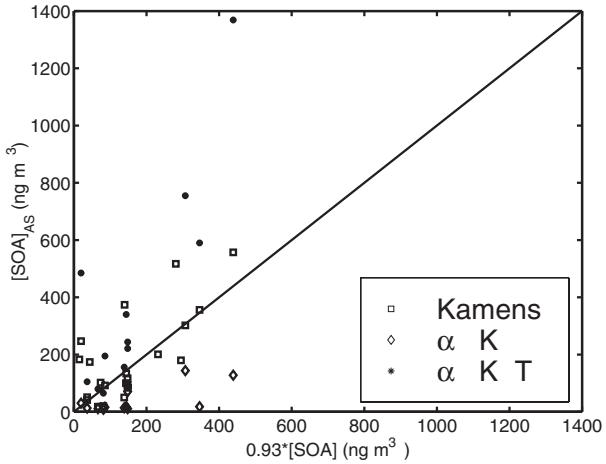

Figure 2.14: Comparison of predicted SOA concentrations with those of *Andersson-Sköld and Simpson* [2001] for six sites in the Nordic countries. The abscissa is 93% of predicted SOA concentrations of this work (see text). The ordinate is the SOA concentrations predicted by *Andersson-Sköld and Simpson* [2001] for three different mechanisms. "Kamens" is based on the gas-phase reaction mechanisms of *Kamens et al.* [1999]. "α-K" is based on the aerosol yield parameters of *Griffin et al.* [1999b]. "α-K-T" is based on the same aerosol yield parameters but adjusted for temperature effects.

lifetime of SOA does not change. The lifetime of SOA can change because wet-scavenging is sensitive to precipitation rates, which vary with locations. As seen from Figure 2.14, the present predictions are in good agreement with those of *Andersson-Sköld and Simpson* [2001], given the differences in gas-phase chemistry, model resolution, and meteorological conditions. The slightly higher levels predicted by *Andersson-Sköld and Simpson* [2001] may be a result of the fact that they used a stronger temperature dependence of K_{om}; we employ $\Delta H/R = 5000$ K in Equation 2.4, whereas they used $\Delta H/R = 9525$ K.

2.4.4 Sources of Uncertainties in Global Burdens and Distributions

Global burdens and distributions are strongly dependent on a number of factors. First and foremost, they are sensitive to the emission inventories of primary carbonaceous aerosols [*Liousse et al.*, 1996]. The BC inventory from fossil fuel used in the present work is approximately 4 times less than that of *Cooke and Wilson* [1996] in North America but comparable

to that of *Cooke et al.* [1999]. The difference is a result of updated emission factors and fuel usage data. The global emissions of POA from fossil fuels employed here are a factor of two higher than those of *Cooke et al.* [1999] because *Liousse et al.* [1996] assume that fossil fuel emissions of POA are proportional to the fossil fuel emissions of BC and that the proportionality constant is globally uniform.

Uncertainties in the emissions of POA also have an effect on the predicted global burden and lifetime of SOA. For a given emission rate of biogenic hydrocarbons but less POA, more semi-volatile oxidation products will stay in the gas-phase and be transported away from the source regions. At higher altitudes, colder temperatures would eventually allow the some for the products to condense into the aerosol phase. Using the predicted global aerosol production of 11.2 Tg yr^{-1} and assuming that all 201 Tg yr^{-1} parent hydrocarbons are oxidized, the overall global aerosol yield that we predict is

$$Y \approx \frac{11.2}{201} = 0.05$$

If we average the mass-based stoichiometric coefficients $\alpha_{i,j,j}$s listed in Table 2.3 and weigh them by emissions and reactivity, the average is $\bar{\alpha}$=0.7. Since $\bar{\alpha} \gg Y$, this means that the total organic aerosol concentration M_o is in the regime where the total aerosol yield is very sensitive to M_o. In other words, SOA production is very sensitive to the concentrations of POA (and therefore to the emission rate of POA). As human activities continue to increase POA emissions, SOA production will likewise increase.

Because aerosol-forming hydrocarbons are oxidized in the atmosphere virtually entirely, uncertainties in their emission inventory translate directly to uncertainties in SOA production. According to *Guenther et al.* [1995], uncertainties associated with monoterpene

emissions in some temperate regions are at least a factor of 3. Segmenting total monoterpene and ORVOC emissions into individual compounds and lumping into groups of reactants (Table 2.5) also contribute to the uncertainty. The contribution of individual compounds to the total monoterpene emission is not geographically constant as we have assumed. By grouping compounds with similar aerosol yield parameters and reactivities together according to Table 2.5, the contributions of each group of parent hydrocarbons to SOA formation (see Table 2.8) are roughly proportional to the emission rates multiplied by the mass-based stoichiometric coefficients. Uncertainties in the emissions of specific monoterpene would certainly lead to inaccuracy in the predicted global SOA production.

The spatial resolution of the GCM also introduces uncertainties to the model prediction since physical processes such as emissions and transport often occur at a spatial scale smaller than the GCM grid cells. For example, the coarse resolution can introduce artificial dilution of emissions and lead to underestimation of aerosol concentrations.

Another factor leading to uncertainty in prediction of global SOA production arises from the aerosol yield parameters. Available experimental data on α and K_{om} values for the biogenic hydrocarbons are for temperatures of about 298 K. We have represented the temperature dependence of K_{om}, but temperature dependence of α is not taken into account. Implicitly assumed is that the nature of the reaction pathway and products remains unchanged at colder temperatures, an assumption that is likely not to be a source of serious error.

Finally, uncertainties in wet-scavenging lead to large uncertainties in global burden, lifetime, and distribution of any soluble tracer. The relevant parameters in the current study include the percentage of primary carbonaceous aerosols emitted that are hydrophobic and the scavenging efficiency (or solubility) of hydrophilic aerosols. More hydrophobic

aerosols or lower scavenging efficiency lead to longer predicted lifetime, more aerosol in the upper troposphere, and a larger global burden. For the semi-volatile gas-phase oxidation products, values of Henry's law coefficients are important. Lower Henry's law coefficients mean that more gas-phase products are transported to the upper troposphere, where colder temperatures allow the semi-volatile gases to condense. This would also increase SOA concentrations in the polar regions.

2.5 Preindustrial versus Present Day

For preindustrial BC and POA emissions, we assume only 10% of the current global emissions from biomass burning occured in the preindustrial period and neglect all fossil fuel sources, resulting in 0.56 and 4.5 Tg yr^{-1} of BC and POA, respectively. The seasonal and geographical distributions of preindustrial BC and POA emissions are assumed to be the same as the present-day biomass emissions of carbon monoxide given by *Wang et al.* [1998a]. Preindustrial monthly mean concentrations of OH and O_3 concentrations are available from *Mickley et al.* [1999]. Although biogenic VOC emissions may have decreased since the 1800's due to deforestation, we assume that the monoterpene and biogenic ORVOC emissions remain the same. Therefore, our preindustrial SOA calculation may lie in the low end of the possible range.

The global distribution of preindustrial carbonaceous aerosol concentrations is shown in Figure 2.15. In contrast to the present day, the average BC and POA concentrations are higher in the SH where biomass burning is more prominent. The relative increase since the preindustrial time is greater in the NH because of fossil fuel emissions. Total global burdens are estimated to have increased by almost an order of magnitude since preindustrial period (Table 2.18).

Table 2.18: Preindustrial and Present Day Global Burdens of Carbonaceous Aerosols

	Burden (Tg)	
Aerosol	Preindustrial	Present Day
BC	0.02	0.21
POA	0.11	1.2
SOA	0.06	0.19

For SOA, preindustrial concentrations are still predicted to be higher in the NH, where biogenic emissions of VOC are higher. If we assumed that biogenic emissions of VOC remained constant and that VOCs are oxidized almost to completion even with lower ozone levels, the overall lower preindustrial SOA concentrations is mainly due to less POA available for absorption of SOA. The preindustrial SOA production rate is estimated to be 0.85 Tg yr^{-1}, which is an order of magnitude of lower than present-day production. Interestingly, SOA concentrations in the upper troposphere are actually predicted to be slightly higher during the preindustrial time (Figure 2.15c). This prediction is explained by the semi-volatile nature of SOA; with lower POA concentrations near the surface, more gas-phase products are transported to higher altitudes where they condense to the aerosol phase. This result again illustrates the sensitivity of SOA concentrations to wet-deposition of gas-phase products and the temperature dependence of the partition coefficient, K_{om}.

2.6 Direct Radiative Forcing of Carbonaceous Aerosols

Radiative forcing is calculated as the difference in the incoming solar irradiance at the top of the atmosphere (TOA) with and without the presence of aerosols. We neglect long-wave forcing as it is expected to be small [*Haywood et al.*, 1997]. Direct aerosol radiative forcing is calculated on-line using the radiation model embedded in the GISS GCM II-

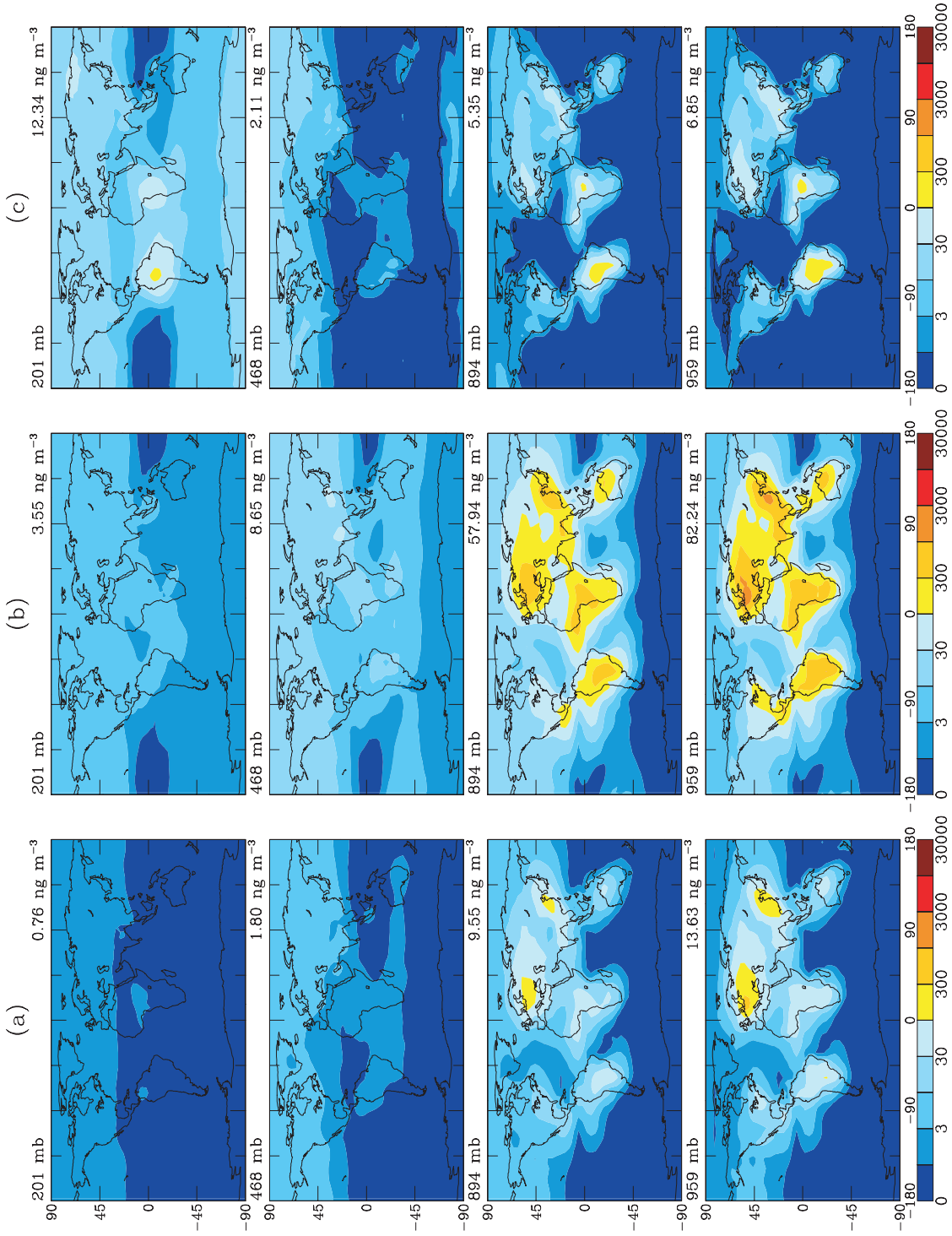

Figure 2.15: Simulated annual average aerosol concentrations (ng m^{-3}) for preindustrial period: (a) BC; (b) POA; (c) SOA.

prime [*Lacis and Hansen*, 1974; *Hansen et al.*, 1983; *Lacis and Mishchenko*, 1995; *Tegen et al.*, 2000]. Reflection, absorption, and transmission by aerosols are calculated using the single Gauss point doubling/adding radiative transfer model. The correlated k-distribution method is used to compute absorption by gases for 6 solar and 25 thermal intervals [*Lacis and Oinas*, 1991]. The radiation time step in the model is 5 hours. The radiative forcing calculations do not feed back into the GCM climate, so that the preindustrial and present day simulations use the same meteorological fields.

To include inorganic aerosols, present-day and preindustrial monthly sulfate fields and associated aerosol water computed with the GISS GCM II-prime are imported from the work of *Adams et al.* [2001].

2.6.1 Aerosol Mixing State

The mixing state of carbonaceous aerosol is important in determining its radiative effect [*Chýlek et al.*, 1995; *Haywood et al.*, 1997; *Myhre et al.*, 1998; *Jacobson*, 2000]. To quantify the effect of aerosol mixing state on direct radiative forcing, we consider two limiting cases. In one case, each aerosol component is assumed to be contained in physically separate particles, forming an external mixture. In the other case the aerosols are internally mixed. A more detailed microphysical representation could treat each particle that contains black carbon, organic carbon and sulfate as a core of black carbon surrounded by a shell of sulfate, OC and water. As shown by *Jacobson* [2000], the radiative forcing of aerosols with a concentric core of black carbon lies between those of internally- and externally- mixed particles. By considering the two extreme cases, we can estimate the range of radiative forcing.

2.6.2 Aerosol Optical Properties

Optical properties (extinction efficiency, single-scattering albedo, and asymmetry parameter) of the aerosols are determined by Mie theory based on wavelength-dependent refractive indices and assumed size distributions. The particle size distribution is assumed to be the standard gamma distribution with area-weighted effective variance, $v_e = 0.2$. We assume that the variance is constant even when particles take up water and grow to larger sizes. The effective dry radius and density, as well as optical properties of dry aerosols at λ=550 nm, of each class are listed in Table 2.19. Dry sulfate aerosol is represented as ammonium sulfate, with refractive indices from *Toon et al.* [1976]. The water uptake of ammonium sulfate aerosol is governed by thermodynamic equilibrium [*Adams et al.*, 1999]. Composite refractive indices of the aqueous sulfate aerosol are the volume-averaged refractive indices of ammonium sulfate and water. Refractive indices of water are taken from *d'Almeida et al.* [1991]. Refractive indices of soot in *d'Almeida et al.* [1991] are used for BC. For an internal mixture of BC, OC, and sulfate aerosols, the refractive indices are calculated by volume-weighting the refractive indices of BC, OC, $(NH_4)_2SO_4$, and water.

In the absence of data for OC, refractive indices for "water-soluble" aerosol from *d'Almeida et al.* [1991] are used for OC. "Water-soluble" aerosols as described in *d'Almeida et al.* [1991] include sulfates, nitrates, as well as water-soluble organic aerosols. Since water uptake by organic aerosol is not well established, we consider two cases. At one limit, we assume no water uptake. In the other case we follow the treatment of water-soluble aerosols given in *d'Almeida et al.* [1991] (Figure 2.16). Below 50% relative humidity, water-uptake is assumed to be zero. Above 99%, the growth factor $f_g = r_{\text{wet}}/r_{\text{dry}}$ is capped at 2.52. This treatment of water uptake is similar in magnitude to that given by *Fitzgerald* [1975] and is considered to be the upper bound since not all organic compounds are as soluble as ammonium sulfate.

Table 2.19: Aerosol Physical and Optical Properties at λ=550 nm in the Dry State.

Aerosol Type	$r_{e,\mathrm{dry}}$ (μm)	ρ (g cm^{-3})	σ_e (m^2 g^{-1})	ω	g
$(NH_4)_2SO_4$	0.3	1.8	4.2	1.00	0.69
OC	0.5	1.8	2.53	0.94	0.68
BC	0.1	1.0	12.5	0.38	0.47
internal mixture	0.3				

$r_{e,\mathrm{dry}}$ = effective dry radius; ρ = density; σ_e = extinction coefficient; ω = single scattering albedo; g = asymmetry factor

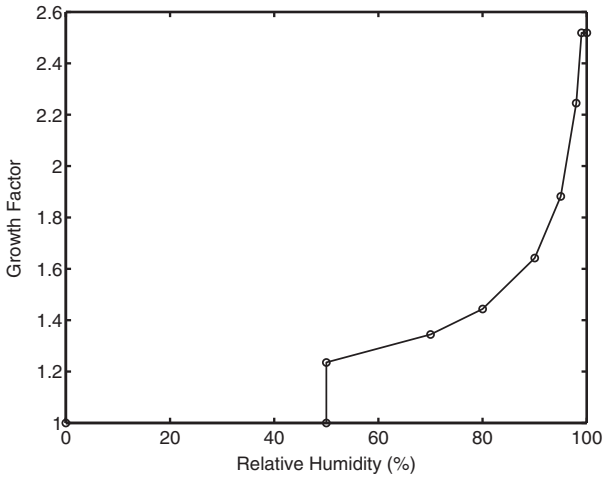

Figure 2.16: Hygroscopic growth of organic aerosol [*d'Almeida et al.*, 1991]. The growth factor is defined as $f_g = r_{\mathrm{wet}}/r_{\mathrm{dry}}$.

For the case of internally mixed aerosols, we assume that the total amount of water uptake is equal to that of the externally mixed aerosols.

2.6.3 Global Distributions of Direct Radiative Forcing

The results presented here are one-year averages after an initial spin up of 7 months. Figure 2.17 shows the annually-averaged global distributions of radiative forcing for anthropogenic sulfate, OC, and BC. The cooling at TOA calculated here for sulfate aerosols is slightly different from that of *Adams et al.* [2001] because we do not consider the presence of ammonium and nitrate and assume that all sulfate exists as ammonium sulfate. We do,

however, include all water that is associated with the equilibrium of $(NH_4)_2SO_4$-NO_3-NH_4-H_2O system given by *Adams et al.* [1999].

The globally-averaged annual direct radiative effect of anthropogenic black carbon is predicted to be +0.50 W m^{-2}. The effect is predicted to be the greatest in regions of high black carbon concentrations and high surface albedo, such as eastern China and northern Europe.

The globally averaged TOA radiative forcing of pure anthropogenic organic carbon is relatively small, -0.09 W m^{-2}, and the direction of warming or cooling varies geographically based on the surface albedo and cloud cover. The single scattering albedo of organic carbon at $\lambda = 550$ nm is $\omega = 0.94$ based on the properties given in Section 2.6.2. Over regions of high surface albedo, organic carbon aerosol causes a net warming. For lower albedos, the effect is one of net cooling. In either case, the magnitude of forcing is generally small. Including water uptake by organic aerosol increases the tendency toward cooling (increased ω), and the predicted globally-averaged annual radiative forcing becomes -0.18 W m^{-2}.

Figure 2.18 shows the predicted global distributions of TOA radiative forcing for all three types of aerosols combined. As expected, the internally-mixed aerosol exhibits less cooling than the external mixture. The predicted cooling decreases from 0.68 W m^{-2} for the external mixture to 0.39 W m^{-2} for internally mixed aerosols when water uptake of OC is not considered. When the water uptake by OC is included, the combined cooling decreases from 0.78 to 0.48 W m^{-2}. In an internal mixture, black carbon is present in every aerosol particle such that all particles absorb radiation; for the external mixture, only black carbon (and, to a lesser extent, organic carbon) absorbs solar radiation. Even though the overall global net anthropogenic forcing is negative, regions of significant warming are predicted, such as the polar regions, eastern China, and India. Table 2.20 summarizes the radiative

Table 2.20: Summary of Predicted TOA Direct Radiative Forcing (W m^{-2})

Aerosol Type	Preindustrial	Modern Day	Net Anthropogenic Forcing
$(NH_4)_2SO_4$	-0.53	-1.63	-1.10
BC	0.07	0.57	0.51
OC (dry)	0.00	-0.09	-0.09
OC (wet)	-0.03	-0.21	-0.18
External mixture (dry OC)	-0.47	-1.15	-0.68
External mixture (wet OC)	-0.49	-1.26	-0.78
Internal mixture (dry OC)	-0.47	-0.86	-0.39
Internal mixture (wet OC)	-0.49	-0.97	-0.48

forcing predictions.

2.6.4 Seasonal Variations of Direct Radiative Forcing

The predicted seasonal trend of anthropogenic radiative forcing is shown in Figures 2.19 and 2.20. In the NH, the maximum cooling of sulfate occurring in summer coincides with a high SO_2 oxidation rate and and overlaps with the peak warming of BC, which is dominated by industrial emissions. The BC peak occurs slightly earlier in the NH because biomass emissions are also important for BC. The peak of OC in the NH is determined by a combination of fossil fuel and biomass burning sources. The peak in March represents the tailing part of the biomass burning season but also of increasing fossil fuel sources. Sulfate forcing in the SH is small in comparison to that in the NH, but still stronger than those of BC and OC. In the SH, OC and BC forcings peak in August and September, which coincide with peak of the burning season.

Figure 2.20 shows the combined seasonal effect of all three classes of aerosols. Regardless of the mixing state and water uptake of OC, radiative forcing in the SH remains relatively constant. Forcing always tends toward cooling except for the case of internally mixed aerosols with no water uptake by OC during the months of June to September. In the NH,

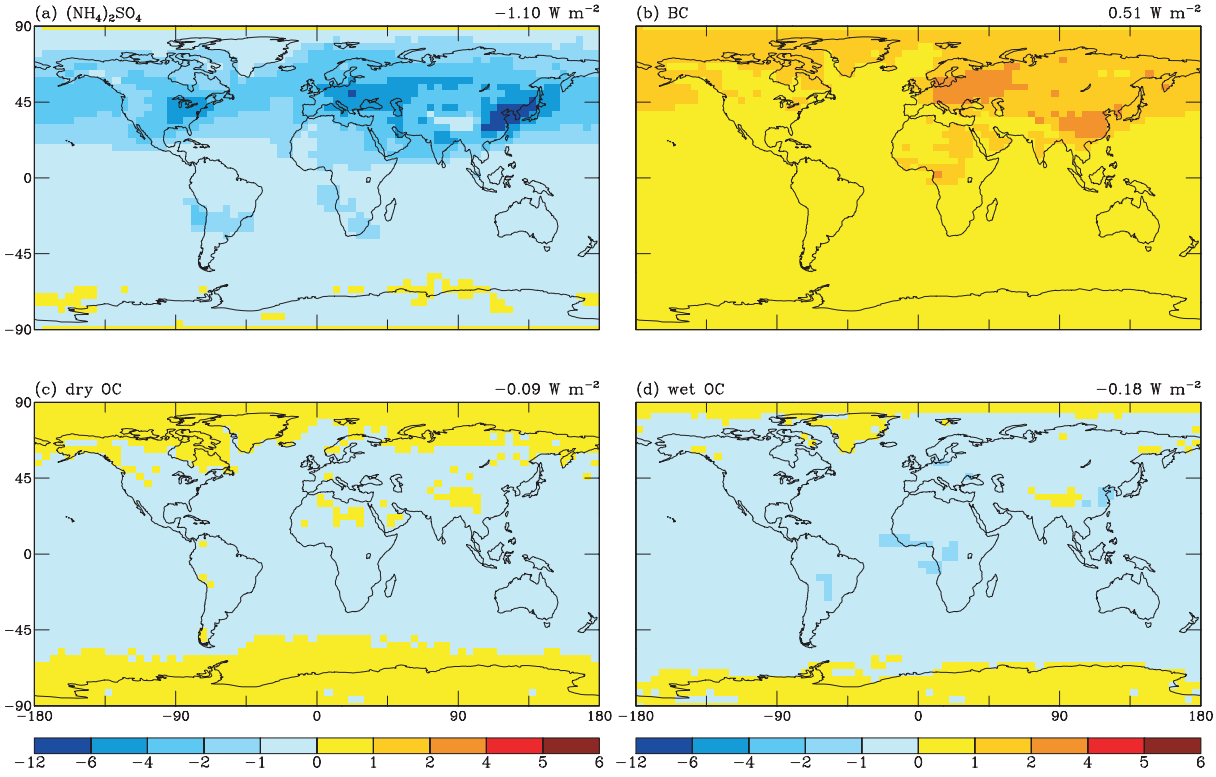

Figure 2.17: Geographical distributions of predicted anthropogenic contribution to annual average TOA direct radiative forcing (W m^{-2}) for (a) $(NH_4)_2SO_4$-water; (b) BC; (c) OC without water uptake; and (d) OC with water uptake. The global averages are given on the upper right corner of each figure.

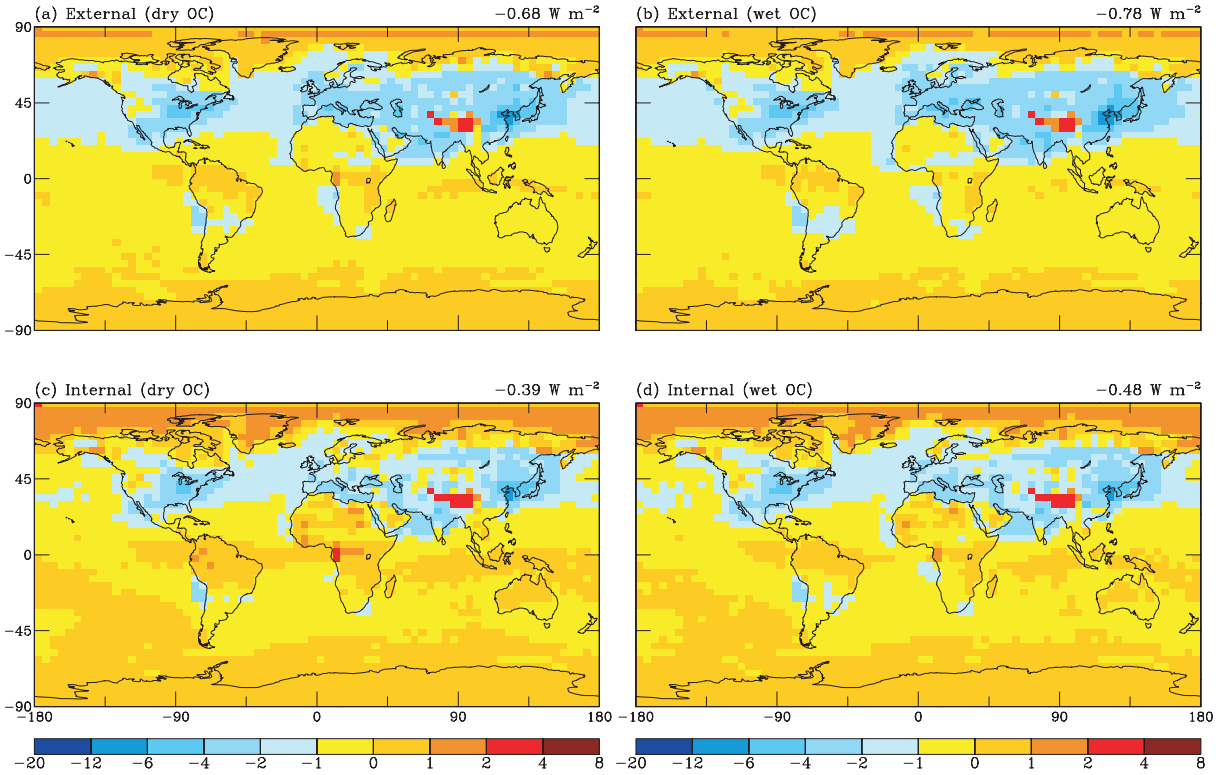

Figure 2.18: Geographical distributions of predicted anthropogenic contribution to annual average TOA direct radiative forcing (W m^{-2}) for various cases of aerosol mixing state: (a) externally mixed without water uptake by OC; (b) externally mixed with water uptake by OC; (d) internally mixed without water uptake by OC; (d) internally mixed with water uptake by OC. The global averages are given on the upper right corner of each figure.

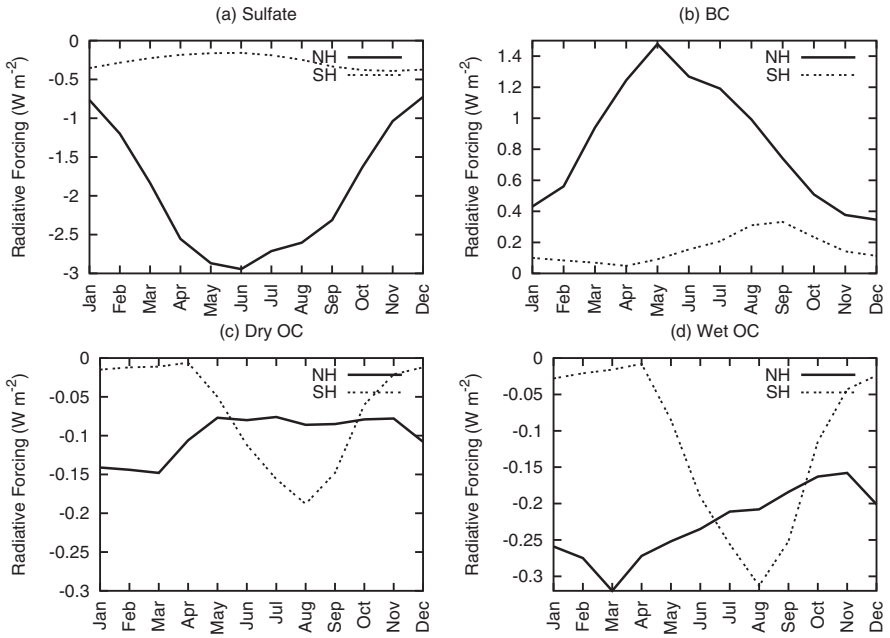

Figure 2.19: Seasonal cycle of anthropogenic TOA radiative forcing (W m^{-2}) for (a) $(NH_4)_2SO_4$-water; (b) BC; (c) OC without water uptake; and (d) OC with water uptake.

there is strong cooling during summer. The presence of black carbon reduces the cooling of sulfate and OC by almost one third in case of the internal mixture with dry OC and almost 70% for an internal mixture with wet OC.

2.6.5 Comparison of Predicted Radiative Forcing with Previous Work

2.6.5.1 Black carbon

Table 2.21 compares the predicted direct radiative forcing of black carbon with those of previous studies. For internally-mixed aerosols, separating the contribution of each component to the total radiative forcing is difficult because total radiative forcing is not a linear sum of individual components. For the purpose of comparison with other works, however, we take the direct radiative forcing of BC in an internal mixture to be the difference in radiative forcing between the internal mixture of sulfate, OC, and BC and that of an external

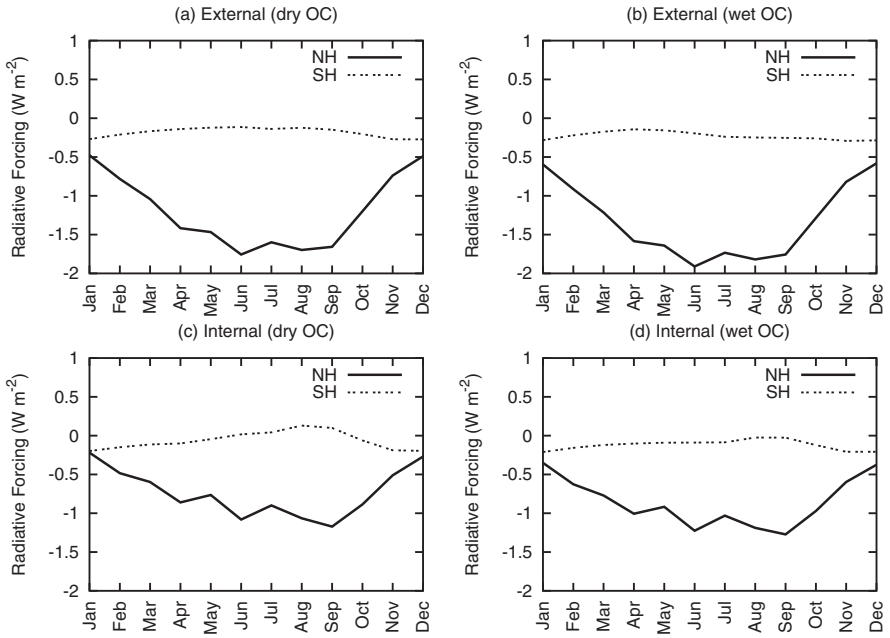

Figure 2.20: Seasonal cycle of anthropogenic TOA radiative forcing (W m^{-2}) for various cases of aerosol mixing state: (a) externally mixed without water uptake by OC; (b) externally mixed with water uptake by OC; (d) internally mixed without water uptake by OC; (d) internally mixed with water uptake by OC.

mixture of sulfate and OC. This definition is still not perfect since most of the studies listed in Table 2.21 considered only sulfate and BC and excluded OC.

Many of the previous estimated BC radiative forcings listed in Table 2.21 are relatively small because they considered only fossil fuel BC and not biomass burning. In Figure 2.21, predicted BC radiative forcing is shown as a function of the global BC burden for the studies in which the global burdens can be determined. Even when differences in global burdens are taken into account, discrepancies among the different studies still exit. Another important factor affecting radiative forcing is the actual 3-D distribution, which is different for fossil fuel and biomass burning BC. *Haywood and Shine* [1995], *Haywood et al.* [1997], *Haywood and Ramaswamy* [1998], and *Myhre et al.* [1998] all assumed that the distribution of fossil BC scales with that of sulfate. The assumption is oversimplified because not only is the ratio

of BC and sulfate emission rates different for varying fuel types, wet scavenging of sulfate is more effective as sulfate is much more soluble. The geographical distribution is important because the radiative forcing is strongly dependent on the surface albedo, the presence of clouds, and the interaction of scattering and absorbing aerosols in the case of an internal mixture [*Haywood et al.*, 1997; *Haywood and Ramaswamy*, 1998]. Finally, uncertainties in the size distribution of the aerosols lead to variabilities in the predictions.

2.6.5.2 Organic carbon

Radiative forcing of organic aerosol has been less studied than BC. *Cooke et al.* [1999] calculated the radiative forcing of fossil OC to be -70 W (g C)$^{-1}$ (-0.012 W m^{-2} and 0.087 Tg C) and *Koch* [2001] calculated the forcing of fossil fuel and biomass OC to be -210 W (g C)$^{-1}$ (-0.30 W m^{-2} and 0.95 Tg $\approx$ 0.73 Tg C). Our values of -36 to -76 W (g OC)$^{-1}$ (-0.08 to -0.17 W m^{-2} and 1.48 Tg $\approx$ 1.14 Tg C) are comparable to those of *Cooke et al.* [1999]. The major difference between our work and *Koch* [2001] lies in the optical properties of OC. At λ= 550 nm, we used an extinction coefficient σ_e = 2.53 m^2 g^{-1}, whereas *Koch* [2001] used σ_e = 8 m^2 g^{-1} for dry OC, the refractive indices of ammonium sulfate for OC instead of the "water-soluble" aerosol *Cooke et al.* [1999] and the present study employ. The optical properties also depend on water uptake by the organic carbon. Both *Cooke et al.* [1999] and *Koch* [2001] considered only dry OC.

2.7 Conclusions

The global distribution of carbonaceous aerosols is simulated online in the GISS GCM II-prime. We include black carbon (BC) and primary organic aerosols (POA) from fossil fuel and biomass burning, as well as secondary organic aerosols (SOA) from the oxidation

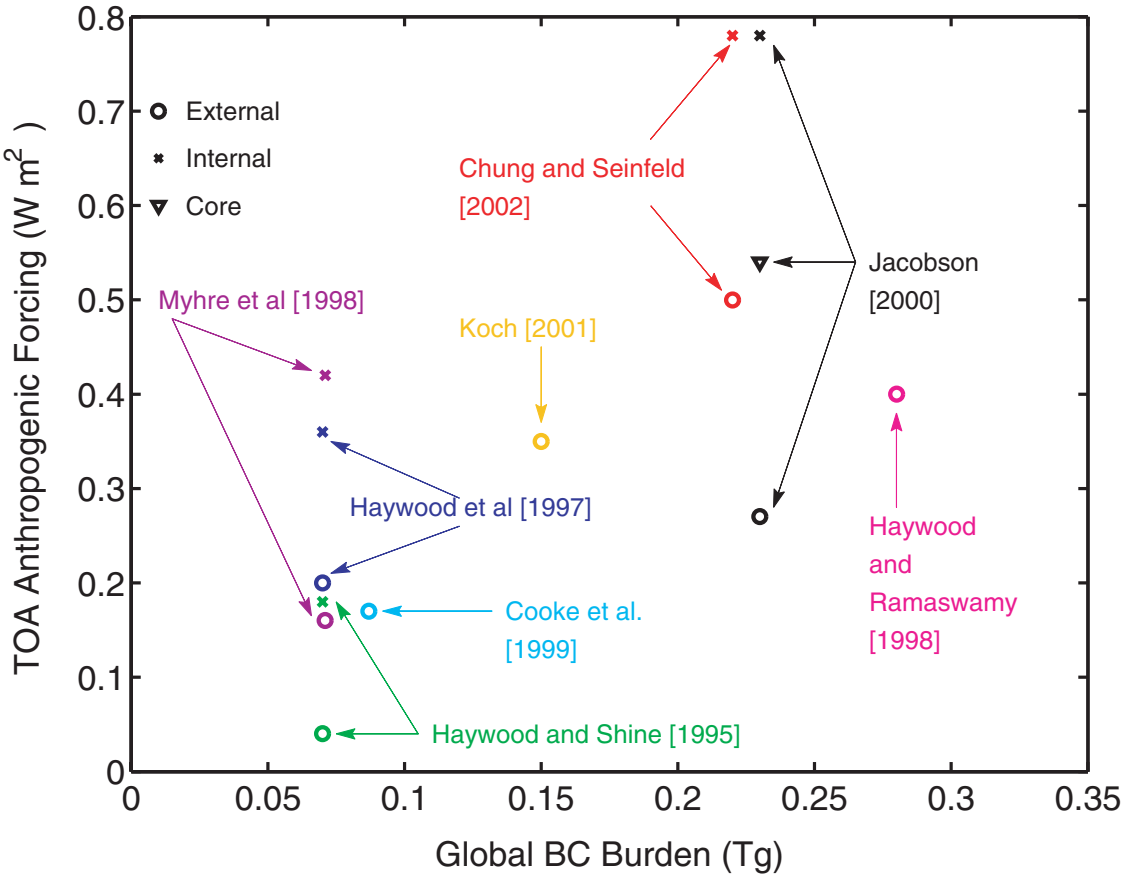

Figure 2.21: Comparison of BC radiative forcing predictions versus BC global burden by various authors. The color of the data points are coded to the authors, and their shapes correspond to the assumptions made about the mixing state of the aerosols.

Table 2.21: Comparison of Predicted Direct Radiative Forcing of Black Carbon with Other Studies (W m^{-2})

Reference	Emissions	Mixing Scenario	Anthropogenic Forcing
This work	FF and BB	External	0.51
		Internal	0.8
Haywood and Shine [1995][a]	FF	External	0.04
		Internal	0.18
Haywood et al. [1997]	FF	External	0.20
		Internal	0.36
Haywood and Ramaswamy [1998]	FF and BB	External	0.40
Myhre et al. [1998]	FF	External	0.16
		Internal	0.42
Penner et al. [1998]	FF	External	0.20
Cooke et al. [1999]	FF	External	0.17
Jacobson [2000]	FF and BB	External	0.27
		Internal	0.78
		BC Core	0.54
Koch [2001]	FF and BB	External	0.35

[a] Clear-sky forcing. FF=fossil fuel; BB=biomass burning

of biogenic hydrocarbons. Simulated black carbon concentrations are generally low at rural and marine sites when compared with available measurements. In comparison to BC and OC concentrations measured at rural sites in the United States, predictions are consistently low, suggesting that the carbonaceous aerosol emissions inventory in the U.S. might be too low. Overall, the results suggest that wet-scavenging, the dominant sink for carbonaceous aerosols, may be overestimated. More accurate predictions of scavenging require better knowledge of the hydrophilic fraction of primary aerosols and the solubility of hydrophilic aerosols.

We also present global simulation of SOA from oxidation of biogenic hydrocarbons by O_3, OH, and NO_3. Unlike primary organic aerosols, which have the highest concentrations at the surface near source regions, SOA is predicted to accumulate in cold regions of the upper troposphere. At the surface, SOA contributes only about 10 to 20% of the total

OC, whereas in polar regions it is predicted to contribute up to 50%. The reason is that semi-volatile gas-phase oxidation products are transported to higher altitudes where colder temperatures allow more products to condense. SOA burden and lifetime are sensitive to the temperature dependence of gas-particle partition coefficients. SOA production is also sensitive to the solubility of the gas-phase oxidation products since solubility determines how effectively they are removed from the atmosphere by wet-scavenging and how far they are transported away from their source regions.

Human activities since the preindustrial period are predicted to have increased global burdens of BC and OC by an order of magnitude and almost tripled the SOA production rate. Anthropogenic perturbations are especially pronouced in the NH due to fossil fuel use.

Anthropogenic black carbon is predicted to contribute to a globally and annually averaged net radiative forcing of +0.5 W m^{-2} when considered to be externally mixed and +0.78 W m^{-2} when occurring in an internal mixture of BC, OC, and sulfate. Externally mixed OC has a radiative forcing of -0.08 to -0.17 W m^{-2}, depending on the amount of water uptake. Globally averaged and taken together, anthropogenic BC, OC and sulfate are predicted to exert a radiative forcing of -0.4 to -0.76 W m^{-2}, depending on the exact assumptions of aerosol mixing and water uptake by OC. Even though the net radiative effect is one of cooling, warming of up to 3 W m^{-2} is predicted to occur in regions of large BC concentrations and high surface albedo. The annual combined cycle of BC, OC, and sulfate radiative forcing is nearly constant in the SH but varies strongly with season in the NH, with maximum cooling occurring during summer. Regional climate perturbations are expected to lead to climate feedbacks that warrant further study.

2.8 Acknowledgments

This work was supported by the National Aeronautics and Space Administration Earth Observing System Interdisciplinary Science program (NASA EOS-IDS). Serena Chung was supported by a National Science Foundation Graduate Fellowship. The authors thank Peter Adams and Dorothy Koch for assistance.

Chapter 3

Climate Response of Direct Radiative Forcing of Anthropogenic Black Carbon

Reference: Chung, S. H., and J. H. Seinfeld, (2005), Climate response of direct radiative forcing of anthropogenic black carbon, submitted to *J. Geophys. Res.*

3.1 Abstract

The equilibrium climate effect of direct radiative forcing of anthropogenic black carbon (BC) is examined by 100-year simulations in the Goddard Institute for Space Studies General Circulation Model II-prime coupled to a mixed-layer ocean model. Anthropogenic BC is predicted to raise globally and annually averaged equilibrium surface air temperature by 0.20 K if BC is assumed to be externally mixed. The predicted increase is significantly greater in the Northern Hemisphere (0.29 K) than in the Southern Hemisphere (0.11 K). If BC is assumed to be internally mixed with the present-day level of sulfate aerosol, the predicted annual mean surface temperature increase rises to 0.37 K globally, 0.54 K for the Northern Hemisphere, and 0.20 K for the Southern Hemisphere. The climate sensitivity of BC direct radiative forcing is calculated to be 0.6 K W^{-1} m^2, independent of the as-

sumption of BC mixing state. The largest surface temperature response occurs over the northern high latitudes during winter and early spring. In the tropics and midlatitudes, the largest temperature increase is predicted to occur in the upper troposphere. Direct radiative forcing of anthropogenic BC is also predicted to lead to a change of precipitation patterns in the tropics; precipitation is predicted to increase between 0 and 20degN and decrease between 0 and 20degS, shifting the inter-tropical convergence zone northward. If BC is assumed to be internally mixed with sulfate instead of externally mixed, the change in precipitation pattern is enhanced. The change in precipitation pattern is not predicted to alter the global burden of BC significantly because that occurs predominantly in regions removed from BC sources.

3.2 Introduction

Atmospheric abundances of tropospheric greenhouse gases (GHGs) and aerosols have increased since the preindustrial period due to anthropogenic activities, and are estimated to make significant contributions to perturbing the radiative balance of the Earth-atmosphere system over the next century [*Intergovernmental Panel on Climate Change (IPCC)*, 2001]. While GHGs such as CO_2 and CH_4 warm the atmosphere by trapping outgoing infrared radiation, anthropogenic aerosols, such as sulfates or black carbon (BC), cool or warm the atmosphere by scattering or absorbing solar radiation, respectively. Among radiatively active species of anthropogenic origin in the atmosphere, BC is increasingly recognized as an important contributer to global climate change [*Jacobson*, 2002; *Hansen and Nazarenko*, 2004; *Roberts and Jones*, 2004; *Wang*, 2004]. Anthropogenic BC is also considered an important factor in the perturbation of regional climate [*Ramanathan et al.*, 2001a,b; *Menon et al.*, 2002].

The first-order estimate of the climate impact of an atmospheric constituent is the direct radiative forcing it induces, which measures the net change in incoming and outgoing irradiance, usually calculated at top of the atmosphere (TOA) or at the tropopause. The concept of radiative forcing as a measure of climate change is justified by the assumption that, for small perturbations, the equilibrium global and annual mean surface air temperature change ($\Delta[\bar{T}_s]$) is approximately linearly related to the global and annual mean radiative forcing ($\Delta[\bar{F}]$), i.e.,

$$\Delta[\bar{T}_s] = \lambda \Delta[\bar{F}], \tag{3.1}$$

where λ is the climate sensitivity in units of K W^{-1} m^2. Indeed, climate model experiments have shown that, for relatively spatially homogeneous radiative forcing, λ is reasonably independent of the nature of the forcing within an individual climate model (within 20%). For example, *Hansen et al.* [1984,1997], *Forster et al.* [2000], and *Joshi et al.* [2003], show that the climate responses for doubled CO_2 and a 2% increase in solar irradiance are remarkably similar even though solar forcing affects shortwave radiation and CO_2 mainly affects longwave radiation.

An important factor in the linear relationship of Equation (3.1) is that $\Delta[\bar{F}]$ needs to be defined appropriately. The IPCC Assessment [*IPCC*, 2001] defines radiative forcing as the "change in net (down minus up) irradiance (solar plus longwave; in W m^{-2}) at the tropopause AFTER allowing for stratospheric temperatures to readjust to radiative equilibrium, but with surface and tropospheric temperature and state held fixed at the unperturbed values." The rationale for using this adjusted (instead of instantaneous) forcing is that the radiative relaxation time of the stratosphere is a few weeks, much faster than the decadal timescale for the surface-troposphere system, which is governed by the thermal

inertial of the ocean [*Hansen et al.*, 1997; *Shine and Forster*, 1999]. Because radiative forcing for tropospheric aerosols is normally reported in the literature as the instantaneous forcing at TOA, unless otherwise noted, forcings for aerosols reported in this study are instantaneous direct radiative forcings at TOA. Note that for tropospheric aerosols that only interact with shortwave radiation, such as sulfate and BC, the instantaneous forcing at TOA, instantaneous forcing at tropopause, and adjusted forcing at tropopause are approximately equal *Hansen et al.* [1997]; therefore, no accuracy is lost in using the instantaneous forcing instead of the adjusted forcing for BC or sulfate.

Global annual mean adjusted direct radiative forcing at the tropopause of CO_2 and other GHGs has been estimated at +2.43 W m^{-2} [*IPCC*, 2001]. For BC, the estimate (at TOA) ranges from +0.16 to +0.80 W m^{-2} [*Haywood and Shine*, 1995; *Haywood et al.*, 1997; *Haywood and Ramaswamy*, 1998; *Myhre et al.*, 1998; *Penner et al.*, 1998; *Cooke et al.*, 1999; *Jacobson*, 2000; *Koch*, 2001; *Chung and Seinfeld*, 2002; *Wang*, 2004]. The differences in the estimates are due to differences in predicted global BC concentrations, which are sensitive to emission and wet scavenging rates, to assumptions of the extent to which BC is mixed with other aerosols, to meteorological variables, such as surface albedo, and to vertical distribution of BC with respect to cloud layers. Even though the exact value of present day direct radiative forcing of BC is not known, all studies indicate a potential warming of the atmosphere caused by increased BC atmospheric loading since the preindustrial period.

There are significant differences between the two radiatively active constituents of the atmosphere, GHGs and BC. As mentioned previously, the global distribution of CO_2 is relatively homogeneous such that globally averaged direct radiative forcing is a good measure of the climate response [*Hansen et al.*, 1984, 1997; *Forster et al.*, 2000; *Joshi et al.*, 2003]. Aerosols, however, are not homogeneously mixed in the atmosphere. BC, mainly anthro-

pogenic in origin and with an atmospheric lifetime on the order of one week, is concentrated in continental regions where fossil fuel emissions and biomass burning are dominant. BC loading is also much higher in the Northern Hemisphere (NH) than in the Southern Hemisphere (SH). The inhomogeneity of the BC distribution means that, even if its globally average radiative forcing is relatively small, its regional impact can be significant. Annually averaged, the local column forcing for fossil fuel and biomass BC has been predicted to exceed 3.0 W m^{-2} at TOA in regions of high BC loading, such as Europe and eastern Asia [*Haywood and Ramaswamy*, 1998; *Koch*, 2001; *Chung and Seinfeld*, 2002]. On spatial scales smaller than the horizontal resolution of climate models, the forcing is even larger.

In comparison to other aerosols, the magnitude of BC direct radiative forcing is similar to that of sulfate, for which the direct radiative forcing at TOA has been estimated to be in the range of -0.29 to -0.95 W m^{-2} [*IPCC*, 2001]. However, BC aerosols differ profoundly from sulfates in their interaction with solar radiation in that sulfate aerosols radiatively cool both the surface and atmosphere by scattering solar radiation back to space, whereas BC radiatively warms the atmosphere by absorbing solar radiation but radiatively cools the surface by blocking solar radiation from reaching the surface. Negative forcing at the surface due to absorbing aerosols can be substantial and is supported by observational evidence [*Ramanathan et al.*, 2001b; *Markowicz et al.*, 2002]. The simultaneous surface cooling and warming at higher elevation have the potential to increase the static stability of the atmosphere. BC also differs from sulfate in that the contribution from cloudy regions to the total forcing for BC is higher than that of sulfate because a highly reflective cloud below a BC layer reflects more sunlight back to the BC layer, allowing BC to absorb even more radiation [*Haywood and Ramaswamy*, 1998].

Hansen et al. [1997] and *Cook and Highwood* [2004] studied the climate sensitivity λ

of absorbing aerosols by studying the change in λ as the single scattering albedo changes between 1.0 and 0.8, but with constant aerosol optical depth. Both studies concluded that absorbing aerosols do not follow the linear relationship in Equation (3.1). In fact, the climate sensitivity λ may even be negative, depending on the single scattering albedo. The range of the values of single scattering albedo studied by *Hansen et al.* [1997] and *Cook and Highwood* [2004] is effectively for pure scattering aerosol or a mixture of scattering aerosol with a small component of an absorbing aerosol (e.g., BC). In comparison, the single scattering albedo of pure BC is only 0.4 (assuming optical properties from *d'Almeida et al.* [1991] and gamma size distribution with area-weighted effective radius of 0.1 μm and variance of 0.2). Therefore, the studies of *Hansen et al.* [1997] and *Cook and Highwood* [2004] do not applied directly to pure BC. Nevertheless, these studies suggest that, for BC, global and annual mean direct radiative forcing at TOA (or tropopause) may be an inadequate indicator of climate response.

There have been numerous studies of the projected anthropogenic impact on climate change. Most studies consider only CO_2 and other GHGs while some also consider sulfate aerosol and ozone (see Chapter 9 of *IPCC* [2001]). Much less is understood about the climate impact of BC as there are relatively few studies on BC and climate. Recent global climate studies that have incorporated BC include *Jacobson* [2002], *Menon et al.* [2002], *Wang* [2004], *Roberts and Jones* [2004], and *Jacobson* [2004].

On the basis of six-year transient climate simulations with a mixed-layer ocean model, *Jacobson* [2002] predicts that removing fossil fuel emissions of BC and organic carbon (OC) would cool surface air by about 0.35 K after five years. The emission inventory used in that study is based on that of *Cooke et al.* [1999], giving 5.1 Tg yr^{-1} and 15.8 Tg yr^{-1} of fossil fuel BC and organic aerosol, respectively. The study of *Jacobson* [2002] is updated with the

new emissions inventory of *Bond et al.* [2004] and to include the effect of BC absorption in snow and sea ice in *Jacobson* [2004]. The 10-year, globally averaged temperature response of fossil fuel and biofuel BC and OC is predicted to be about +0.27 K (+0.32 in the last 3 years). In both studies, aerosol optical properties were calculated assuming a shell and core model in which the core is comprised of BC and the shell consists of sulfate, nitrate, OC, sea salt, and mineral dust. Since fossil fuel BC and OC are considered together, the climate effects due to BC alone is not determined.

Menon et al. [2002] use observed aerosol optical depth data in China, India, and the Indian Ocean to study the impact of increased BC in that region on global climate change. The effect of BC is determined from two 120-year climate simulations using observed sea surface temperature (SST). *Menon et al.* [2002] predict that BC over China, India, and the Indian Ocean cools surface temperature in China by 0.5 to 1 K but warms most of the world during June-July-August, especially in the Sahara Desert region and in west and central Canada. The study also predicts increased precipitation in southern China, India, and Myanmar and decreased precipitation to the south of those regions. Results of *Menon et al.* [2002] indicate that local tropospheric warming and dynamical export can lead to regional climate change away from the regions of radiative forcing.

Another study on the climate impact of BC is *Wang* [2004]. In that study, the climate effect of 14 Tg yr^{-1} of BC is considered using different cases of SST. When SST is explicitly assigned based on observational data, BC is predicted to not cause a significant change in annually averaged global mean surface temperature. If a mixed-layer ocean model is used to calculate SST, *Wang* [2004] predicts that BC causes a slight warming of 0.09 K at the surface based on the average of the last twenty years of a sixty-year simulation. The results of *Wang* [2004] indicate that the impact of BC is more significant at the regional scale

than at the global scale, such as the predicted change in precipitation patterns around the inter-tropical convergence zone (ITCZ). Because *Wang* [2004] considers BC to be externally mixed, its predicted 0.22 W m^{-2} BC forcing at TOA is on the lower end, and its is likely underestimated.

To determine the climate sensitivity of direct radiative forcing of fossil fuel BC, *Roberts and Jones* [2004] use 4 times the fossil fuel emission rate of BC of *Cooke et al.* [1999] (20.2 Tg yr^{-1}). The rationale for quadrupling the emission rates is to increase signal-to-noise ratio of the climate model. Their results show that global and annual mean radiative forcing of fossil fuel BC scales linearly with emission rate; however, they do not show whether the climate sensitivity factor λ is constant for BC. From 30-year simulations using an atmosphere-ocean slab model, *Roberts and Jones* [2004] predict the climate sensitivity of direct radiative forcing of quadrupled fossil fuel BC to be 0.56±0.06 K W^{-1} m^2, 40% less than that of CO_2 using the same climate model. Even though *Roberts and Jones* [2004] predict warming at the surface on the global scale, they also predict cooling over the surfaces of China, India, and parts of Africa, which they attribute to reduction of incident shortwave radiation by BC. Furthermore, similar to the results of *Wang* [2004], *Roberts and Jones* [2004] also predict a northward shift of the ITCZ.

The purpose of this work is to study the climate response resulting from increased BC emissions since the preindustrial period. To allow for a more detailed examination of the climatic response due to absorbing aerosols, this study focuses on direct radiative forcing. Other effects, such as the first and second indirect forcing, are not considered. To address the uncertainty in the magnitude of predicted direct radiative forcing with respect to the mixing state of BC, two limiting cases are considered. In one case, BC is assumed to be physically separate from other particles, forming an external mixture. For the second

case, BC is assumed to be homogeneously mixed with sulfate particles, forming an internal mixture. These two limiting cases provide upper and lower bounds for the radiative forcing of BC. Throughout, comparison with results of previous studies are made.

3.3 Model Description

Global climate is simulated online in the Goddard Institute for Space Studies General Circulation Model II-prime (GISS GCM II") [*Hansen et al.*, 1983; *Rind and Lerner*, 1996]. To study the change in equilibrium climate due to direct radiative forcing of BC, results of three simulations are analyzed. In all three cases, monthly-mean, present-day (year 2000) concentrations of sulfate are used in the solar radiative flux calculations; also all three simulations predict BC concentrations online based on present-day emissions of BC. In the first simulation, which will be referred to as CONTROL, monthly mean concentrations of preindustrial BC and present-day sulfate are imported into the radiation scheme to calculate the baseline climate. Present-day sulfate and preindustrial BC are assumed to be externally mixed for this case. Also in the CONTROL simulation, anthropogenic direct radiative forcing of BC is calculated using online predicted present-day BC concentrations; however, the predicted anthropogenic BC forcing is not allowed to interact with the climate simulation, i.e., only preindustrial BC and present-day sulfate concentrations are incorporated into the radiative scheme for the climate simulation in CONTROL. In simulations EXTERNAL and INTERNAL, predicted present-day BC concentrations (instead of imported preindustrial BC concentrations) are allowed to interact with the climate simulation. In simulation EXTERNAL, BC is assumed to be externally mixed, whereas in simulation INTERNAL, BC is assumed to be internally mixed with present-level of sulfate aerosol. Note that the distinction between externally- and internally-mixed cases only refers to the optical properties

of the assembly of BC and sulfate and not to the physical and chemical properties of the aerosols. The scavenging of BC particles (see Section 3.3.3) is treated the same regardless of the mixing assumption. The differences in the predicted climate between CONTROL and that of EXTERNAL and INTERNAL are analyzed to determined the contribution of BC to climate change.

3.3.1 Climate Model: GISS GCM II-Prime

The GISS GCM II' is summarized in *Hansen et al.* [1983] with updates in *Rind and Lerner* [1996], *Del Genio and Yao* [1993], and *Del Genio et al.* [1996]. The GCM has horizontal resolution of 4deg latitude by 5deg longitude and nine σ layers in the vertical, from the surface to 10 mbar. The vertical layers are centered at approximately 959, 894, 786, 634, 468, 321, 201, 103, and 27 mbar, with a 50-mbar surface layer.

While prescribed seasonal ocean temperatures and ice cover are sufficient for studying the transport and distribution of BC, the climate, however, depends strongly on the underlying sea surface temperature (SST), which can change as BC alters the radiative balance of the climate system. Clearly, a reliable forecast of future climate depends upon the ability of the climate model to predict changes in ocean as well as atmosphere.

To implement a model that allows realistic SST adjustment without using the computationally intensive coupled ocean-atmosphere model, climates are simulated in "Q-flux" mode, which uses a mixed-layer ocean model (also called slab ocean model) and is described in detail in *Hansen et al.* [1984] and *Russell et al.* [1984]. In this mode, the heat transport by the ocean current is held constant, but the ocean temperatures and ice cover are computed based on energy exchange with the atmosphere, ocean heat transport, and the ocean mixed layer heat capacity. No exchange of heat between the mixed layer and the deeper

ocean is assumed. Even though no feedback of climate change on ocean transport and heat exchange to the deeper ocean is allowed to occur, the atmospheric simulation is realistic and the results are a good approximation for modest climate perturbations. Ocean heat fluxes used in the current study are from the work of *Mickley et al.* [2004], which used the same version of the GCM as here. The climate sensitivity for this version of the GISS GCM is 4.2degC for doubled CO_2.

3.3.2 Background Sulfate Aerosol

To study the effect of aerosol mixing state, global sulfate distributions are needed. Because the focus of this study is on black carbon, sulfate concentrations for all climate simulations are held constant at the present-day level. Monthly mean sulfate and associated aerosol water concentrations are calculated using the methodology of *Adams et al.* [2001]. The aerosol system of sulfate-ammonium-nitrate-water is simulated online in the GISS GCM with constant SST. The results of the last three years of simulation (after spin-up of 11 months) are averaged and used for subsequent climate simulations. For optical properties, all sulfate is assumed to be ammonium sulfate, but aerosol water content is determined from the the equilibrium water content of the bulk sulfate-ammonium-nitrate-water aerosol system, which is calculated based on the thermodynamic scheme ISORROPIA of *Nenes et al.* [1998]. Annually averaged, the predicted present-day sulfate and aerosol water global burdens are 2.2 Tg and 7.1 Tg, respectively. These values are slightly different from those of *Adams et al.* [2001] because here an updated gas-phase HNO_3 field from the Harvard-GISS GCM is used [*Mickley et al.*, 1999]. The current HNO_3 burden is lower, leading to lower aerosol nitrate, and therefore lower aerosol water content. Figure 3.1 shows the sulfate and aerosol water column burdens used in this study.

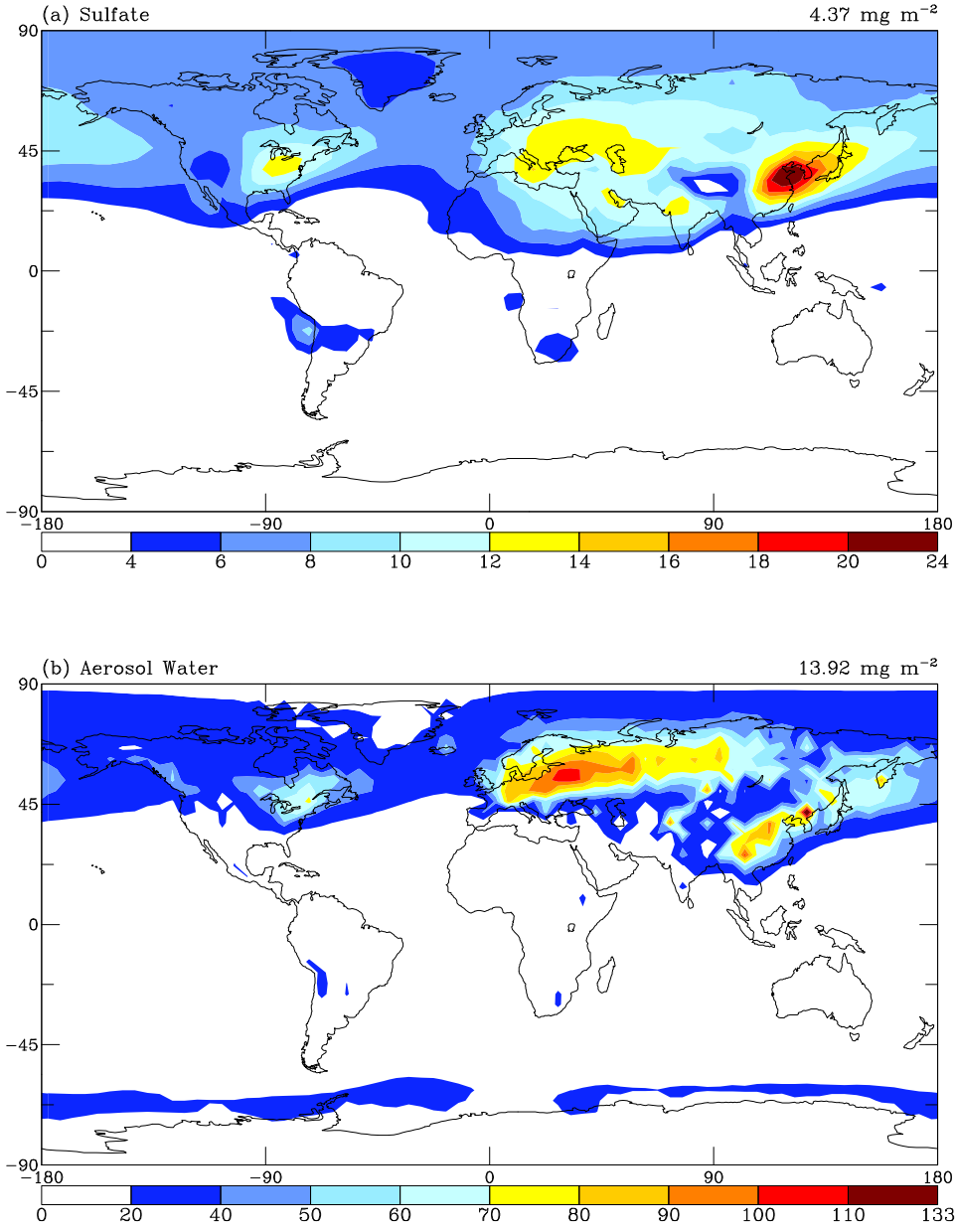

Figure 3.1: Present-day column burdens (mg m^{-2}) of (a) sulfate and (b) aerosol water used in this study. The global mean is provided on the upper right-hand corner of each graph. The burdens are based on the averages of the last 3 years of a 61-month atmosphere-only GCM simulation.

3.3.3 Simulation of Black Carbon

Simulation of BC follows the methodology of *Chung and Seinfeld* [2002]. For the purpose of wet scavenging, BC is divided into hydrophobic and hydrophilic categories. Based on the estimates of *Cooke et al.* [1999], emitted BC is assumed to be 80% hydrophobic and 20% hydrophilic. Once emitted, ambient conversion of hydrophobic BC to hydrophilic BC occurs with an exponential decay lifetime of 1.15 days. Hydrophilic BC is assumed to be infinitely soluble in water whereas hydrophobic BC is assumed to be insoluble. Inside clouds, transport of dissolved hydrophilic BC follows the GCM treatment of liquid water [*Del Genio and Yao*, 1993; *Del Genio et al.*, 1996]. BC is either deposited (in case of precipitation) or returned to the air (in case of evaporation or detrainment). Below clouds, BC is scavenged according to a first-order parameterization that depends on the amount of precipitation [*Dana and Hales*, 1976; *Koch et al.*, 1999]. BC is also removed from the atmosphere by dry deposition with assumed dry deposition velocity of 0.1 cm s^{-1} [*Liousse et al.*, 1996].

A major difference between the this study and that of *Chung and Seinfeld* [2002] in the simulation of BC is that the new emission inventory by *Bond et al.* [2004] is used here. In addition to considering fuel and economic sector as done in the earlier inventory by *Penner et al.* [1993], *Bond et al.* [2004] also take into account combustion type and emission controls. The current inventory is also an update in that it is based on fuel-usage data of 1996 instead of 1984. Estimated global BC emission rates are 1.6, 3.3, and 3.0 Tg yr^{-1} for biofuel, open burning, and fossil fuel, respectively. *Bond et al.* [2004] provide only annual emissions; the biomass burning inventory is distributed monthly by scaling the annual emissions by monthly fire counts of the Global Burned Area 2000 Project [*Grégoire et al.*, 2003]. Fossil fuel and biofuel emissions are assumed to be constant throughout the year.

To estimate the monthly mean preindustrial concentrations of BC, the preindustrial

biomass-burning emission level is assumed to be 10% of present-day and preindustrial fossil fuel emission is assumed to be zero. Preindustrial concentrations are simulated online in the GCM with constant SST. Results of the last three years of simulation after 11 months of spin up period are averaged and imported into the radiation code to calculate the baseline climate (simulation CONTROL). The estimated preindustrial global burden of BC is 0.01 Tg.

The present-day BC concentrations are also simulated online in the simulation CONTROL. The predicted annual mean column burden of BC is shown in Figure 3.2. The predicted present-day BC burden is greatest in eastern US, Europe, India, and China, where fossil fuel emissions are dominant, and in South America and southern Africa, where biomass emissions are high. The predicted present-day global BC burden is 0.14 Tg, which is lower than that of 0.22 Tg of *Chung and Seinfeld* [2002]; the explanation is the lower emission rates of the *Bond et al.* [2004] inventory versus that of *Penner et al.* [1993] inventory that was employed by *Chung and Seinfeld* [2002] (8 Tg yr^{-1} versus 12 Tg yr^{-1} globally). The largest differences occur in eastern Europe and northwestern US, where the emission rate recommended by *Bond et al.* [2004] is about a factor of 5 lower and a factor of 3 higher than those of the previous emission inventory used, respectively.

Predicted zonal mean BC concentrations as a function of pressure are shown in Figure 3.3. Except for the polar regions, predicted BC concentrations are the greatest at the surface and decrease as altitude increases, mostly due to removal by wet deposition. Elevated concentrations in the tropics reflect the significance of biomass burning. Transport from the midlatitudes to high latitudes leads to relatively high levels of BC above the surface in the polar regions.

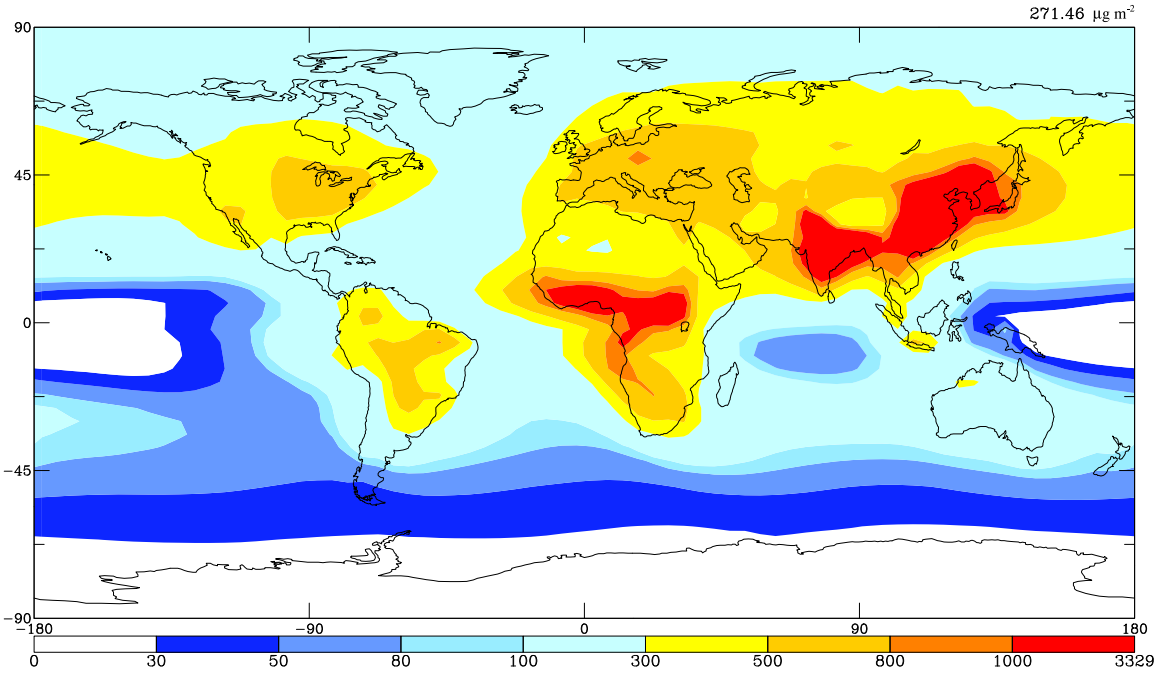

Figure 3.2: Estimated present-day BC column burden (μg m^{-2}). Results are averages of the last 75 years of simulation CONTROL.

3.3.4 Direct Radiative Forcing of Black Carbon

Direct radiative forcing calculations of BC follows the method of *Chung and Seinfeld* [2002]. Optical properties (extinction efficiency, single-scattering albedo, and asymmetry parameter) of BC and sulfate aerosols are determined by Mie theory based on wavelength-dependent refractive indices and assumed size distributions. The particle size distribution is assumed to be the standard gamma distribution with area-weighted effective variance $v_e = 0.2$. The variance is assumed to be constant even when particles take up water and grow to larger sizes. For external mixture of BC and sulfate, the area-weighted effective radii for dry BC and sulfate are 0.1 μm and 0.3 μm [*Tegen et al.*, 2000] and particle densities are assumed to be 1.8 and 1.0 g cm^{-3} [*d'Almeida et al.*, 1991], respectively. Dry sulfate aerosol is represented as ammonium sulfate, with refractive indices from *Toon et al.* [1976]. The water uptake of ammonium sulfate aerosol is governed by thermodynamic equilibrium

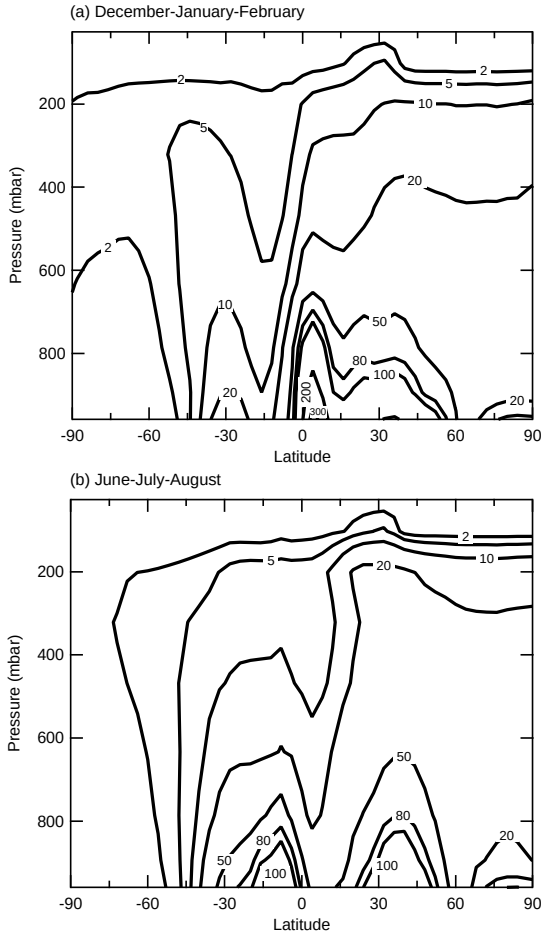

Figure 3.3: Estimated present-day zonal mean BC concentrations (ng m^{-3}) as a function of pressure for (a) December-January-February and (b) June-July-August. Results are averages of the last 75 years of simulation CONTROL.

(see *Adams et al.* [1999] and Section 3.3.2). Composite refractive indices of the aqueous sulfate aerosol are the volume-averaged refractive indices of ammonium sulfate and water. Refractive indices of water are taken from *d'Almeida et al.* [1991]. For BC refractive indices of soot in *d'Almeida et al.* [1991] are used. BC is assumed to not take up water. For an internal mixture of BC and sulfate aerosols, the area-weighted effective radius for the dry particle is assume to be 0.3 μm and particle density is the mass-averaged density of BC, $(NH_4)_2SO_4$, and water. The refractive indices are calculated by volume-weighting the refractive indices of BC and $(NH_4)_2SO_4$, and water.

Using the online concentrations of BC discussed in the previous section, direct radiative forcing of BC is calculated in simulation CONTROL. Direct radiative forcing is calculated at each model layer as the instantaneous difference in the solar radiative irradiance in the presence and absence of BC. At the surface, radiative forcing is calculated as the instantaneous difference in the absorbed solar radiation at the surface in the presence and absence of BC. During CONTROL simulation the radiation scheme is called three times during every radiation time step (5 hours). In the first two calls, imported present-day concentrations of aqueous sulfate aerosols and online concentrations of BC are used. In the first call, sulfate and BC are assumed to be externally mixed. For the second call, sulfate and BC are assumed to be internally mixed. The radiative fluxes during the first two calls are archived for diagnostics and do not affect the climate simulation. Finally, during the third call, the radiation scheme use the imported present-day sulfate and preindustrial BC concentrations. The difference in shortwave radiative fluxes between the first and third call is the direct radiative forcing of BC in an external mixture. Similarly, the difference in shortwave radiative fluxes between the second and third call is the direct radiative forcing of BC in an internal mixture. Note that present-day sulfate concentrations remain constant for all

Table 3.1: Summary of Direct Radiative Forcing Estimates of Anthropogenic BC (W m^{-2})

	External			Internal		
	NH	SH	Global	NH	SH	Global
TOA	0.52	0.15	0.33	0.93	0.28	0.60
Atmosphere	1.33	0.43	0.89	1.92	0.62	1.27
Surface	-0.81	-0.28	-0.55	-1.00	-0.34	-0.67

calls to the radiation scheme. The sulfate contribution to radiative forcing is assumed to stay constant whether sulfate and BC are externally or internally mixed; thus, the change in radiative irradiance between the externally- and internally-mixed cases is attributed to the enhancement of BC direct radiative forcing due to the change in mixing state. Direct longwave radiative forcing is neglected as it is expected to be small [*Haywood et al.*, 1997] (but the longwave climate response to BC shortwave direct radiative forcing is included). A summary of forcing estimates is given in Table 3.1.

3.3.4.1 Annual mean direct radiative forcing

Anthropogenic BC is estimated to contribute to a globally and annually averaged direct radiative forcing of +0.33 W m^{-2} at TOA if considered to be externally mixed. The forcing efficiency of 2.4 W m^{-2} per Tg BC is similar to that of *Chung and Seinfeld* [2002] and *Koch* [2001], which also uses GISS GCM-II'. For comparison of forcing estimates with other models, see *Chung and Seinfeld* [2002]. If BC is assumed to be internally mixed with the present-day level of sulfate, the estimate increases to +0.60 W m^{-2}. The increase in warming is a result of the fact that the single scattering albedo of the assemblage of BC plus sulfate aerosol is lower under the internally mixed assumption. At the surface, anthropogenic BC direct radiative forcing is estimated to be -0.55 W m^{-2} and -0.67 W m^{-2} for the externally- and internally-mixed cases, respectively. The increase in surface cooling going from an external to an internal mixture of BC and sulfate is less than the

corresponding increase in warming at TOA because the magnitude of the ratio of surface to TOA direct radiative forcing decreases with decreasing single scattering albedo (if surface and TOA forcing are of the opposite signs). Globally and annually averaged, the ratio of surface to TOA anthropogenic BC forcing decreases from 1.7 to 1.1 going from an external to an internal mixture of BC and sulfate. Subtracting surface forcing from TOA forcing, anthropogenic BC is predicted to warm the atmosphere by 0.89 W m^{-2} to 1.27 W m^{-2}.

Figure 3.4 shows the geographical distribution of the estimated anthropogenic BC contribution to annual mean direct radiative forcing; the corresponding zonal and monthly mean is shown in Figure 3.5. The geographical distribution of direct radiative forcing at TOA is determined by two factors: the column burden of BC and the reflectivity of the surface underneath the BC layer. These two factors cause TOA forcing to be the largest in eastern China, where the annually averaged forcing is estimated to be 5-6 W m^{-2}. Not only is the BC loading high in eastern China (see Figure 3.2), the underlying desert surface is highly reflective. In contrast to the midlatitudes, BC loading in the northern high latitudes is relatively small; however, due to the high surface albedo from snow and ice, direct radiative forcing in the northern high latitudes is still high. As seen from Figures 3.4a and 3.4b, TOA forcing increases everywhere if BC is assumed to be internally mixed with sulfate, as most areas of high BC loading overlap with areas of high aerosol sulfate loading. In contrast to forcing at TOA, the forcing at the surface is concentrated in the midlatitudes where BC loading is the greatest (Figures 3.4c and 3.4d). Because surface forcing decreases as surface albedo increases, surface forcing in the northern high latitudes is actually very low even though the TOA forcing is high. As mentioned earlier, the increase in surface cooling from the internal to external mixture assumption is less than the increase in warming at TOA. Overall, both TOA and surface direct radiative forcings are concentrated in the NH.

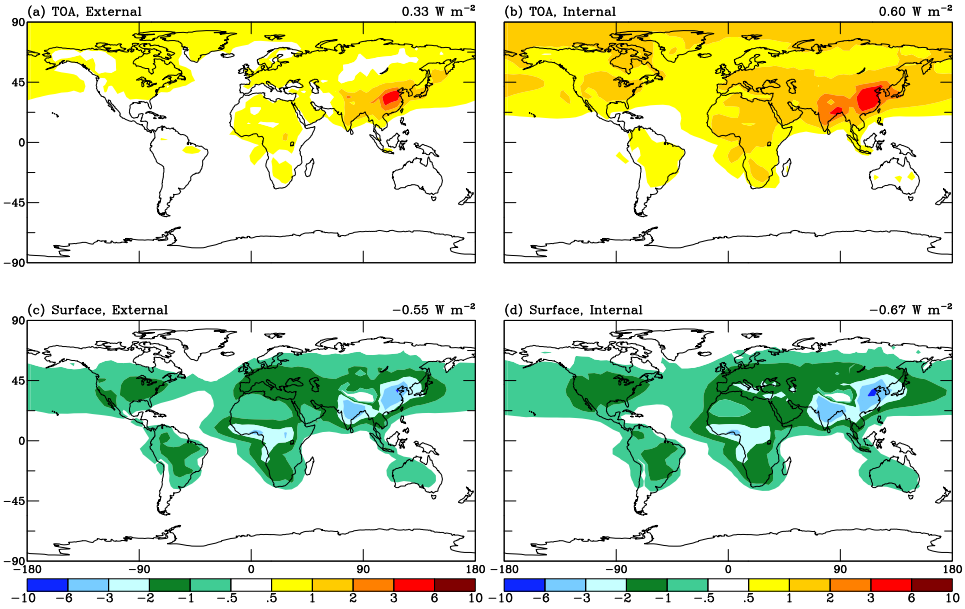

Figure 3.4: Geographical distributions of estimated anthropogenic contribution to annual mean direct radiative forcing (W m^{-2}) of BC at TOA (top panel) and the surface (bottom panel) for externally-mixed (left panel) and internally-mixed (right panel) BC. Results are averages of the last 75 years of simulation CONTROL.

3.3.4.2 Seasonal and zonal mean direct radiative forcing

The zonal and monthly means of estimated BC direct radiative forcings at TOA and the surface are shown in Figure 3.5. Between 30degN and 90degN, TOA and surface forcings peak from April to June, which is the period of maximum BC emission in the NH from biomass burning. During this period of high BC emission in the NH, TOA forcing is the largest in the northern polar region because both surface albedo and solar insolation are high. Surface forcing, on the other hand, peaks at 35degN, where zonal mean emissions are largest. During the northern winter months, direct radiative forcing remains high at midlatitudes because of fossil fuel emissions. In comparison to the NH, peak forcing in the SH is an order of magnitude lower at TOA and a factor of two lower at the surface. The seasonal pattern of forcing in the SH also follows the seasonal cycle of biomass emission, which is largest from August to October in the SH. Zonally, maximum forcing occurs around

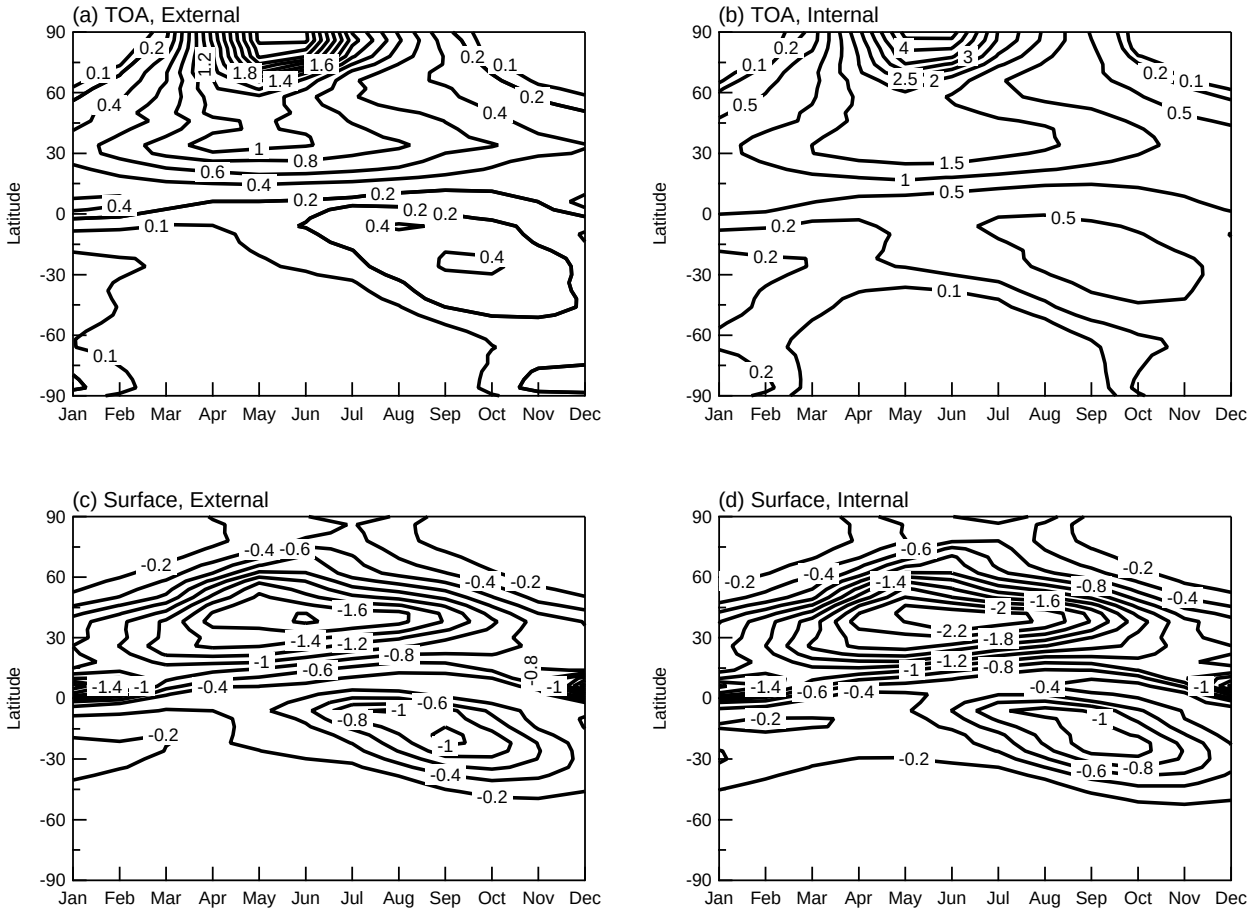

Figure 3.5: Estimated zonal and monthly mean anthropogenic contribution to direct radiative forcing (W m^{-2}) of BC at TOA (top panel) and the surface (bottom panel) for externally-mixed (left panel) and internally-mixed (right panel) BC. Results are averages of the last 75 years of simulation CONTROL.

20degS, overlapping with the region of highest emissions. With essentially no emissions south of 40degS, BC concentrations are so low that direct radiative forcing is extremely low in the southern polar regions. When BC is assumed to be internally mixed with the present-day level of sulfate, the seasonal and zonal patterns of anthropogenic BC radiative forcing remain the same; only the magnitude of the forcing is higher.

Figure 3.6 shows the predicted zonal mean BC direct radiative forcing as a function of pressure for both externally- and internally-mixed BC. The contrast between the north-

ern winter (December-January-February or DJF) and summer (June-July-August or JJA) months is clearly evident. During the northern winter, direct radiative forcing is concentrated near the tropics, where BC concentrations are high. Unlike the distribution of BC concentration, however, forcing is not largest near the surface, but around 800 mbar. The reason for this is that BC above cloud layers results in higher forcing due to the high cloud reflectivity. As mentioned earlier, the largest forcing occurs during the NH summer months at northern high latitudes. Figure 3.6 indicates that maximum forcing in JJA occurs at around 300 mbar (approximately 9 km in elevation). Again, even though BC concentrations here are not very high (about 20 ng m^{-3}), the high reflectivity of the underlying ice and snow surfaces causes direct radiative forcing to be large.

3.4 Results and Discussion

All three climate simulations (CONTROL, EXTERNAL, and INTERNAL) have been carried out for 100 years. The first 25 years are used as spin-up to allow the model sufficient time to reach equilibrium. Results presented in this section are averaged over the last 75 years of each simulation. Assuming that results of each year represent one set of data, statistical analysis based on the two-sample "usual" t-test of *Zwiers and von Storch* [1995] is applied to the results of the last 75 years of each simulation. For latitude-longitude plots, the mean and other statistics are calculated at each grid box without taking into account of spatial correlation. For pressures-zonal plots, statistical analysis are applied after zonal and pressure means have been calculated. Note that the "usual" t-test of *Zwiers and von Storch* [1995] differs from that of the traditional Student's t-test in that the "usual" t-test does not assume that the results of each simulation year to be independent. For this study in which $n = 75$ for using results from the last 75 years of each simulation, if Student's t-test

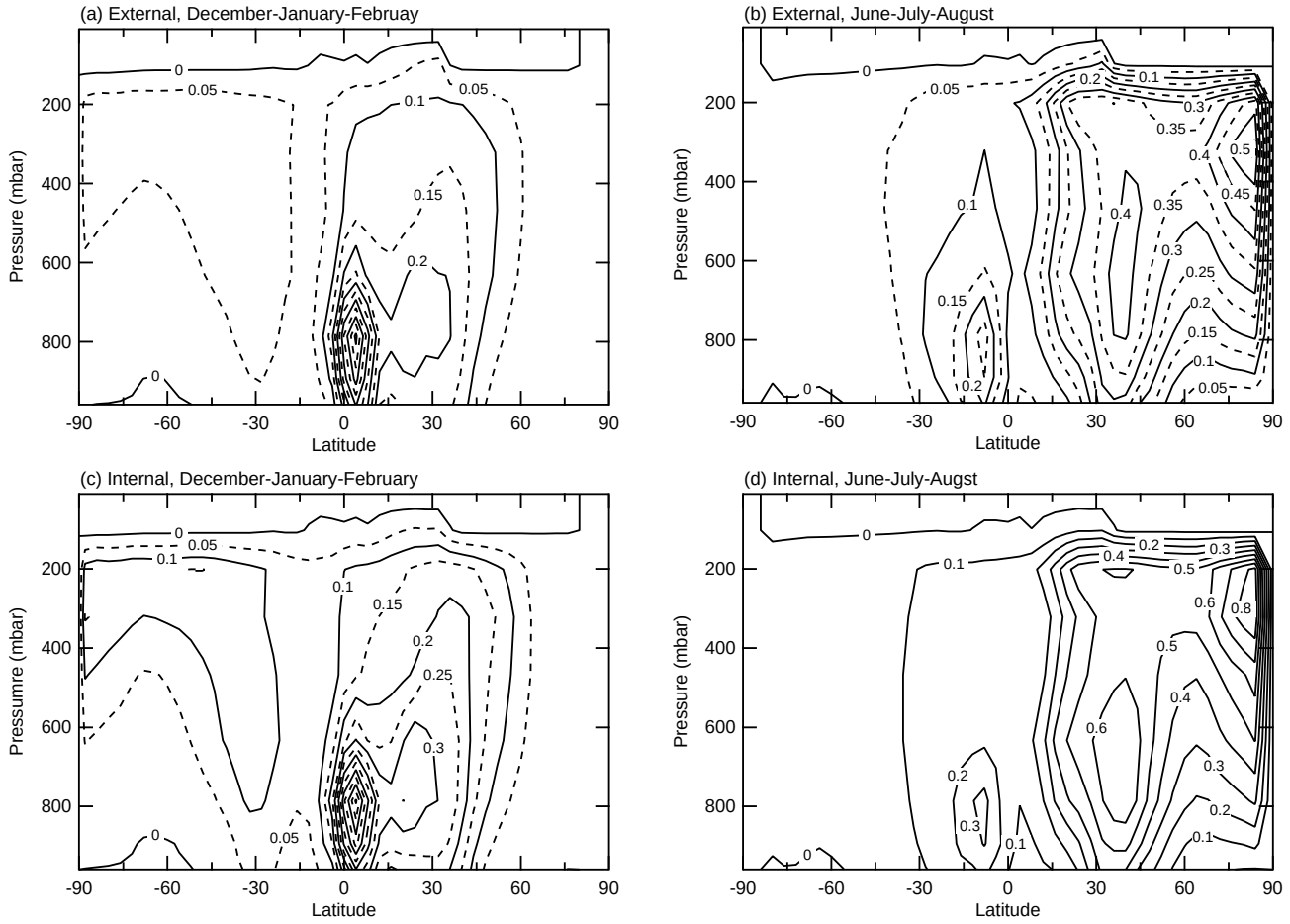

Figure 3.6: Estimated zonal mean anthropogenic contribution to direct radiative forcing (W m^{-2}) of BC as a function of pressure for December-January-February (left panel) and June-July-August (right panel) for externally-mixed (top panel) and internally-mixed (bottom panel) BC. Except for (d), contour lines are in 0.05 W m^{-2} increments. Results are averages of years 26 to 30 of simulation CONTROL.

is applied directly, the difference in means is considered to be significant at 95% confidence level if the difference is greater than $1.98 \times s\sqrt{2/n}$, where s is the standard deviation of the climate variable of interest. However, Student's t-test assumes that the number of samples to be independent. Since in this study the results from the 75 sampled years are from the same simulation, the independence assumption is not valid. In the "usual" t-test, the difference in means is significant at the 95% confidence interval if it is greater than $1.98 \times s\sqrt{1/\hat{n}_e + 1/\hat{m}_e}$, where $\hat{n}_e < n$ and $\hat{m}_e < n$ are the equivalent sample sizes for the two simulations to be compared. In the case that $\hat{n}_e + \hat{m}_e < 30$, a lookup table is utilized. For details on how to calculate equivalent sample size and more rigorous explanation of the "usual" t-test, please refer to *Zwiers and von Storch* [1995]. For the three simulations carried out in this study, $\hat{n}_e$ and $\hat{m}_e$ are on the order of 30, but vary depending on the climate variable and location of interest.

Unless otherwise specified, all results shown are significant at the 95% level. Also note that the statistical analysis is applied only to the variability of the model output; uncertainties of model parameterization, emission rates, subgrid variabilities, etc. are not considered. Figure 3.7 shows the surface air temperature for all three 100-year simulations. The figure indicates that each simulation has equilibrated at a different climate state. A summary of estimated annual mean change of selected climate variables is given in Table 3.2.

3.4.1 Annual Mean Surface Air Temperature Response

The geographical distribution of the equilibrium annual mean surface air temperature response attributed to direct radiative forcing of anthropogenic BC is shown in Figure 3.8. Even though the forcing resulting from BC at the surface is negative, BC forcing is positive in the air immediately above the surface, and the surface air temperature is predicted to

Table 3.2: Summary of Annual Mean Differences and 95% Confidence Intervals of Selected Climate Variables.

	EXTERNAL-CONTROL			INTERNAL-CONTROL			INTERNAL-EXTERNAL		
	NH	SH	Global	NH	SH	Global	NH	SH	Global
Surface Air Temperature (K)	0.29±0.05	0.11±0.03	0.20±0.03	0.54±0.04	0.20±0.03	0.37±0.03	0.25±0.04	0.10±0.03	0.17±0.03
Land Temperature (K)	0.31±0.06	0.14±0.05	0.26±0.04	0.59±0.05	0.30±0.05	0.50±0.04	0.28±0.05	0.16±0.06	0.24±0.03
Sea Surface Temperature (K)	0.19±0.15	0.07±0.22	0.12±0.28	0.36±0.12	0.13±0.12	0.23±0.12	0.17±0.15	0.06±0.17	0.11±0.23
Precipitation (mm day^{-1})	0.030±0.010	-0.023±0.010	0.003±0.003	0.057±0.009	-0.035±0.009	0.011±0.003	0.027±0.009	-0.012±0.009	0.008±0.003
Total Cloud Cover (%)	0.28±0.16	-0.14±0.09	0.07±0.08	0.44±0.15	-0.22±0.09	0.11±0.08	0.16±0.13	-0.08±0.09	0.04±0.07
Cloud Top Pressure (mbar)	-0.7±0.8	2.1±0.7	0.7±0.4	-2.0±0.8	2.7±0.6	0.3±0.4	-1.3±0.7	0.6±0.7	-0.4±0.4
Precipitable Water (mm)	0.56±0.08	0.20±0.07	0.38±0.07	1.03±0.07	0.38±0.07	0.70±0.06	0.47±0.08	0.18±0.08	0.32±0.08
Surface Albedo (%)	-0.15±0.05	-0.00±0.01	-0.08±0.03	-0.29±0.05	-0.01±0.01	-0.15±0.03	-0.14±0.05	-0.01±0.01	-0.07±0.03

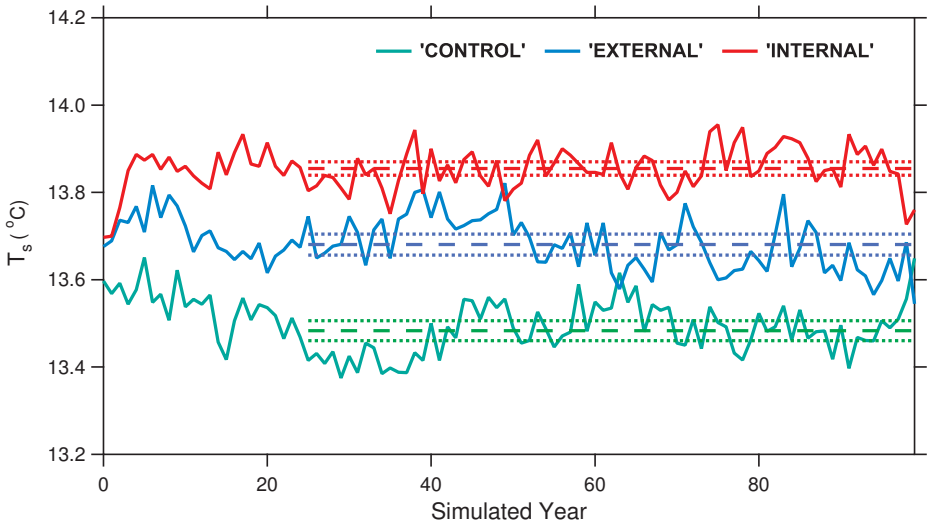

Figure 3.7: Modeled global and annual mean surface air temperature versus simulation year. The dashed lines are means of the last 75 years of simulation; the dotted lines indicate 95% confidence intervals of the means.

increase. Globally and annually averaged, the surface air temperature is predicted to rise by 0.20 and 0.37 K for the externally- and internally-mixed cases, respectively. Clearly, uncertainty in direct radiative forcing due to the mixing state leads to significant difference in the temperature response.

In both the externally- and internally-mixed cases, the temperature response is concentrated more in the NH, which is expected since radiative forcing is strongest in the NH. The estimated surface temperature increase is 0.29 to 0.54 K for the NH and 0.11 to 0.20 K for the SH. Other than the hemispheric pattern, however, the geographical pattern of the surface temperature response does not follow that of the direct radiative forcing and the maximum response does not occur over regions of largest forcing. Previous studies have shown that temperature response to radiative forcing is largest in the high latitudes independent of the type of forcing (i.e., solar, CO_2, ozone, or cloud forcing), e.g., *Manabe and Wetherald* [1975], *Chen and Ramaswamy* [1996a], *Hansen et al.* [1997], *Forster et al.* [2000], *Boer and Yu* [2003], *Joshi et al.* [2003], and *Mickley et al.* [2004]. The predictions here for

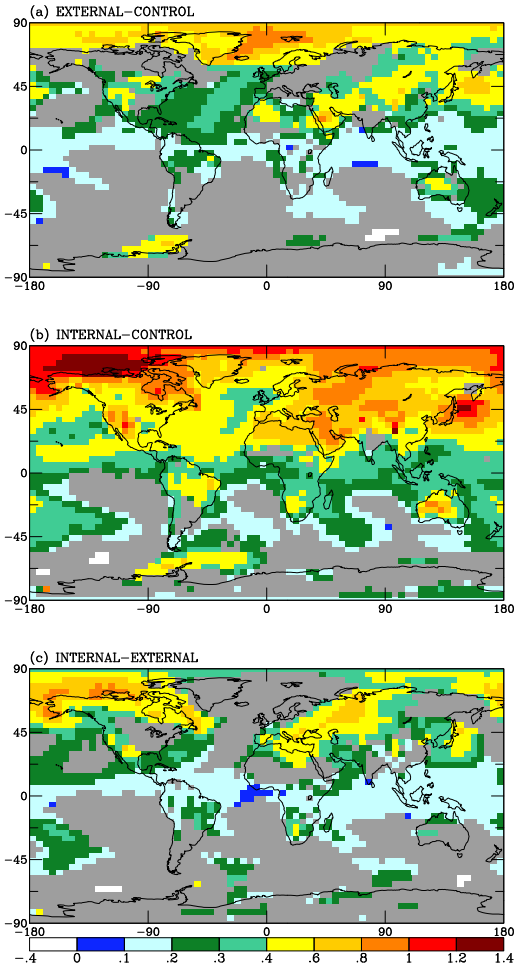

Figure 3.8: Estimated change in equilibrium annual mean surface air temperature (K) for (a) EXTERNAL minus CONTROL, (b) INTERNAL minus CONTROL, and (c) INTERNAL minus EXTERNAL. Gray indicates areas where the change is not significant at the 95% confidence level.

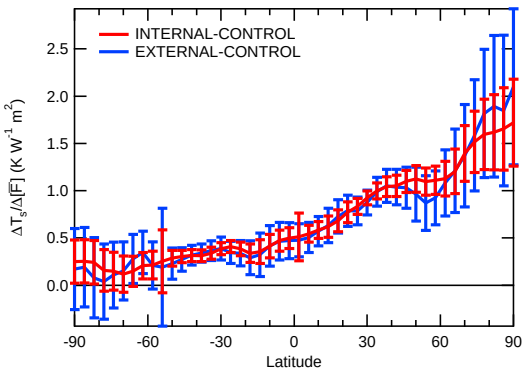

Figure 3.9: Estimated change in zonal and annual mean surface air temperature normalized by global and annual mean instantaneous direct radiative forcing at TOA. The error bars indicate 95% confidence intervals assuming zero uncertainty for the direct radiative forcing estimates.

BC direct radiative forcing exhibit a similar pattern, with the temperature response in high northern latitudes being as large as 1.4 K in annual mean. Figure 3.9 shows the zonal mean change in annual mean temperature weighted by the globally and annually averaged forcing at TOA. Figure 3.9 indicates that the zonal mean surface temperature response is very similar for externally- and internally-mixed BC and that the response is clearly maximum in the northern high latitudes. Note that zonally and annually averaged, the largest forcing occurs at around 30degN and in the northern polar region and is about 0.8 W m^{-2} and 1.4 W m^{-2} for externally- and internally-mixed BC, respectively.

Other than the northern high latitudes, when BC is externally mixed, substantial urface warming is predicted over most of Asia, as well as remote regions of the Atlantic and the Pacific, even extending to parts of the SH. The temperature response over the high BC emission regions of Europe and North America is actually insignificant in comparison to the model variability. If BC is assumed to be internally mixed with sulfate, however, then substantial surface warming is predicted to occur throughout the entire NH as well as a significant portion of the SH, including parts of South America and most of southern Africa,

Australia, and southern Pacific. Notice that even though the absolute temperature increase in the tropics is relatively small in comparison to that of the high northern latitudes, relative to the natural variability (as measured by the standard deviation of model output) of the respective latitude, the temperature increase in the tropics is much higher. Figure 3.10 shows the estimated ratio of the change to the standard deviation of annual mean surface air temperature. Over the tropics, the predicted change in surface air temperature is on the order of one standard deviation for externally-mixed BC. For internally-mixed BC, the temperature increase is on the order of three standard deviations. As *Menon et al.* [2002] and *Roberts and Jones* [2004] have already suggested, Figures 3.8 and 3.10 strongly indicate that the effect of BC radiative forcing is not local, but in fact can alter the climate of remote regions.

Even though the climate sensitivity of BC predicted here is similar to the prediction of *Roberts and Jones* [2004] (see Section 3.4.2), the results here differ in one significant way: *Roberts and Jones* [2004] predict small cooling of surface air in some regions, such as in China and India, whereas in this study no significant surface cooling is predicted anywhere. As mentioned previously, absorption of BC in the atmosphere reduces incident solar radiation at the surface, potentially leading to cooling at the surface. If results from years 20 to 30 of each simulation of this study were analyzed (to parallel *Roberts and Jones* [2004] study), surface cooling would have been predicted in some regions, but the cooling is statistically insignificant. Thereafter the climate equilibrates and the reduction in solar radiation at the surface is compensated by the changes in longwave radiative flux, sensible heat flux, and latent heat flux (see Section 3.4.6 later); eventually warming or no change is predicted everywhere at the surface. Lacking statistical information, and given the relatively short simulations of *Roberts and Jones* [2004], detailed comparison between this study and

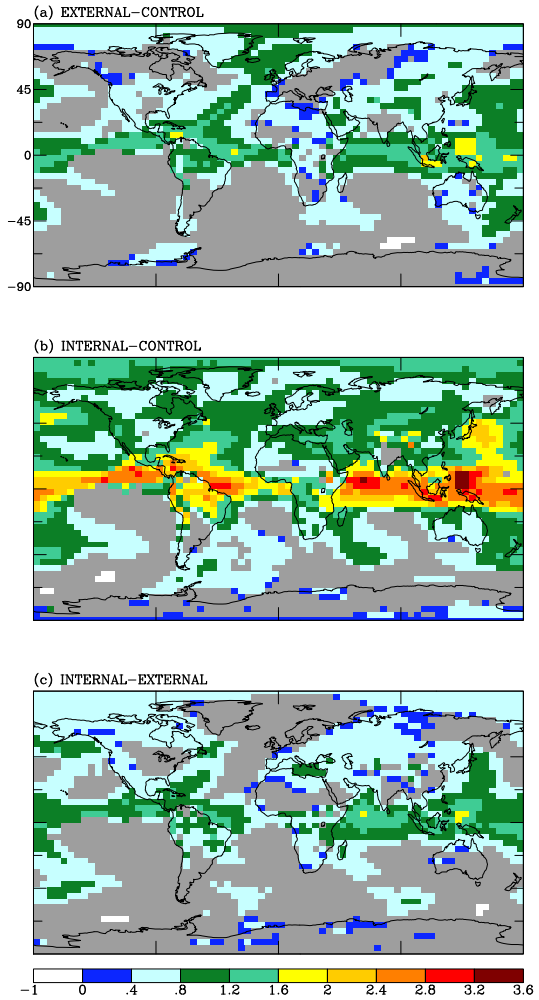

Figure 3.10: Grid by grid estimated ratio of equilibrium change to standard deviation of annual mean surface air temperature for (a) EXTERNAL minus CONTROL, (b) INTERNAL minus CONTROL, and (c) INTERNAL minus EXTERNAL. Gray indicates areas where the change is not significant at the 95% confidence level.

Roberts and Jones [2004] is difficult.

In comparison to the surface air temperature response induced by ozone and equivalent CO_2 forcings studied by *Mickley et al.* [2004], there are both similarities and differences. Direct comparison of this study and *Mickley et al.* [2004] is particularly useful because both studies use the same climate model. *Mickley et al.* [2004] examine the climate response of direct radiative forcing of anthropogenic ozone and a 25-ppm increase in CO_2 concentration from the present-day level. In both cases, the annually and globally averaged instantaneous radiative forcing at the tropopause is estimated to be 0.49 W m^{-2}, which lies between that of 0.33 and 0.60 W m^{-2} for BC estimated here. Note that *Mickley et al.* [2004] report only the instantaneous forcing at the tropopause. As mentioned in Section 3.2, adjusted forcing is a better of measure of potential climate response than instantaneous forcing. Unlike BC, for which instantaneous forcing at TOA, instantaneous forcing at tropopause, and adjusted forcing at tropopause are all approximately equal, adjusted forcings at the tropopause are typically 10-20% less than the instantaneous forcings at the tropopause for CO_2 and ozone [*Hansen et al.*, 1997; *Mickley et al.*, 2004]. The estimated climate sensitivity of 0.6 K W^{-1} m^{-2} for BC calculated here is within 15% of the climate sensitivity of ozone and about 30% less than that of CO_2, as calculated by *Mickley et al.* [2004] but taking into the account of the 10-20% reduction for the forcings of ozone and CO_2. The difference in climate sensitivities of BC and ozone is within the uncertainties of the model, despite the fact that the geographical and seasonal patterns of ozone radiative forcing are different from those of BC. The 30% reduction in the climate sensitivity of BC compared to that of CO_2 is similar to the 40% reduction found by *Roberts and Jones* [2004]. The reason for the lowered climate sensitivity of BC in comparison to that CO_2 is not known.

In all three cases, the maximum temperature increase is still in the northern high lat-

itudes, indicating that, to some extent, regional differences in forcing are diluted in the temperature response. However, regional differences do exist. For example, annual mean surface air temperature is estimated to increase by about 0.6 to 0.8 K in central and eastern Russia, where no significant increase is predicted for ozone or CO_2 forcing. The reason for the difference is likely because radiative forcing over China is larger for BC than for CO_2 and ozone (estimated annual mean direct radiative forcings over China are approximately 5 W m^{-2}, 0.5 W m^{-2}, and 0.1 W m^{-2} for anthropogenic BC, anthropogenic ozone, and 25-ppm increase in CO_2, respectively). Similarly for western Europe, significant warming is predicted only for BC, though only if BC were internally-mixed with sulfate. Here, predicted forcing for BC mixed internally with sulfate is slightly higher than that of O_3 and CO_2. The warming in eastern China and western Europe may also be caused by non-local radiative forcing. For example, *Menon et al.* [2002] predict BC in Asia causes warming over most of Europe even with fixed SST.

3.4.2 Climate Sensitivity of Black Carbon

For both externally- and internally-mixed BC the climate sensitivity of direct radiative forcing of anthropogenic BC predicted here is ∼0.6 K W^{-1} m^2, which is very similar to that predicted by *Roberts and Jones* [2004] for quadrupled fossil fuel BC (0.56 K W^{-1} m^2 with 95% confidence interval of ±0.06). Note that the climate sensitivity for double CO_2 of the Hadley Centre climate model used in *Roberts and Jones* [2004] is 0.9 K W^{-1} m^2, comparable to 0.8 K W^{-1} m^2 for the climate model used in this study. The fact that climate sensitivity is independent of the mixing assumption suggests that the linear relationship of Equation (3.1) is still valid for BC, contrary to the conclusion of *Hansen et al.* [1997] and *Cook and Highwood* [2004]. The difference can be explained by the fact that the climate

sensitivities reported in *Hansen et al.* [1997] and *Cook and Highwood* [2004] are for a mixture of purely scattering aerosol with small amount of absorbing material. Relevant results from *Hansen et al.* [1997] and *Cook and Highwood* [2004] are reproduced in Table 3.3. Based on the λ calculated for aerosols with single scattering albedo ω between 0.8 and 1.0 and at fixed optical depth, both studies conclude that the proportionality between $\Delta[\bar{T}_s]$ and $\Delta[\bar{F}]$ is not constant (see column 4 of Table 3.3). The climate sensitivity factor λ calculated by *Hansen et al.* [1997] and *Cook and Highwood* [2004], however, is not only for absorbing aerosols. The climate sensitivity of absorbing aerosols can be inferred from the results of *Hansen et al.* [1997] and *Cook and Highwood* [2004] by the following method.

Assuming that the linear relationship of Equation (3.1) holds for purely scattering aerosols, then the contribution of surface air temperature change from a purely scattering aerosol is given by

$$[\Delta\bar{T}_{\mathrm{s,sca}}] = \lambda_{\mathrm{sca}}\Delta[\bar{F}_{\mathrm{sca}}] \tag{3.2}$$

In the case studied by *Hansen et al.* [1997], for example, $\lambda_{\mathrm{sca}} = 0.87$ K W^{-1} m^2 (fifth row and fourth column of Table 3.3). *Hansen et al.* [1997] and *Cook and Highwood* [2004] study the effect of absorbing aerosols by reducing the single scattering albedo ω but keeping the optical depth τ_{total} constant. Physically, a small portion of the purely scattering aerosol is replaced with an absorbing aerosol such that (under the external mixture assumption)

$$\omega\tau_{\mathrm{total}} = \tau_{\mathrm{sca}} + \omega_{\mathrm{abs}}\tau_{\mathrm{abs}} \tag{3.3}$$

$$\tau_{\mathrm{total}} = \tau_{\mathrm{sca}} + \tau_{\mathrm{abs}} \tag{3.4}$$

where again the subscript "sca" refers to the purely scattering aerosol component, "abs" refers to the absorbing aerosol, and ω is the single scattering albedo of the assemble of both

aerosol types. For varying ω and fixed τ_{total}, the two equations above can be solved for the optical depth of the pure scattering aerosol τ_{sca}:

$$\tau_{\text{sca}} = \left(\frac{\omega - \omega_{\text{abs}}}{1 - \omega_{\text{abs}}} \right) \tau_{\text{total}} \tag{3.5}$$

The radiative forcing contribution can also be separated into the purely scattering and absorbing components:

$$\Delta[\bar{F}] = \frac{\tau_{\text{sca}}}{\tau_{\text{total}}} \Delta[\bar{F}_{\text{sca},\tau=\tau_{\text{total}}}] + \Delta[\bar{F}_{\text{abs}}] \tag{3.6}$$

The first term on the right accounts for the reduction in cooling due to the amount of purely scattering aerosol that is displaced by the absorbing aerosol, and the second term $\Delta[\bar{F}_{\text{abs}}]$ accounts for the warming due to the addition of the absorbing aerosol. The equation above can be rearranged to solve for $\Delta[\bar{F}_{\text{abs}}]$:

$$\Delta[\bar{F}_{\text{abs}}] = \Delta[\bar{F}] - \frac{\tau_{\text{sca}}}{\tau_{\text{total}}} \Delta[\bar{F}_{\text{sca},\tau=\tau_{\text{total}}}] \tag{3.7}$$

Combining Equations (3.1), (3.2) and (3.6), the temperature response is

$$\Delta[\bar{T}_{\text{s}}] = \lambda_{\text{sca}} \left(\frac{\tau_{\text{sca}}}{\tau_{\text{total}}} \Delta[\bar{F}_{\text{sca},\tau=\tau_{\text{total}}}] \right) + \lambda_{\text{abs}} \Delta F_{\text{abs}} \tag{3.8}$$

The climate sensitivity factor for absorbing aerosol λ_{abs} can be solved from the above equation:

$$\lambda_{\text{abs}} = \frac{\Delta[\bar{T}_{\text{s}}] - \lambda_{\text{sca}} \left(\frac{\tau_{\text{sca}}}{\tau_{\text{total}}} \Delta[\bar{F}_{\text{sca},\tau=\tau_{\text{total}}}] \right)}{\Delta F_{\text{abs}}} \tag{3.9}$$

The calculated values for λ_{abs} based on the results of *Hansen et al.* [1997] and *Cook*

Table 3.3: Climate Sensitivity of Absorbing Aerosol from Previous Studies.

Reported in literature				Eqns (3.5) to (3.9) using $\omega_{abs} = 0.38$		
ω	$\Delta[F]$ (W m^{-2})	$\Delta[T_s]$ (K)	λ (K W^{-1} m^2)	τ_{sca}	$\Delta[F_{abs}]$ (W m^{-2})	λ_{abs} (K W^{-1} m^2)
Hansen et al. [1997]						
1	-2.43	-2.12	0.87	0.1	0	...
0.95	-1.61	-0.94	0.58	0.092	0.62	1.62
0.90	-0.82	0.17	-0.21	0.084	1.22	1.60
0.85	-0.03	1.01	-33.70	0.076	1.81	1.44
0.80	0.74	1.90	2.57	0.068	2.39	1.40
Cook and Highwood [2004]; Lower troposphere						
1	-4.72	-1.70	0.36	0.2	0	...
0.95	-3.02	-0.60	0.20	0.18	1.32	0.73
0.90	-1.40	0.60	-0.43	0.17	2.56	0.79
0.85	0.14	1.80	12.86	0.15	3.72	0.83
0.80	1.61	2.90	1.80	0.14	4.81	0.84
Cook and Highwood [2004]; Mid troposphere						
1	-4.90	-1.80	0.37	0.2	0	...
0.95	-2.28	-0.90	0.39	0.18	2.22	0.34
0.90	0.23	-0.10	-0.43	0.17	4.34	0.32
0.85	2.64	0.60	0.23	0.15	6.35	0.31
0.80	4.95	1.20	0.24	0.14	8.27	0.29

Note the climate sensitivity for double CO_2 is 0.92 and 0.47 K W^{-1} m^2 for the climate models used in *Hansen et al.* [1997] and *Cook and Highwood* [2004], respectively.

and Highwood [2004] are given in Table 3.3 for $\omega_{abs} = 0.38$, which is the value of the single scattering albedo used for BC in this study. The calculated values for λ_{abs} shown in Table 3.3 indicate that, for a given climate model and within the same globally uniform distribution in optical depth, the climate sensitivities vary by less than 15%. For ω_{abs} in the range of 0 to 0.7, the values of λ_{abs} vary by less than 20%, which is within the model uncertainty.

To summarize, the results of *Hansen et al.* [1997] and *Cook and Highwood* [2004] and the calculated λ_{abs} indicate that the proportionality between global mean surface air temperature change and direct radiative forcing is nearly constant for aerosols with single scattering albedo less than ∼0.7. In other words, linearity is true for direct radiative forcing of BC (of which ω is on the order of 0.4); however, the linear relationship does not hold for the

combined forcing of a mixture of BC plus sulfate (of which the composite ω is on the order of 0.9 depending on the mass ratio of each component). This supports the results of this study that the climate sensitivity of BC itself is independent of the mixing state.

A note of caution must be noted with regard to the value of λ or λ_{abs}. There are two issues concerning the proportionality constant: 1) whether it is the same among species, and 2) whether it varies for the same species under different conditions. With regard to the first issue, as noted in Section 3.4.1, the climate sensitivity of BC is ~30% less than that of CO_2, consistent with the results of *Roberts and Jones* [2004]. With regard to the second issue, the linearity of climate response of BC direct radiative forcing has only been shown for limited cases. In both *Hansen et al.* [1997] and *Cook and Highwood* [2004], optical depth is distributed uniformly throughout the globe. For this study, as direct radiative forcing of BC increases from being externally- to internally-mixed with sulfate, the distribution of the forcing remains mostly the same (with slight change due to the fact that the distribution of sulfate does not overlap completely with that of BC). The results of *Cook and Highwood* [2004] indicate that λ_{abs} is a factor of 2 higher for forcing located in the lower troposphere (695-930 mbar) in comparison to forcing located in the mid-troposphere (310-400 mbar), consistent with the "ghost-forcing" experiment of *Hansen et al.* [1997], in which arbitrary heating is added to the radiative source term in the energy equation. Also, note that in both *Hansen et al.* [1997] and *Cook and Highwood* [2004], for forcing in the lower troposphere, $\lambda_{\text{abs}} \sim 1.7\lambda_{2\times CO_2}$. The result of this study, i.e., $\lambda_{\text{BC}} \sim 0.7\lambda_{2\times CO_2}$, is similar to that of $\lambda_{\text{abs}} \sim 0.7\lambda_{2\times CO_2}$ calculated from the results of *Cook and Highwood* [2004] for forcing in the mid-troposphere. As mentioned previously in Section 3.3.4.2 and indicated by Figure 3.6, maximum BC forcing is predicted to occur in the mid-troposphere. Clearly, the climate sensitivity of direct radiative forcing of BC is different if the vertical distribution of the

forcing is different.

3.4.3 Monthly Mean Surface Air Temperature Response

The monthly and zonally averaged surface air temperature response is shown in Figure 3.11. As *Hansen et al.* [1997] have shown, the equilibrium response of surface air temperature is insensitive to the seasonality of the forcing because the radiative relaxation time of the troposphere is on the order of months and the response time for mixed-layer ocean is on the order of years. Figure 3.11 indicates that the greatest change in surface temperature in the northern high latitudes occurs during winter and early spring. At the northern midlatitudes, the warming is on the order of 0.3 K, with slightly more warming occurring during summer. In the tropics and southern midlatitudes, the surface air temperature is predicted to be less, on the order of 0.1 K, leading to an increase in the meridional temperature gradient between the northern and southern hemispheres. In contrast to the high latitudes, the response in the low and midlatitudes shows little seasonal variability. The surface response in the southern high latitudes is insignificant. In comparison to the externally-mixed case, internal mixing is predicted to extend the period of warming in the high northern latitudes and increase surface warming by around 0.3 K throughout the year in the midlatitudes and the tropics.

Figures 3.8 to 3.11 reinforce previous studies on climate effects of CO_2, ozone, and solar forcings that the surface temperature response is the strongest in the high latitudes (in this case, the northern high latitudes). One reason, in the case of BC, is simply that the TOA radiative forcing is large in this region (see Figures 3.4 and 3.5). Another reason is that a forcing at high latitudes yields a stronger response than a forcing at low latitudes due to the positive feedback mechanism in which surface warming reduces snow and ice coverage,

reducing surface albedo, and thus leading to even greater warming. The change in zonally averaged predicted annual mean surface albedo in the NH is shown in Figure 3.12. Also, at high latitudes during winter, a more stable lapse rate tends to confine the thermal response close the the surface, as with the case of CO_2 suggested by *Manabe and Wetherald* [1975]. The positive albedo feedback mechanism and more stable lapse rate also causes the surface temperatures response to be the largest during winter even though TOA forcing is largest during spring and summer. Note that the reduced surface albedo in this study is the result of melting of ice and snow as BC direct radiative forcing warms the atmosphere and surface. The albedo change due to snow darkening effect studied in *Hansen and Nazarenko* [2004] and *Jacobson* [2004] is not considered here.

3.4.4 Vertical Distribution of Temperature Response

The zonal mean temperature response as a function of pressure for DJF and JJA is shown in Figure 3.13. Warming is predicted to occur throughout most of the troposphere up to 200 mbar and north of 60degS. During JJA, the zonal and altitude pattern of the temperature response is similar to that of the forcing north of 30degN, otherwise the pattern of temperature response does not follow the pattern of forcing. As mentioned previously, high direct radiative forcing and ice-albedo feedback causes the warming to be largest in the northern high latitudes, and the stable lapse rate during northern winter tends to confine the temperature response close to the surface. During JJA, however, the largest temperature response occurs around 300 mbar in the northern polar region as well as around 45degN, close to the regions of the largest forcing at this time of the year. In the low and midlatitudes, the predicted warming is greatest in the the upper troposphere because moist convective processes tend to adjust temperatures in a column toward the moist adiabatic

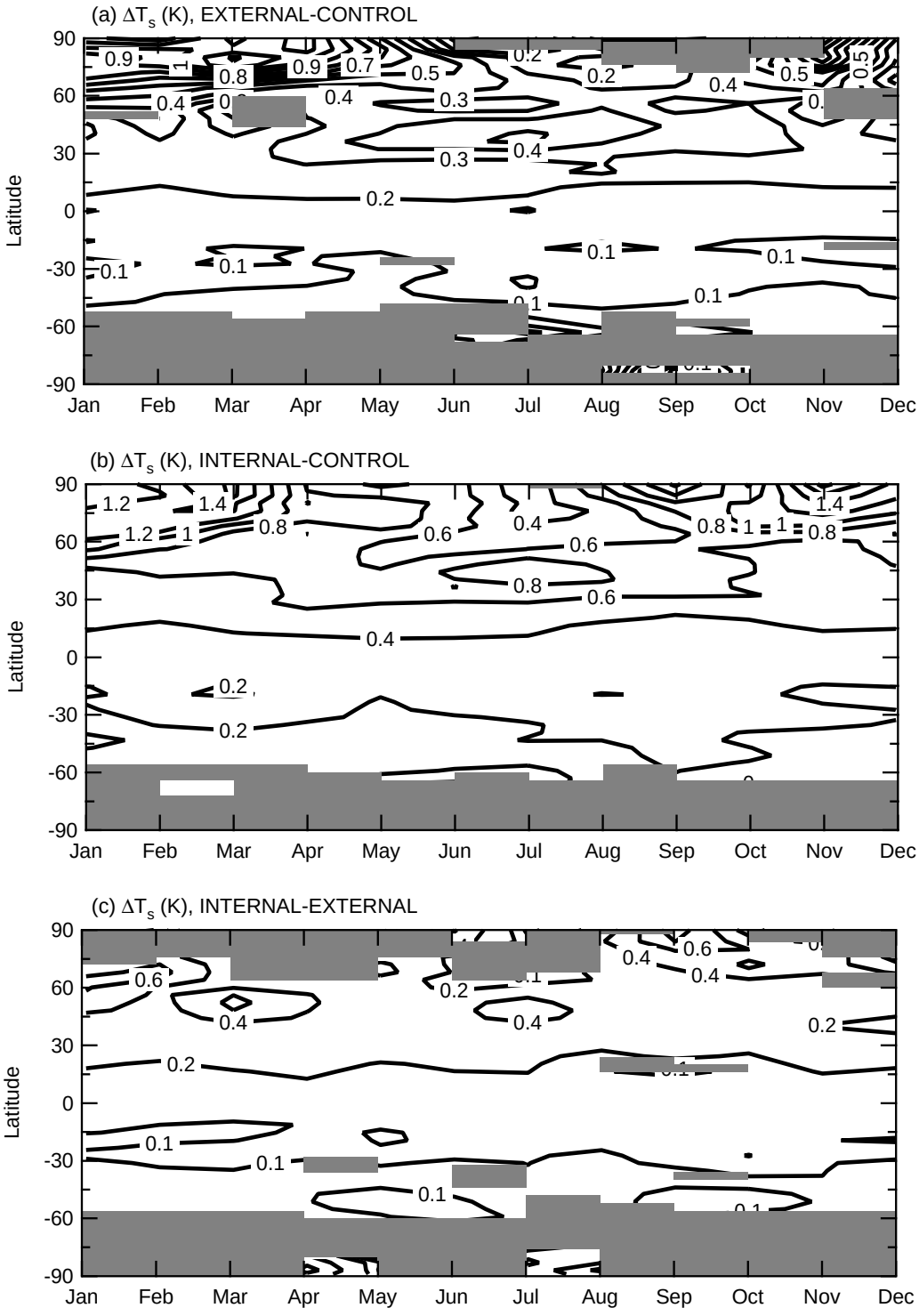

Figure 3.11: Estimated change in monthly and zonally averaged equilibrium surface air temperature (K) for (a) EXTERNAL minus CONTROL, (b) INTERNAL minus CONTROL, and (c) INTERNAL minus EXTERNAL. Gray indicates areas where the change is not significant at the 95% confidence level.

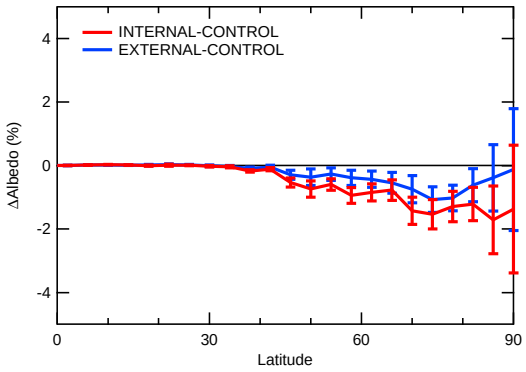

Figure 3.12: Estimated change in annually and zonally averaged surface albedo in the NH. The error bars indicate 95% confidence intervals.

lapse rate, causing the maximum tropospheric warming to occur in the upper troposphere instead of near the surface [*Manabe and Wetherald*, 1975]. Even though forcing in the SH is small, substantial warming still occurs, especially around 60degS. The warming over the SH is partly a result of small radiative forcing but also because of dynamical and diffusion effects from warming in the NH. *Forster et al.* [2000] have shown that even when solar or CO_2 forcing is restricted to the NH (SH), substantial warming is predicted to occur in the SH (NH). Similarly, when *Chen and Ramaswamy* [1996b] perturb the climate by increasing liquid water path or reducing cloud droplet radius from 20deg to 70degN, cooling is predicted in the SH. The results here further support the conclusion that local radiative forcing can cause climate change in remote regions. Overall, the predicted temperature increase of the internally-mixed case is almost twice that of the externally-mixed case.

3.4.5 Response of the Hydrological Cycle

Figure 3.14 shows the predicted zonally averaged change in specific humidity as a function of pressure. Direct radiative forcing of BC causes an increase in water vapor in the atmosphere, consistent with increasing temperature. The water vapor mixing ratio in-

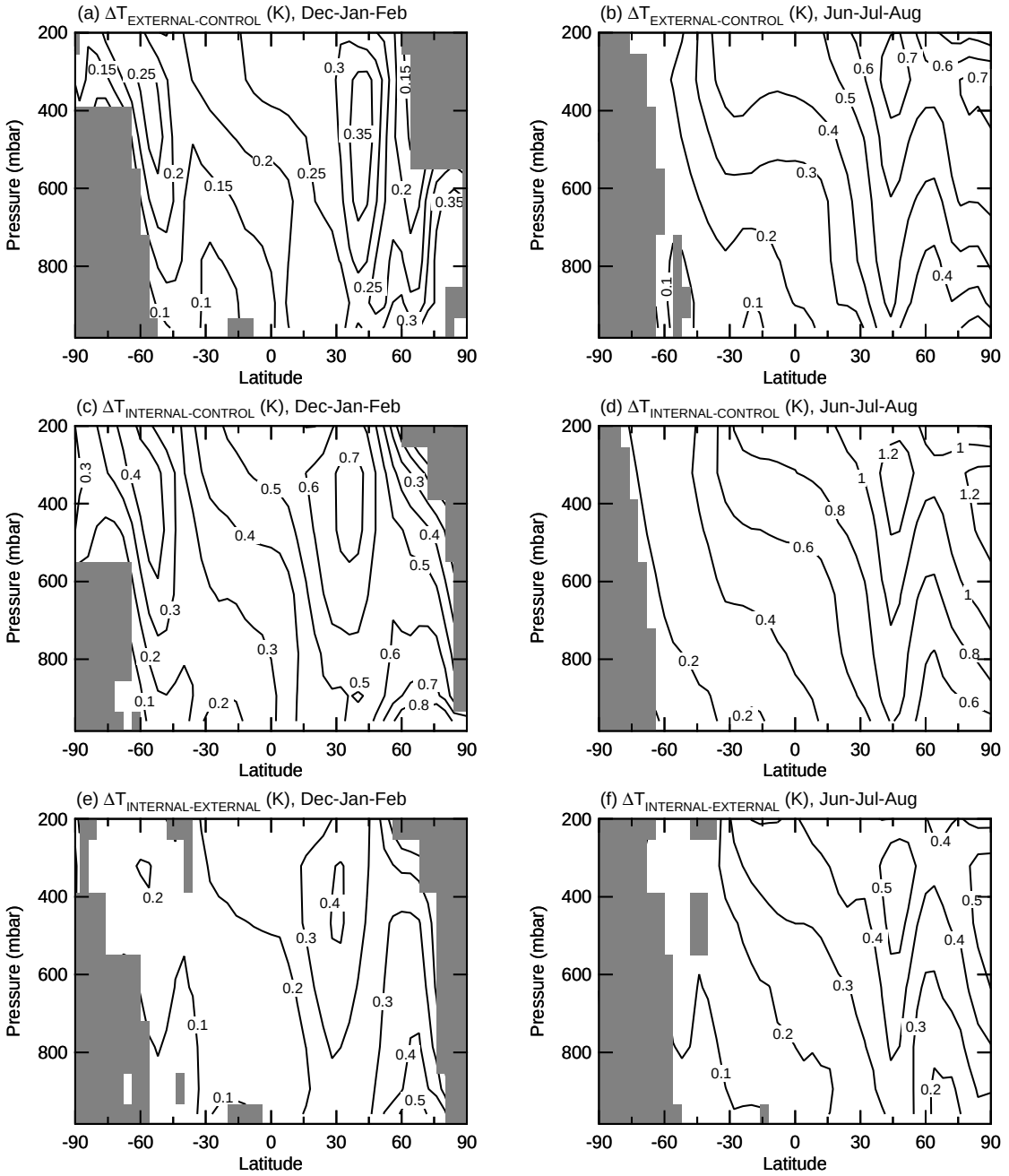

Figure 3.13: Estimated change in zonally averaged equilibrium temperature (K) as a function of pressure for December-January-February (left panel) and June-July-August (right panel) for EXTERNAL minus CONTROL (top panel), INTERNAL minus CONTROL (middle panel), and INTERNAL minus EXTERNAL (bottom panel). Gray indicates areas where the difference is not significant at the 95% confidence level.

creases most in the low latitudes and during JJA. As expected, the increase is greater if BC is assumed to be internally mixed with sulfate instead of externally mixed. Given that water vapor is a greenhouse gas, the increase in water vapor mixing ratio leads to a positive feedback loop on the temperature response.

Another obvious change in the hydrological cycle is reflected in precipitation change, which is shown in Figure 3.15. BC radiative forcing is predicted to increase precipitation between 0 and 20degN and decrease precipitation between 0 and 20degS, effectively shifting the ITCZ northward. This result is similar to that predicted by *Roberts and Jones* [2004] and *Wang* [2004]. The greatest change occurs over the central Pacific, away from the location of largest BC forcing. The change in precipitation pattern can be explained by the enhanced interhemispheric temperature difference, which induces a change in the zonal mean meridional circulation and convection in the tropics. Figure 3.16 shows the predicted change in annually and zonally averaged mass stream function. In the NH equatorial region, the ascending branch of the mean meridional circulation is enhanced, accompanied by a strong moisture flux convergence, leading to increased precipitation. Just south of the equator, the opposite is true: the ascending branch of the zonal mean meridional circulation is weakened, reducing precipitation. The change in the meridional circulation occurs both in winter and summer, i.e., the Hadley cell circulation is weakened during DJF and strengthened during JJA. Note that the predicted change in meridional flow and precipitation pattern is opposite to that of *Chen and Ramaswamy* [1996b], who studied the climate sensitivity to increased cloud liquid water path between 20deg-70degN. In that study, increased cloud albedo in the NH leads to larger cooling in the NH than in the SH, leading to change in the meridional transport such that precipitation is increased south of the equator and reduced north of the equator.

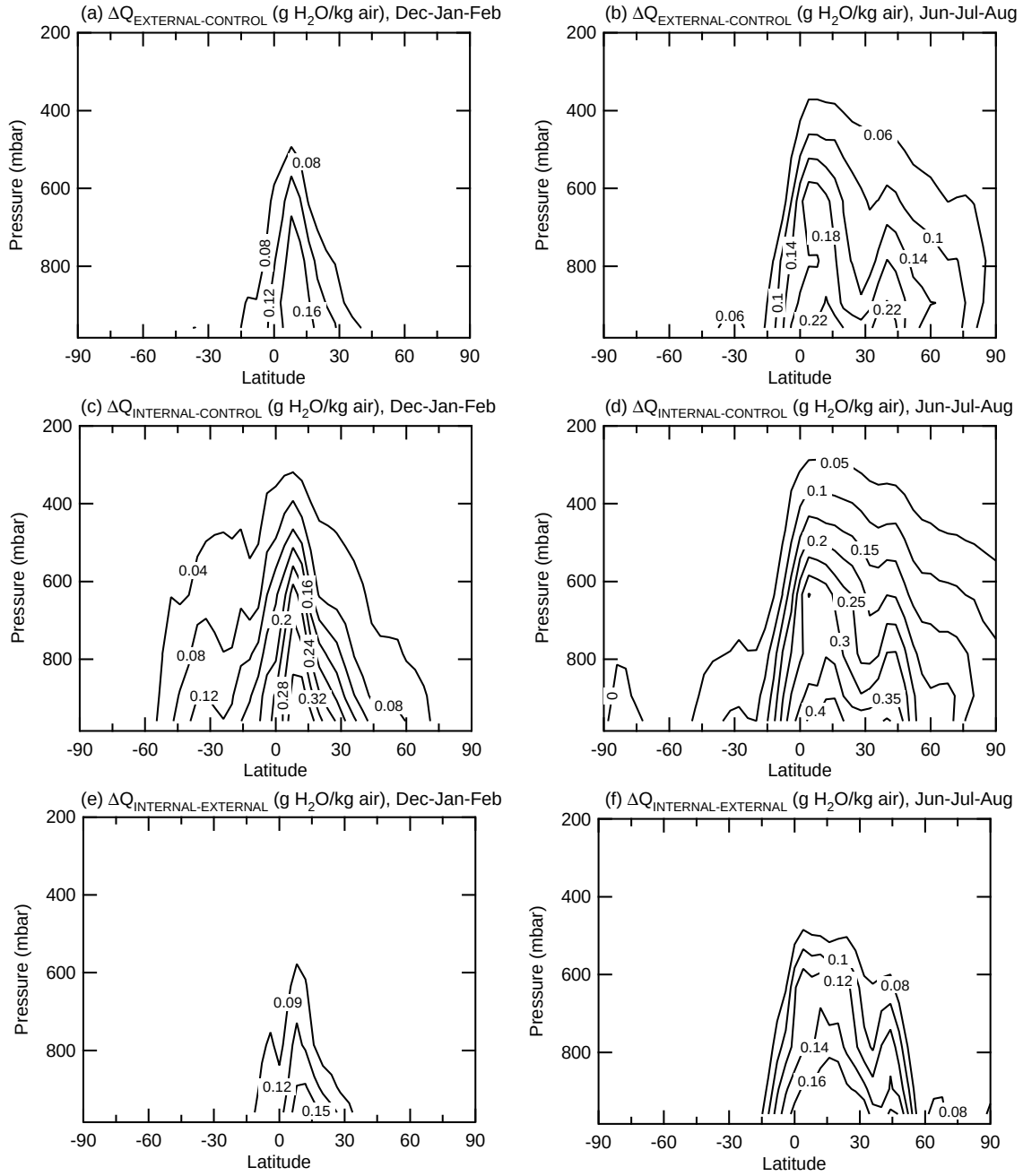

Figure 3.14: Estimated change in zonally averaged equilibrium specific humidity (g H_2O/kg air) as a function of pressure for December-January-February (left panel) and June-July-August (right panel) for EXTERNAL minus CONTROL (top panel), INTERNAL minus CONTROL (middle panel), and INTERNAL minus EXTERNAL (bottom panel). All non-zero contour lines indicate that the difference is significant at the 95% confidence level.

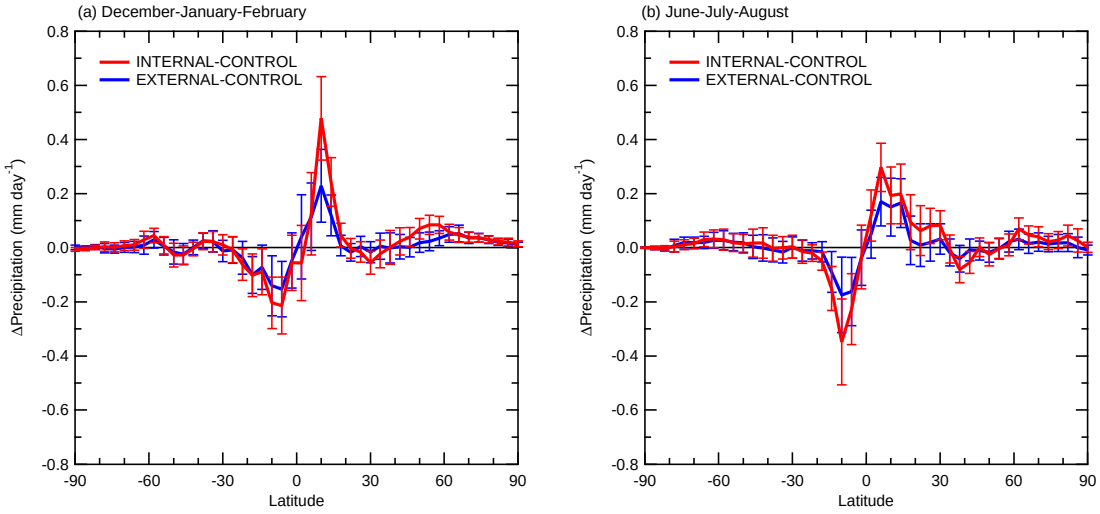

Figure 3.15: Estimated change in zonally averaged equilibrium precipitation rate (mm day^{-1}) for (a) December-January-February and (b) June-July-August. The error bars indicate 95% confidence intervals.

The change in precipitation pattern around the tropics correlates with change in convective cloud cover. Figure 3.17 shows the predicted zonal mean change in convective and large-scale cloud cover. The increase in precipitation between 0deg to 20degN is matched closely by increased convective cloud cover; similarly, the decrease in precipitation between 0deg and 20degS is accompanied by reduction in convective cloud cover. Note that even though BC direct radiative forcing is the greatest over the NH, the reduction in convective cloud cover in the SH is greater than the corresponding increase in the NH. For both convective cloud cover and precipitation, the largest response occurs during the winter months of each hemisphere. As seen from Figure 3.18, which shows the change in cloud cover for each hemisphere as a function of pressure, the change in cloud cover occurs predominately between 300 and 500 mbar. Similar to the temperature response, the impact of BC direct radiative forcing on cloud cover is greater in the case of internally-mixed BC than in the case of externally-mixed BC.

In addition to change in convective cloud, direct radiative of BC is also predicted to

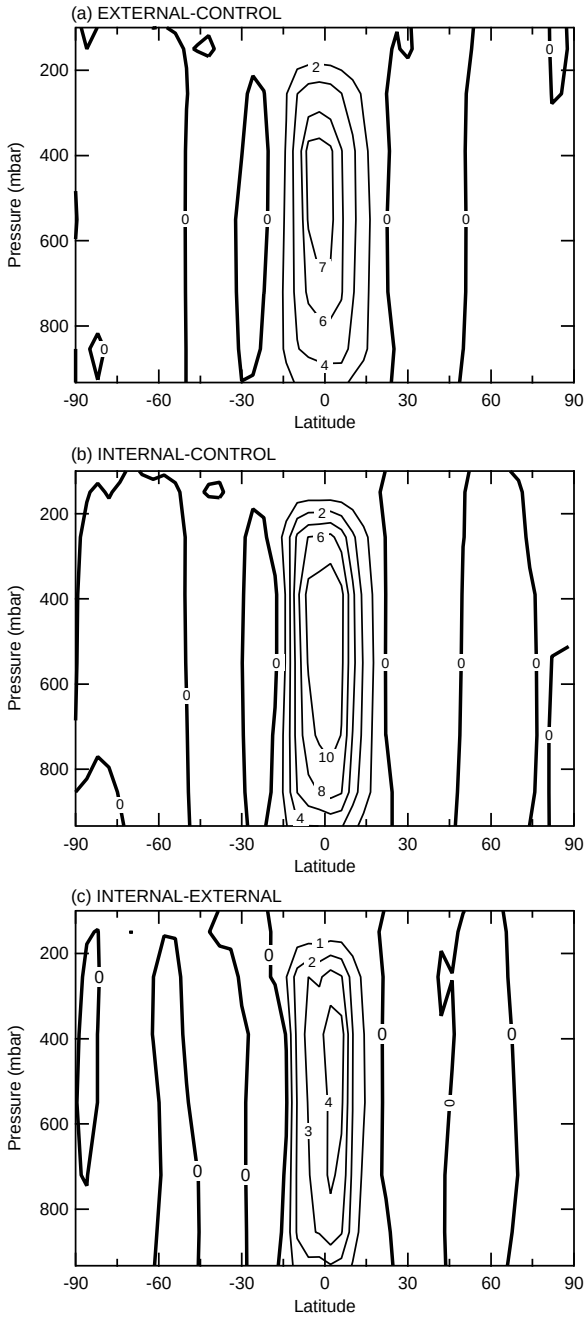

Figure 3.16: Estimated change in zonally and annually averaged mass stream function (10^9 kg s^{-1}) as a function of pressure. Positive values indicate anti-clockwise circulation. All non-zero contour lines indicate that the difference is significant at the 95% confidence level.

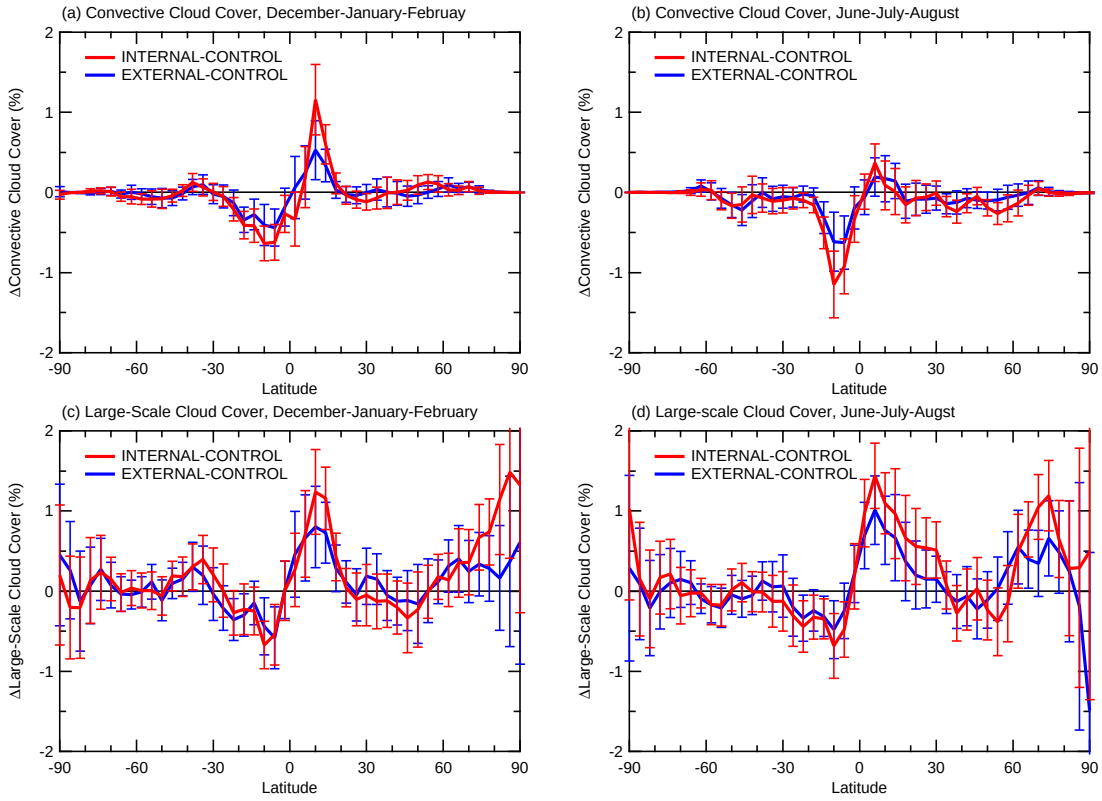

Figure 3.17: Estimated change in zonally averaged equilibrium cloud cover for December-January-February (left left panel) and June-July-August (right panel) for convective cloud (top panel) and large-scale cloud (bottom panel). The error bars indicate 95% confidence intervals.

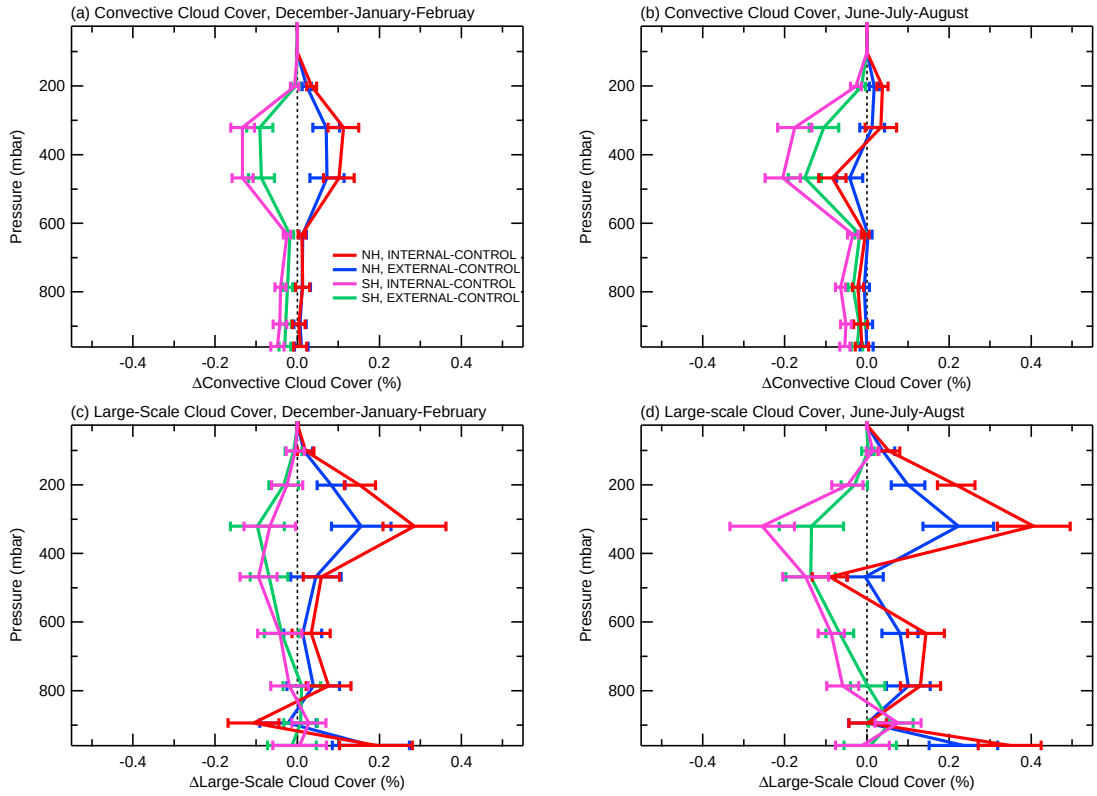

Figure 3.18: Estimated change in hemispherically averaged equilibrium cloud cover as a function of pressure for convective (top panel) and large-scale (bottom panel) clouds for December-January-February (left left panel) and June-July-August (right-panel). The error bars indicate 95% confidence intervals.

change large-scale cloud cover, which is shown in Figures 3.17 and 3.18. Around the equator, the change in large-scale clouds is similar to the change in convective clouds, again due to increased northward transport of water vapor across the equator near the surface, resulting in increased cloud cover in the northern equatorial region and reduction in cloud cover in the southern equatorial region. Because of radiative warming of BC in northern mid- and high latitudes, low and mid-level covers are reduced, but high cloud cover is increased even more due to decreased static stability. This semi-direct effect of absorbing aerosol is also observed in the study of *Cook and Highwood* [2004] and is similar to the effect of the "ghost" forcing experiments of *Hansen et al.* [1997]. According to *Hansen et al.* [1997], for high clouds (above 7-8 km), the warming from the greenhouse effect of cloud water on globally averaged surface air temperature dominates the cooling from the cloud albedo effect. The competing cloud albedo and greenhouse effects are especially strong in the northern tropics, as seen in Figure 3.19, which shows the predicted change in zonal mean equilibrium shortwave and longwave radiative fluxes. In the northern tropics the increase in high level clouds reflects more solar radiation back to space such that the net solar radiation absorbed by the planet is negative even though the initial perturbation of direct radiative forcing is positive. The greenhouse effect of high clouds, however, leads to net warming. In contrast to high clouds, for mid- and low level clouds, the albedo effect dominates the greenhouse effect. Therefore, the semi-direct effect of BC introduces a positive feedback on surface temperature increase by reducing low- and mid-level clouds and increasing high level clouds.

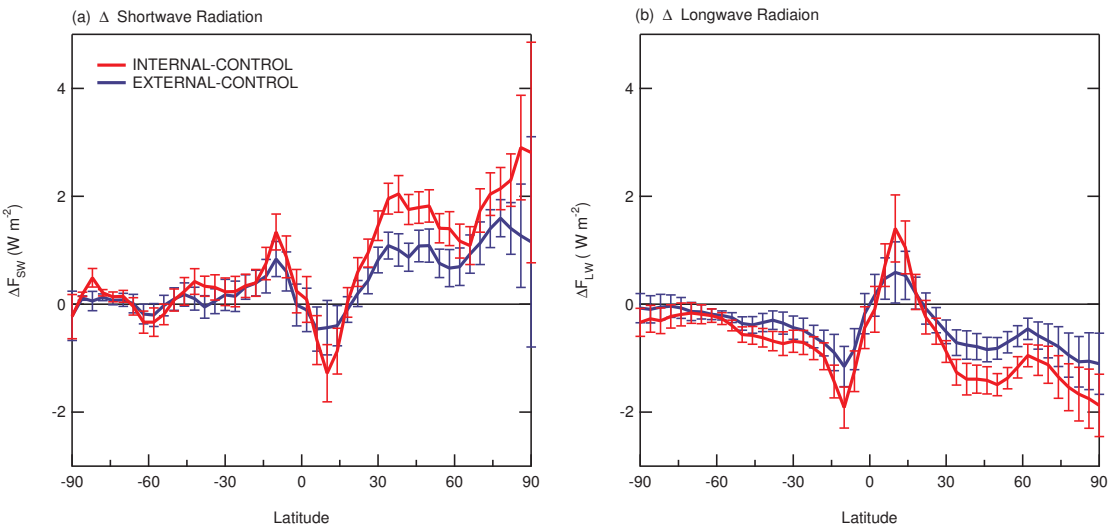

Figure 3.19: Estimated change in zonal mean equilibrium radiative flux of the planet for (a) shortwave radiation and (b) longwave radiation. A positive change indicates warming of the atmosphere. The error bars indicate 95% confidence intervals.

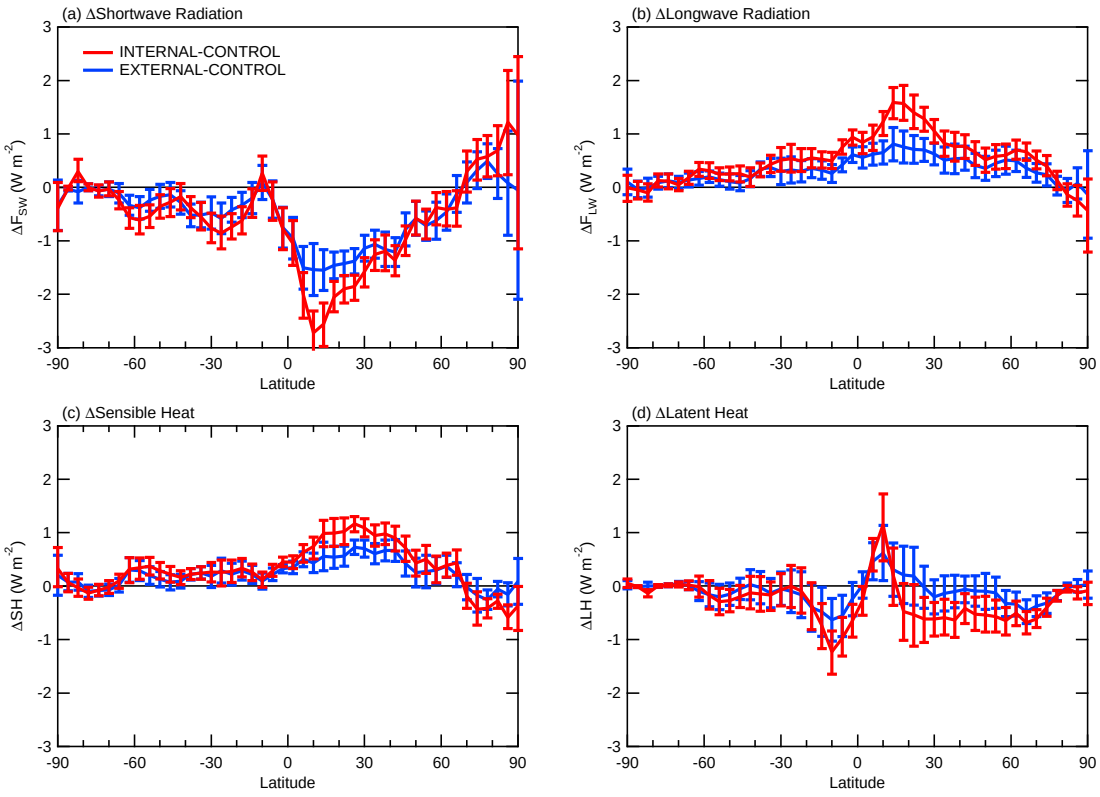

Figure 3.20: Estimated zonal and annual change (W m^{-2}) in (a) shortwave radiative flux, (b) longwave radiative flux, (c) sensible heat flux, and (d) latent heat flux at the the surface. A positive change indicates warming of the surface.

3.4.6 Change in Surface Energy Budget

The climate response due to BC can be studied from the change in surface energy budget. Figure 3.20 shows the zonal and annual mean change in surface energy fluxes. As expected, shortwave absorption by BC in the atmosphere leads to reduction in absorbed shortwave radiation at the surface in most latitudes. In the northern low latitudes, the reduction in absorbed solar radiation at the surface after the climate has reached equilibrium is even greater than the instantaneous direct forcing at the surface that led to the change in climate because increased high cloud cover (see Section 3.4.5) reflected even more solar radiation away from the surface. In the northern high latitudes, solar absorption at the surface actually increases because of the reduction in surface albedo as result of decreased ocean ice coverage and snow depth (see Figure 3.12).

The change in net solar radiation at the surface is compensated by the change in longwave radiation, sensible heat flux, and latent heat flux. Figure 3.20b indicates an increase in net downward longwave radiation. This change is attributed to increase in atmospheric temperature and increased emissivity of a more moist atmosphere. Similar to the change in longwave radiation, decrease in sensible heat flux from the ground to the atmosphere also acts to compensate for the reduction in solar radiation, as the air above the surface is warmed more than the surface. Finally, changes in evaporation result in change in latent heat fluxes, which also correspond to the changes in precipitation pattern discussed in Section 3.4.5.

3.4.7 Black Carbon Distribution

Given that wet-scavenging is the dominant sink for atmospheric BC, one would expect that the global BC distribution would be altered by the change in the hydrological cycle.

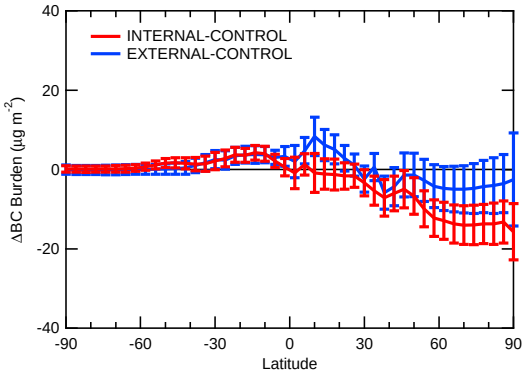

Figure 3.21: Estimated change in annually and zonally averaged BC column burden (μg m^{-2}). The error bars indicate 95% confidence intervals.

Figure 3.21 shows the annually and zonally averaged change in BC burden. As discussed previously, in the tropics precipitation is predicted to increase just north of the equator and decrease just south of the equator. For the case of externally-mixed BC, the reduction in wet scavenging dominates, leading to a slightly increased annually-averaged BC burden around the tropics. In comparison to the case of externally-mixed BC, for the internally-mixed case, the increase in precipitation between 0deg and 20degN is predicted to be greater than the reduction in precipitation between 0deg and 20degS; consequently, the annually-averaged BC burden is predicted to increase between 0deg and 20degS and remained unchanged between 0deg and 20degN. North of 30degN, the change in BC burden is extremely small and only greater than the natural variability of the model when internally-mixed case with sulfate. Overall, the change in global burden of BC is small (on the order of 0.5%) because the change in precipitation is predicted to occur mainly over oceans, away from regions of high BC concentrations.

3.5 Discussion of Uncertainties

The results presented in the previous sections indicate that the climate response of BC is strongly dependent on the mixing state of BC with other aerosols. Given the prediction here that the climate sensitivity of BC radiative forcing is the same regardless of how BC is mixed with sulfate, at least in terms of global and annual mean surface temperature response, the results of this study provide upper and lower estimates for the climate impact of anthropogenic BC for this model. However, this study considers only BC and sulfate. In the real atmosphere, soot is emitted as a mixture of BC and OC such that all individual particles that contain BC also contain OC. Once emitted, these particles can also be mixed with other species via coagulation and condensation. When the amount of scattering material, such as nitrates or organic carbon, that is mixed with BC is increased, the absorbing efficiency of BC is enhanced even more [*Lesins et al.*, 2002], and BC has even greater climate impact.

In addition to the mixing state of BC, other factors also contribute to uncertainties in the predicted direct radiative forcing of BC, which in turn leads to uncertainties of the climate response. Most importantly, direct radiative forcing of BC is strongly dependent on its global distribution. Unfortunately, constraining the model predictions of global BC distribution is difficult due to lack of long term data. The global burden and distribution of BC are most sensitive to the emission rate. *Bond et al.* [2004] suggest an uncertainty range for global BC emissions of 4.3 to 22 Tg yr^{-1}. Assuming radiative forcing scales linearly with emission rate and employing the climate sensitivity of 0.6 K W^{-1} m^2 determined here, the global and annual mean temperature increase attributed to anthropogenic BC is estimated to be between 0.11 and 1.0 K. In the northern polar region, the temperature increase

is bracketed by 0.4 to 3.9 K. Even though the results presented here and from previous studies indicate that the zonal and global mean surface air temperature is, in some sense, independent of the distribution of forcing, regional impacts can still be important. For example, this study indicates anthropogenic BC leads to warming over central and eastern Russia that is not predicted for ozone or CO_2. This is likely a result of high emissions in the former USSR and China; however, in these regions uncertainties are large [*Bond et al.*, 2004].

Another uncertainty is that in this study aerosol scavenging efficiency is treated as independent of the aerosol mixing state when in fact internally-mixed BC are more soluble in water and would be removed more efficiently from the atmosphere by wet deposition. In this study, the solubility of BC is determined by whether it is hydrophobic or hydrophilic (see Section 3.3.3). The hydrophobic fraction of emitted BC is assumed to be 80% regardless of origin, burning characteristics, or meteorological conditions. Once emitted, hydrophobic BC becomes hydrophilic with a constant exponential decay lifetime of 1.15 days. Accurate modeling of solubility of BC would require knowledge of the structure (or surface area) of BC particles and the rate at which they take up condensable gases such as H_2SO_4 and organics. *Cooke et al.* [2002] indicate that a factor of 2 uncertainty in the decay lifetime leads to approximately 20% uncertainty in global burden. In the extreme limit that all BC is emitted as hydrophilic aerosol, the global burden would be reduced by almost half. Overall, the physical and chemical properties of BC yield a factor of 2 uncertainty in the global burden and lifetime.

Limitations of the climate model also make significant contribution to uncertainties in predicting climate response. One important issue is the coarse resolution of the model. According to *Rind and Lerner* [1996], finer vertical resolution in the GCM could lead to

stronger convection and result in stronger coupling between the upper troposphere and the surface. Stronger convection would certainly be a factor in the change in the zonal mean precipitation pattern that is found in this study. A universal problem with all current GCMs is that the horizontal resolution does not resolve subgrid-scale cloud processes that could be important for BC-cloud interactions. Another factor is because in the climate model used for this study, the ocean ice albedo in the SH is set at a low value 0.25 to achieve a realistic ocean ice cover, climate response in the SH is dampened. Given that most of the forcing occurs in the NH and forcing is nearly zero southward of 60degS, the error introduced by the low SH ocean ice albedo is likely small. Finally, land-surface processes such as those affecting the distribution of water and thermodynamics of the boundary layer are another source of uncertainty in climate predictions.

3.6 Conclusions

This study examines the interaction between BC and climate in a three-dimensional climate model. Three 100-year climate simulations are carried out, and the changes in equilibrium climate due to direct radiative forcing of anthropogenic BC are analyzed. Anthropogenic BC is predicted to raise global and annual mean surface air temperature by 0.20 to 0.37 K depending on whether BC is externally- or internally-mixed with the present-day level of sulfate aerosol, indicating that the mixing state of BC contributes to significant uncertainty in the temperature response. Over the northern high latitudes, the predicted surface air temperature increases by more than 1 K during winter and early spring. The large sensitivity at the high latitudes is a result of high surface albedo and positive feedback in which warming causes reduction in ice and snow cover, leading to reduced surface albedo and more absorbed solar radiation. Other than the northern high latitudes, sub-

stantial surface warming is predicted to also occur over most of Asia and the Atlantic and Pacific oceans. When BC is internally mixed with sulfate aerosol, the geographical extent of predicted surface warming covers the entire NH as well as parts of the SH. The results indicate that regional climate impacts of BC can be important, but not necessarily local to the place of maximum forcing. The zonal mean pattern of surface response of BC direct radiative forcing is similar to that of ozone and CO_2 using the same GCM; however, significant warming is predicted for BC over central Russia but not for ozone or CO_2, suggesting that the regional climate impact of BC is different from that of ozone and CO_2. Other than at the surface, the temperature is predicted to increase throughout the troposphere, especially around 45degN and 400 mbar, which overlaps with the location of largest BC forcing. Over the tropics, the maximum warming occurs in the upper troposphere.

In addition to the thermal response, direct radiative forcing of BC is also predicted to a change precipitation patterns in the tropics. Due to the change in the meridional temperature gradient between the northern and southern hemispheres, a change in the Hadley cell circulation leads to increased precipitation north of the equator and compensating reduction in precipitation south of the equator. Despite wet-scavenging being the dominant sink for atmospheric BC, the global distribution of BC is not expected to change significantly because the change in precipitation pattern tends to occur over the oceans, away from regions of high BC loading. The change in precipitation pattern away from the regions of largest BC forcing is one example of the complex nature of the climate response.

For both externally- and internally-mixed BC, the predicted climate sensitivity of BC direct radiative forcing is estimated to 0.6 K W^{-1} m^2, suggesting that a linear relationship between forcing and surface temperature response is valid for BC (i.e., Equation (3.1)). The predicted sensitivity is about 30% less than that of doubled CO_2 and similar to that of

anthropogenic ozone forcing, all using the same climate model. Even though the predicted direct radiative forcing and climate sensitivity of anthropogenic BC are smaller than those of CO_2, regional differences in temperature and precipitation response still make climate impact of BC important. Overall, larger forcing for internally-mixed BC leads to greater climate response. The increase in temperature, changed precipitation pattern, and altered cloud coverage are all enhanced if BC is assumed to be internally mixed with sulfate instead of externally mixed. These results confirm that the mixing state of BC with other aerosols is important in determining its climate effect.

3.7 Acknowledgments

This work was supported by the National Aeronautics and Space Administration Earth Observing System Interdisciplinary Science program (NASA EOS-IDS). Serena Chung was supported by a National Science Foundation Graduate Fellowship. The authors thank Loretta Mickley and Jean Lerner for assistance.

Chapter 4

Summary and Conclusions

In an effort to better understand and quantify the climate effects of carbonaceous aerosols, three-dimensional simulation of carbonaceous aerosols has been implemented online in a general circulation model (GCM). Chapter 2 reports the details of the model, which include black carbon (BC) and primary organic aerosol (POA) from fossil fuel and biomass burning, as well as secondary organic aerosol (SOA) from the oxidation of biogenic hydrocarbons. Predicted BC concentrations are generally low at rural and marine sites when compared with limited available measurements. In comparison to BC and OC concentrations measured at rural sites in the United States, predictions are consistently low, suggesting that the carbonaceous aerosol emissions inventory use might be too low in the U.S. Overall, the results suggest that wet-scavenging, the dominant sink for carbonaceous aerosols, may be overestimated. More accurate predictions of wet-scavenging require better knowledge of the solubility of carbonaceous aerosols. Still, constraining the model prediction is difficult due the lack of long term data.

Simulation of SOA provides an interesting result in that unlike BC and POA, which have the largest concentrations at the earth's surface near source regions, SOA is predicted to accumulate in cold regions of the upper troposphere. The reason is that semi-volatile gas-phase oxidation products are transported to higher altitudes where colder temperatures

allow more products to condense. Such predictions of secondary maxima of SOA levels in the cold regions of the upper troposphere have not been verified observationally, although the physics leading to this phenomenon is quite evident.

Since the preindustrial period, human activities are predicted to have increased global burdens of BC and OC by an order of magnitude and almost tripled the SOA production rate. The direct radiative forcings due to the increased atmospheric burdens of these aerosols are estimated in the second part of Chapter 2. Because BC absorbs solar radiation, its direct radiative effect is dependent on how it is mixed with other (scattering) aerosols. Globally and annually averaged, top of the atmosphere (TOA) radiative forcing by anthropogenic BC is predicted to be +0.51 W m^{-2} if BC is assumed to be physically separated from other aerosols. If BC is internally mixed with sulfate and OC, the estimate is +0.8 W m^{-2}. For OC (both POA and SOA), the estimated anthropogenic direct radiative forcing is -0.1 to -0.2 W m^{-2}, depending on the water-uptake property of OC. For the ensemble of BC, OC and sulfate aerosols, global and annual mean anthropogenic direct radiative forcing at TOA is estimated to be -0.39 to -0.78 W m^{-2}, depending on the exact assumptions of aerosol mixing and water uptake by OC. As expected, the net effect of direct radiative forcing of anthropogenic aerosols is to offset warming by greenhouse gases (GHGs).

The estimates of direct radiative forcing for carbonaceous aerosols indicate that BC has a larger impact than OC. Chapter 3 studies the climate effect of direct radiative forcing of anthropogenic BC using a GCM coupled to a mixed-layer ocean model. Here, an updated emission inventory of BC is used. Based on the new emission inventory, direct radiative forcing of anthropogenic BC at TOA is estimated +0.33 and +0.6 W m^{-2}, for BC mixed externally and internally with present-day level of sulfate, respectively. Anthropogenic BC is predicted to raise globally and annually averaged equilibrium surface air temperature by

0.20 K if BC is assumed to be externally mixed. The predicted increase is significantly greater in the Northern Hemisphere (0.29 K) than in the Southern Hemisphere (0.11 K). If BC is assumed to be internally mixed with the present-day level of sulfate aerosol, the predicted annual mean surface temperature increase rises to 0.37 K globally, 0.54 K for the Northern Hemisphere, and 0.20 K for the Southern Hemisphere. Even though the predicted global-averaged warming due to BC is less than that of GHGs, significant regional differences do exist. In addition to temperature increase, direct radiative forcing of anthropogenic BC is also predicted to lead to a change in precipitation patterns in the tropics by shifting the intertropical convergence zone northward, a phenomenon not predicted for GHGs.

Even though progress has been made toward understanding of the climate impact of carbonaceous aerosols, large uncertainties still exist. More accurate predictions of the global distribution of aerosols are hindered by uncertainties in factors such as emission rates and representation of wet-scavenging and by limitations of the GCM, e.g. coarse resolutions and unresolved cloud processes. Unfortunately, constraining the model predictions is difficult due to lack of long term data. As already alluded to several times in the discussions of aerosol mixing state, carbonaceous aerosols do not exist independently in the atmosphere. Ultimately, all aerosols and GHGs need to be considered as a whole to better predict the impact of anthropogenic activities on future climate.

Bibliography

Adams, P. J., J. H. Seinfeld, and D. M. Koch, Global concentrations of tropospheric sulfate, nitrate, and ammonium aerosol simulated in a general circulation model, *J. Geophys. Res.*, *104*, 13,791–13,823, 1999.

Adams, P. J., J. H. Seinfeld, D. M. Koch, L. Mickley, and D. Jacob, General circulation model assessment of direct radiative forcing by sulfate-nitrate-ammonium-water inorganic aerosol system, *J. Geophys. Res.*, *106*(D1), 1097–1111, 2001.

Andersson-Sköld, Y., and D. Simpson, Secondary organic aerosol formation in northern Europe: a model study, *J. Geophys. Res.*, *106*(D7), 7357–7374, 2001.

Andreae, M. O., T. W. Andreae, R. J. Ferek, and H. Raemdonck, Long-range transport of soot carbon in the marine atmosphere, *Sci. Total Environ.*, *36*, 73–80, 1984.

Atkinson, R., Gas-phase tropospheric chemistry of organic compounds, *J. Phys. Chem. Ref. Data*, *Monograph No. 2*, 1994.

Atkinson, R., Gas-phase tropospheric chemistry of volatile organic compounds: 1. alkanes and alkenes, *J. Phys. Chem. Ref. Data*, *26*, 215–290, 1997.

Atkinson, R., J. Arey, S. M. Aschmann, S. B. Corchnoy, and Y. Shu, Rate constants for the gas-phase reactions of *cis*-3-hexen-1-ol, *cis*-3-hexenylacetate, *trans*-2-hexenal, and

linalool with OH and NO_3 radicals and O_3 at 296±2 K and OH radical formation yields from the O_3 reactions, *Int. J. Chem. Kinet.*, *27*, 941–955, 1995.

Bahrmann, C. P., and V. K. Saxena, Influence of air mass history on black carbon concentrations and regional climate forcing in southeastern United States, *J. Geophys. Res.*, *103*(D18), 23,153–23,161, 1998.

Baltensperger, U., H. W. Gäggeler, D. T. Jost, M. Lugauer, M. Schwikowski, and E. Weingartner, Aerosol climatology at the high-Alpine site Jungfraujoch, Switzerland, *J. Geophys. Res.*, *102*(D16), 19,707–19,715, 1997.

Barth, M. C., P. J. Rasch, J. T. Kiehl, C. M. Benkovitz, and S. E. Schwartz, Sulfur chemistry in the National Center for Atmospheric Research Community Climate Model: Description, evaluation, features, and sensitivity to aquesous chemistry, *J. Geophys. Res.*, *105*(D1), 1387–1415, 2000.

Benkovitz, C. M., C. M. Berkowitz, R. C. Easter, S. Memesure, R. Wagner, and S. E. Schwartz, Sulfate over the North Atlantic and adjacent continental regions: Evaluation for October and November 1986 using a three-dimensional model driven by observation-derived meteorology, *J. Geophys. Res.*, *99*, 20,725–20,756, 1994.

Berner, A., S. Sidla, Z. Galambos, C. Kruisz, and R. Hitzenberger, Modal character of atmospheric black carbon size distributions, *J. Geophys. Res.*, *101*(D14), 19,559–19,565, 1996.

Bizjak, M., J. Tursic, M. Lesnjak, and T. Cegnar, Aerosol black carbon and ozone measurements at Mt. Krvavec EMEP GAW station, Slovenia, *Atmos. Environ.*, *33*(17), 2783–2787, 1999.

Bodhaine, B. A., Aerosol absorption measurements at Barrow, Mauna- Loa and the south-pole, *J. Geophys. Res.*, *100*(D5), 8967–8975, 1995.

Boer, G. J., and B. Yu, Climate sensitivity and response, *Clim. Dynam.*, *20*(4), 415–429, 2003.

Bond, T. C., Light Absorption by Primary Particles from Fossil-Fuel Combustion: Implication for Radiative Forcing, Ph.D. thesis, University of Washington, Seattle, Washington 98195, 2000.

Bond, T. C., D. G. Streets, K. F. Yarber, S. M. Nelson, J. Woo, and Z. Klimont, A technology-based global inventory of black and organic carbon emissions from combustion, *J. Geophys. Res.*, *109*(D14), D14203, doi:10.1029/2003JD003697, 2004.

Cachier, H., M. P. Brémond, and P. Buat-Ménard, Determination of atmospheric soot carbon with a simple thermal method, *Tellus*, *41B*, 379–390, 1989.

Cachier, H., M. P. Brémond, and P. Buat-Ménard, Organic and black carbon aerosols over marine regions of the Northern Hemisphere, in *Proceedings of the International Conference on Global and Regional Environmental Atmospheric Chemistry*, edited by L. Newman, W. Wang, and C. S. Kiang, pp. 249–261, Department of Energy, Brookhaven National Laboratory, Upton, New York, 1990.

Cadle, S. H., and J. M. Dasch, Wintertime concentrations and sinks of atmospheric particulate carbon at a rural location in northern Michigan, *Atmos. Environ.*, *22*(7), 1373–1381, 1988.

Calogirou, A., B. R. Larsen, and D. Kotzias, Gas-phase terpene oxidation products: A review, *Atmos. Environ.*, *33*, 1423–1439, 1999.

Castro, L. M., C. A. Pio, R. M. Harrison, and D. J. T. Smith, Carbonaceous aerosol in urban and rural European atmospheres: estimation of secondary organic carbon concentrations, *Atmos. Environ.*, *33*(17), 2771–2781, 1999.

Charlson, R. J., J. Langner, H. Rodhe, C. B. Leovy, and S. G. Warren, Peturbation of the Northern Hemisphere radiative balance by backscattering from anthropogenic sulfate aerosols, *Tellus*, *43AB*, 152–163, 1991.

Chen, C.-T., and V. Ramaswamy, Sensitivity of simulated global climate to perturbations in low-cloud microphysical properties. Part I: Globally uniform perturbations, *J. Clim.*, *9*, 1385–1402, 1996a.

Chen, C.-T., and V. Ramaswamy, Sensitivity of simulated global climate to perturbations in low-cloud microphysical properties. Part II: Localized perturbations, *J. Clim.*, *9*, 2788–2801, 1996b.

Chesselet, R., M. Fontugne, P. Buat-Ménard, U. Ezat, and C. E. Lambert, The origin of particulate organic carbon in the marine atmosphere as indicated by its stable carbon isotopic composition, *Geophys. Res. Lett.*, *8*(4), 345–248, 1981.

Chin, M., D. J. Jacob, G. M. Gardner, M. S. Foreman-Fowler, and P. A. Spiro, A global three-dimensional model of tropospheric sulfate, *J. Geophys. Res.*, *101*(D13), 18,667–18,690, 1996.

Chow, J. C., J. G. Watson, E. M. Fujita, Z. Q. Lu, D. R. Lawson, and L. L. Ashbaugh, Temporal and spatial variations of $PM_{2.5}$ and PM_{10} aerosol in the Southern California Air- Quality Study, *Atmos. Environ.*, *28*(12), 2061–2080, 1994.

Chuang, C. C., J. E. Penner, K. E. Taylor, A. S. Grossman, and J. J. Walton, An assessment

of the radiative effects of anthropogenic sulfate, *J. Geophys. Res.*, *102*(D3), 3761–3778, 1997.

Chung, S. H., and J. H. Seinfeld, Global distribution and climate forcing of carbonaceous aerosols, *J. Geophys. Res.*, *107*(D19), 4407, doi:10.1029/2001JD001397, 2002.

Chýlek, P., G. Videen, D. Ngo, R. G. Pinnick, and J. D. Klett, Effect of black carbon on the optical properties and climate forcing of sulfate aerosols, *J. Geophys. Res.*, *100*(D8), 16,325–16,332, 1995.

Chýlek, P., L. Kou, B. Johnson, F. Boudala, and G. Lesins, Black carbon concentrations in precipitation and near surface air in and near Halifax, Nova Scotia, *Atmos. Environ.*, *33*(14), 2269–2277, 1999.

Cook, J., and J. Highwood, Climate response to tropospheric absorbing aerosols in an intermediate general-circulation model, *Q. J. R. Meteorol. Soc.*, *130*, 175–191, 2004.

Cooke, W. F., and J. J. N. Wilson, A global black carbon aerosol model, *J. Geophys. Res.*, *101*, 19,395–19,409, 1996.

Cooke, W. F., S. G. Jennings, and T. G. Spain, Black carbon measurements at Mace Head, 1989-1996, *J. Geophys. Res.*, *102*(D21), 25,339–25,346, 1997.

Cooke, W. F., C. Liousse, H. Cachier, and J. Feichter, Construction of a 1deg $\times$1 deg fossil fuel emission data set for carbonaceous aerosol and implementation and radiative impact in the ECHAM4 model, *J. Geophys. Res.*, *104*, 22,137–22,162, 1999.

Cooke, W. F., V. Ramaswamy, and P. Kasibhatla, A general circulation model study of the global carbonaceous aerosol distribution, *J. Geophys. Res.*, *107*(D16), 4279, doi: 10.1029/2001JD001274, 2002.

d'Almeida, G. A., P. Koepke, and E. P. Shettle, *Atmospheric Aerosol: Global Climatology and Radiative Characteristsics*, A. Deepak Publishing, Hampton, VA, 1991.

Dana, M. T., and J. M. Hales, Statistical aspects of the washout of polydispersed aerosols, *Atmos. Environ.*, *10*, 45–50, 1976.

Darzi, M., and J. W. Winchester, Aerosol characterstics at Mauno Loa Observatory, Hawaii, after east Asian dust storm episodes, *J. Geophys. Res.*, *87*(C2), 1251–1258, 1982.

Davidson, C. I., S. F. Lin, and J. F. Osborn, Indoor and outdoor air pollution in the Himalayas, *Environ. Sci. Technol.*, *20*(6), 561–567, 1986.

Del Genio, A. D., and Y. Yao, Efficient cumulus parameterization for long-term climate studies: The GISS scheme, in *The Representation of Cumulus Convection in Numerical Models Monogr. 46*, edited by K. E. Emanuel and D. J. Raymond, pp. 181–184, American Meteorol. Soc., Boston, Mass., 1993.

Del Genio, A. D., M.-S. Yao, W. Kavari, and K. K.-W. Lo, A prognostic cloud water parameterization for global climate models, *J. Clim.*, *9*, 270–304, 1996.

Dzubay, T. G., R. K. Stevens, and P. L. Haagenson, Composition and origins of aerosol at a forested mountain in Soviet Georgia, *Environ. Sci. Technol.*, *18*, 873–883, 1984.

Falk, A., E. Gullstrand, A. Löf, and E. Wigaeus-Hjelm, Liquid/air partition coefficients of four terpenes, *British J. of Industrial Medicine*, *47*, 62–64, 1990.

Feichter, J., E. Kjellstrom, H. Rodhe, F. Dentener, J. Lelieveld, and G. J. Roelofs, Simulation of the tropospheric sulfur cylcel in a global climate model, *Atmos. Environ.*, *30*, 1693–1707, 1996.

Feichter, J., U. Lohmann, and I. Schult, The atmospheric sulfur cycle in ECHAM-4 and its impact on the shortwave radiation, *Clim. Dynam.*, *13*(4), 235–246, 1997.

Fitzgerald, J. W., Approximation formulas for the equilibrium size of an aerosol as a function of its dry size and composition and the ambient relative humidity, *J. Appl. Metereo.*, *14*, 1044–1049, 1975.

Forster, P., M. Blackburn, R. Glover, and K. Shine, An examination of climate sensitivity for idealised climate change experiments in an intermediate general circulation model, *Clim. Dynam.*, *16*(10-11), 833–849, 2000.

Grégoire, J.-M., K. Tansey, and J. Silva, The GBA2000 initiative: Developing a global burned area database from SPOT-VEGETATION imagery, *Int. J. Remote Sens.*, *24*(6), 1369–1376, 2003.

Griffin, R. J., D. R. Cocker, III, R. C. Flagan, and J. H. Seinfeld, Organic aerosol formation from the oxidation of biogenic hydrocarbons, *J. Geophys. Res.*, *104*, 3555–3567, 1999a.

Griffin, R. J., D. R. Cocker, III, J. H. Seinfeld, and D. Dabdub, Estimate of global atmospheric organic aerosol from oxidation of biogenic hydrocarbons, *Geophys. Res. Lett.*, *26*, 2721–2724, 1999b.

Guenther, A., C. N. Hewitt, D. Erickson, R. Fall, C. Geron, T. Graedel, P. Harley, L. Klinger, M. Lerdau, W. A. McKay, T. Pierce, B. Sholes, R. Steinbrecher, R. Tallamraju, J. Taylor, and P. Zimmerman, A global model of natural volatile organic compound emissions, *J. Geophys. Res.*, *100*, 8873–8892, 1995.

Hansen, A. D. A., H. Rosen, and T. Novakov, Real-time measurement of the absorption coefficient of aerosol particles, *Appl. Opt.*, *21*(17), 3060–3062, 1982.

Hansen, A. D. A., V. N. Kapustin, and A. D. Polissar, Measurements of airbon carbonaceous aerosols in the eastern Arctic, *Izv. Acad. Sci. USSR Atmos. Oceanic Phys. Engl. Transl.*, *27*(6), 429–433, 1991.

Hansen, J., and L. Nazarenko, Soot climate forcing via snow and ice albedos, *Proc. Natl. Acad. Sci.*, *101*(2), 123–428, doi:10.1073/pnas.2237157100, 2004.

Hansen, J., G. Russell, D. R. P. Stone, A. Lacis, S. Lebedeff, R. Ruedy, and L. Travis, Efficient three-dimensional global models for climate studies: Model I and II, *Mon. Weather Rev.*, *111*, 609–662, 1983.

Hansen, J., A. Lacis, G. Russell, P. Stone, I. Fung, R. Ruedy, and J. Lerner, Climate sensitivity: Analysis of feedback mechanisms, in *Climate Processes and Climate Sensitivity, Geophys. Monogr. Ser., Vol. 29*, edited by J. E. Hansen and T. Takahashi, pp. 130–163, American Geiphysical Union, Washington, D.C., 1984.

Hansen, J., M. Sato, and R. Reudy, Radiative forcing and climate response, *J. Geophys. Res.*, *102*(D6), 6831–6864, 1997.

Harris, J. M., and J. D. Kahl, A descriptive atmospheric transport climatology of the Mauna Loa Obervatory, using clustered trajectories, *J. Geophys. Res.*, *95*(D9), 13,651–13,667, 1990.

Hartke, G. J., and D. Rind, Improved surface and boundary layer models for the Goddard Institute for Space Studies general circulation model, *J. Geophys. Res.*, *102*, 16,407–16,422, 1997.

Haywood, J. M., and V. Ramaswamy, Global sensitivity studies of the direct forcing due to

anthropogenic sulfate and black carbon aerosols, *J. Geophys. Res.*, *103*(D6), 6043–6058, 1998.

Haywood, J. M., and K. P. Shine, The effect of anthropogenic sulfate and soot aerosol on the clear sky planetary radiation budget, *Geophys. Res. Lett.*, *22*, 603–605, 1995.

Haywood, J. M., D. L. Roberts, A. Slingo, J. M. Edwards, and K. P. Shine, General circulation model calculations of the direct radiative forcing by anthropogenic sulfate and fossil-fuel soot aerosol, *J. Clim.*, *10*, 1562–1577, 1997.

Heintzenberg, J., Size-segregated measurements of particulate elemental carbon and aerosol light-absorption at remote Arctic locations, *Atmos. Environ.*, *16*(10), 2461–2469, 1982.

Heintzenberg, J., and E. K. Bigg, Tropospheric transport of trace substances in the Southern Hemisphere, *Tellus*, *42B*, 355–363, 1990.

Heintzenberg, J., and C. Leck, Seasonal variation of the atmospheric aerosol near the top of the marine boundary layer over Spitzenberg related to the Arctic sulfur cycle, *Tellus*, *46B*, 52–67, 1994.

Heintzenberg, J., and A. Mészáros, Elemental carbon, sulfur and metals in aerosol samples at a Hungarian regional air pollution station, *IDŐJÁRÁS*, *89*(6), 313–319, 1985.

Heintzenberg, J., K. Müller, W. Birmili, G. Spindler, and A. Wiedensohler, Mass-related aerosol properties over the Leipzig basin, *J. Geophys. Res.*, *103*(D11), 13,125–13,135, 1998.

Hitzenberger, R., A. Berner, H. Giebl, R. Koch, S. M. Larson, A. Rouc, A. Koch, S. Marischka, and H. Puxbaum, Contribution of carbonaceous material to cloud conden-

sation nuclei concentrations in European background (Mt. Sonnblick) and urban (Vienna) aerosols, *Atmos. Environ.*, *33*, 2647–2659, 1999.

Hoffman, E. J., and R. A. Duce, The organic carbon content of marine aerosols collected on Bermuda, *J. Geophys. Res.*, *79*(30), 4474–4477, 1974.

Hoffman, E. J., and R. A. Duce, Organic carbon in marine atmospheric particulate matter: Concentration and particle size distribution, *Geophys. Res. Lett.*, *4*(10), 449–452, 1977.

Hoffmann, T., J. R. Odum, F. Bowman, D. Collins, D. Klockow, R. C. Flagan, and J. H. Seinfeld, Formation of organic aerosols from the oxidation of biogenic hydrocarbons, *J. Atmos. Chem.*, *26*, 189–222, 1997.

Hopper, J. F., D. E. J. Worthy, L. A. Barrie, and N. B. A. Trivett, Atmospheric observations of aerosol black carbon, carbon-dioxide, and methane in the high Arctic, *Atmos. Environ.*, *28*(18), 3047–3054, 1994.

Houghton, J. T., Y. Ding, D. J. Griggs, M. Noguer, P. J. van der Linden, D. Xiaosu, K. Maskell, and C. A. Johnson (Eds.), *Intergovernmental Panel on Climate Change, Climate Change 2001: The Scientific Basis*, Cambridge Univ. Press, Cambridge, U.K., 2001.

Jacobson, M. Z., A physically-based treatment of elemental carbon optics: Implication for global direct forcing of aerosols, *Geophys. Res. Lett.*, *27*(2), 217–220, 2000.

Jacobson, M. Z., Strong radiative heating due to the mixing state of black carbon in atmospheric aerosols, *Nature*, *409*(6821), 695–697, 2001a.

Jacobson, M. Z., Global direct radiative forcing due to multicomponent anthropogenic and natural aerosols, *J. Geophys. Res.*, *196*(D2), 1551–1568, 2001b.

Jacobson, M. Z., Control of fossil-fuel particulate black carbon and organic matter, possibly the most effective method of slowing global warming, *J. Geophys. Res.*, *107*(D19), 4410, doi:10.1029/2001JD001376, 2002.

Jacobson, M. Z., Climate response of fossil fuel and biofuel soot, accounting for soot's feedback to snow and sea ice albedo and emissivity, *J. Geophys. Res.*, *109*, D21201, doi: 10.1029/2004JD004945, 2004.

Janssen, N. A. H., D. F. M. VanMansom, K. VanDerJagt, H. Harssema, and G. Hoek, Mass concentration and elemental composition of airborne particulate matter at street and background locations, *Atmos. Environ.*, *31*(8), 1185–1193, 1997.

Japar, S. M., W. W. Brachaczek, R. A. B. Jr., J. M. Norbeck, and W. R. Pierson, The contribution of elemental carbon to the optical properties of rural atmospheric aerosols, *Atmos. Environ.*, *20*(6), 1281–1289, 1986.

Joshi, M., K. Shine, M. Ponater, N. Stuber, R. Sausen, and L. Li, A comparison of climate response to different radiative forcings in three general circulation models: toward an improved metric of climate change, *Clim. Dynam.*, *20*, 843–854, doi:10.1007/s00382-003-0305-9, 2003.

Kamens, R., M. Jang, C. Chien, and K. Leach, Aerosol formation from the reaction of α-pinene and ozone using a gas-phase kinetics-aerosol partitioning model, *Environ. Sci. Technol.*, *33*, 1430–1438, 1999.

Kanakidou, M., K. Tsigaridis, F. J. Dentener, and P. J. Crutzen, Human-activity-enhanced formation of organic aerosols by biogenic hydrocarbon oxidation, *J. Geophys. Res.*, *105*(D7), 9243–9254, 2000.

Kaneyasu, N., and S. Murayama, High concentrations of black carbon over middle latitudes in the North Pacific Ocean, *J. Geophys. Res.*, *105*(D15), 19,881–19,890, 2000.

Kiehl, J. T., and B. P. Briegleb, The relative roles of sulfate aerosols and greenhouse gases in climate forcing, *Science*, *260*, 311–314, 1993.

Kiehl, J. T., T. L. Schneider, P. J. Rasch, M. C. Barth, and J. Wong, Radiative forcing due to sulfate aerosols from simulations with the National Center for Atmospheric Research Community Climate Model, Version 3, *J. Geophys. Res.*, *105*(D1), 1441–1457, 2000.

Kim, Y. P., K. C. Moon, J. H. Lee, and N. J. Baik, Concentrations of carbonaceous species in particles at Seoul and Cheju in Korea, *Atmos. Environ.*, *33*(17), 2751–2758, 1999.

Kim, Y. P., K. C. Moon, and J. H. Lee, Organic and elemental carbon in fine particles at Kosan, Korea, *Atmos. Environ.*, *34*(20), 3309–3317, 2000.

Koch, D., The transport and direct radiative forcing of carbonaceous and sulfate aerosols in the GISS GCM, *J. Geophys. Res.*, *106*(D17), 20,311–20,332, 2001.

Koch, D., D. Jacob, I. Tegen, D. Rind, and M. Chin, Tropospheric sulfur simulation and sulfate direct radiative forcing in the Goddard Institute for Space Studies general circulation model, *J. Geophys. Res.*, *104*(D19), 23,799–23,822, 1999.

Lacis, A. A., and J. E. Hansen, A parameterization for the absorption of solar radiation in the earth's atmosphere, *J. Atmos. Sci.*, *31*, 118–133, 1974.

Lacis, A. A., and M. I. Mishchenko, Climate forcing, climate sensitivity, and climate response: A radiative modeling perspective on atmospheric aerosols, in *Aerosol Forcing of Climate*, edited by R. J. Charlson and J. Heintzenberg, pp. 11–42, John Wiley & Sons, New York, 1995.

Lacis, A. A., and V. Oinas, A description of the correlated k-distribution method for modeling nongray gaseous absorption, thermal emission, and multiple-scattering in vertically inhomogeneous atmospheres, *J. Geophys. Res.*, *96*(D5), 9027–9063, 1991.

Langner, J., and H. Rodhe, A global three-dimensional model of the tropospheric sulfur cycle, *J. Atmos. Chem.*, *13*, 225–263, 1991.

Lavanchy, V. M. H., H. W. Gaggeler, S. Nyeki, and U. Baltensperger, Elemental carbon (EC) and black carbon (BC) measurements with a thermal method and an aethalometer at the high-alpine research station Jungfraujoch, *Atmos. Environ.*, *33*(17), 2759–2769, 1999.

Lavoué, D., C. Liousse, H. Cachier, B. J. Stocks, and J. G. Goldammer, Modeling of carbonaceous particles emitted by boreal and temperate wildfires at northern latitudes, *J. Geophys. Res.*, *105*(D22), 26,871–26,890, 2000.

Lesins, G., P. Chýlek, and U. Lohmann, A study of internal and external mixing scenarios ans its effect on aerosol optical properties and direct radiative forcing, *J. Geophys. Res.*, *107*(D10), 4049, doi:10.1029/2001JD000973, 2002.

Li, J., E. M. Perdue, S. G. Pavlostathis, and R. Araujo, Physicochemical properties of selected monoterpenes, *Environ. Intern.*, *24*, 353–358, 1998.

Lide, D. R. (Ed.), *CRC Handbook of Chemistry and Physics*, CRC Press, Cleveland, Ohio, 2001.

Limbeck, A., and H. Puxbaum, Dependence of in-cloud scavenging of polar oranic aerosol compounds on the water solubility, *J. Geophys. Res.*, *105*(D15), 19,857–19,867, 2000.

Lindberg, J. D., R. E. Douglass, and D. M. Garvey, Atmospheric particulate absorptpion and black carbon measurement, *Appl. Opt.*, *38*(12), 2369–2376, 1999.

Liousse, C., H. Cachier, and S. G. Jennings, Optical and thermal measurements of black carbon aerosol content in different environments - variation of specific attenuation cross-section, sigma (σ), *Atmos. Environ.*, *27*(8A), 1203–1211, 1993.

Liousse, C., J. E. Penner, C. Chuang, J. J. Walton, H. Eddleman, and H. Cachier, A global three-dimensional model study of carbonaceous aerosols, *J. Geophys. Res.*, *101*(D14), 19,411–19,432, 1996.

Loew, J. A., M. H. Smith, B. M. Davison, S. E. Benson, M. K. Hill, C. D. O'Dowd, R. M. Harrison, and C. N. Hewitt, Physicochemical properties of atmospheric aerosol at South Uist, *Atmos. Environ.*, *30*(22), 3765–3776, 1996.

Lohmann, U., K. von Salzen, N. McFarlane, H. G. Leighton, and J. Feichter, Tropospheric sulfur cycle in the Canadian general circulation model, *J. Geophys. Res.*, *104*(D21), 26,833–26,858, 1999.

Luecken, D. J., C. M. Berkowitz, and R. C. Easter, Use of a three-dimensional cloud-chemistry model to study the trans-Atlantic transport of soluble sulfur species, *J. Geophys. Res.*, *96*, 22,477–22,490, 1991.

Lugauer, M., U. Baltensperger, M. Furger, H. W. Gäggeler, D. T. Jost, M. Schwikowski, and H. Wanner, Aerosol transport to the high Alpine sites Jungfraujoch (3454 m asl) and Colle Gnifetti (4452 m asl), *Tellus*, *50B*, 76–92, 1998.

Malm, W. C., M. L. Pitchford, M. Scruggs, J. F. Sisler, R. Ames, S. Copeland, K. A. Gebhart, and D. E. Day, *Spational and Seasonal Patterns and Temporal Variability of*

Haze and Its Consitutuents in the United States: Report III, Cooperative Institute for Research, Colorado State University, Fort Collins, Colorado, 2000.

Manabe, S., and R. T. Wetherald, The effects of doubling CO_2 concentration on the climate of a general circulation model, *J. Atmos. Sci.*, *32*(1), 3–15, 1975.

Markowicz, K. M., P. J. Flatau, M. V. Ramana, P. Crutzen, and V. Ramanathan, Absorbing Mediterranean aerosols lead to a large reduction in the solar radiation at the surface, *Geophys. Res. Lett.*, *29*(20), 1968, doi:10.1029/2002GL015767, 2002.

Mendonca, B. G., Local wind circulations on the slopes of mauna loa, *J. Appl. Meteorol.*, *8*, 533–541, 1969.

Menon, S., J. Hansen, L. Nazarenkk, and Y. Lup, Climate effects of black carbon aerosols in China and India, *Science*, *297*, 2250–2253, 2002.

Mickley, L. J., P. Murti, D. Jacob, J. Logan, D. Koch, and D. Rind, Radiative forcing from tropospheric ozone calculated with a unified chemistry-climate model, *J. Geophys. Res.*, *104*, 30,135–30,172, 1999.

Mickley, L. J., D. J. Jacob, B. D. Field, and D. Rind, Climate response to the increase in tropospheric ozone since preindustrial times: A comparison between ozone and equivalent CO_2 forcings, *J. Geophys. Res.*, *106*, D05106, doi:10.1029/2003JD003653, 2004.

Molnár, A., E. Mészáros, H. C. Hansson, H. Karlsson, A. Gelencsér, G. Y. Kiss, and Z. Krivácsy, The importance of organic and elemental carbon in the fine atmospheric aerosol particles, *Atmos. Environ.*, *33*(17), 2745–2750, 1999.

Myhre, G., F. Stordal, K. Restad, and I. S. A. Isaksen, Estimation of the direct radiative forcing due to sulfate and soot aerosols, *Tellus*, *50B*, 463–477, 1998.

Nenes, A., C. Pilinis, and S. N. Pandis, ISORROPIA: A new thermodynamics equilibrium model for multiphase multicomponent inorganic aerosols, *Aquat. Geochem.*, *4*, 23–152, 1998.

Noone, K. J., and A. D. Clarke, Soot scavenging measurements in Artic snowfall, *Atmos. Environ.*, *22*(12), 2773–2778, 1988.

Novakov, T., C. E. Corrigan, J. E. Penner, O. Rosario, and O. M. Bracero, Organic aerosols in the Carribean trade winds: A natural source, *J. Geophys. Res.*, *102*, 21,307–213,131, 1997.

Novakov, T., T. S. Bates, and P. K. Quinn, Shipboard measurements of concentrations and properties of carbonaceous aerosols during ACE-2, *Tellus*, *52B*(2), 228–238, 2000.

Nunes, T. V., and C. A. Pio, Carbonaceous aerosols in industrial and coastal atmospheres, *Atmos. Environ.*, *27A*(8), 1339–1346, 1993.

Nyeki, S., U. Baltensperger, I. Colbeck, D. T. Jost, E. Weingartner, and H. W. Gäaggeler, The Jungfraujoch high-Alpine research station (3454m) as a background clean continental site for the measurement of aerosol parameters, *J. Geophys. Res.*, *103*(D6), 6097–6107, 1998.

O'Dowd, C. D., M. H. Smith, and S. G. Jennings, Submicron particle, radon, and soot carbon characterstics over the northeast Atlantic, *J. Geophys. Res.*, *98*(D1), 1123–1135, 1993.

Odum, J. R., T. P. W. Jungkamp, R. J. Griffin, R. C. Flagan, and J. H. Seinfeld, The atmospheric aerosol-forming potential of whole gasoline vapor, *Science*, *276*, 96–99, 1997.

Ohta, S., and T. Okita, Measurements of particulate carbon in urgan and marine air in Japanese areas, *Atmos. Environ.*, *18*(11), 2439–2445, 1984.

Ohta, S., and T. Okita, A chemical characterization of atmospheric aerosols in Sapporo, *Atmos. Environ.*, *24A*(4), 815–822, 1990.

Pandis, S. N., S. E. Paulson, J. H. Seinfeld, and R. C. Flagan, Aerosol formation in the photooxidation of isoprene and β-pinene, *Atmos. Environ.*, *25A*, 997–1008, 1991.

Pankow, J. F., An absorption model of gas/particle partitioning of organic compounds in the atmosphere, *Atmos. Environ.*, *28*(2), 185–188, 1994a.

Pankow, J. F., An absorption mdoel of gas/particle partitioning involved in the formation of secondary organic aerosol, *Atmos. Environ.*, *28*(2), 189–193, 1994b.

Parungo, F., C. Nagamoto, M. Zhou, A. Hansen, and J. Harris, Aeolian transport of aerosol black carbon from China to the ocean, *Atmos. Environ.*, *28*(20), 3251–3260, 1994.

Penner, J. E., H. Eddleman, and T. Novakov, Towards the development of a global inventory for black carbon emissions, *Atmos. Environ.*, *27A*, 1277–1295, 1993.

Penner, J. E., C. A. Atherton, and T. E. Graedel, Global emissions and models of photochemically active compounds, in *Global Atmospheric-Biospheric Chemistry*, edited by R. Prinn, pp. 223–248, Plenum, New York, 1994.

Penner, J. E., T. Wigley, P. Jaumann, B. Santer, and K. Taylor, Anthropogenic sulfate aerosols and climate change: A method for calibrating forcing, in *Communicating About Climate: The Story of the Model Evaluation Consortium for Climate Assessment*, edited by W. Howe and A. Henderson-Sellers, pp. 91–111, Gordon and Breach Science Publishing, Sydney, 1997.

Penner, J. E., C. C. Chuang, and K. Grant, Climate forcing by carbonaceous and sulfate aerosols, *Clim. Dynam.*, *14*, 839–851, 1998.

Pham, M., J. F. Müller, G. P. Brasseur, G. Granier, and G. Megie, A 3d model stuy of the global sulfur cycle: Contributions of anthropogenic and biogenic sources, *Atmos. Environ.*, *30*, 1815–1822, 1996.

Piccot, S. D., J. J. Watson, and J. W. Jones, A global inventory of volatile organic compound emissions from anthropogenic sources, *J. Geophys. Res.*, *97*, 9897–9912, 1992.

Pinnick, R. G., G. Fernandez, E. Martinezandazola, B. D. Hinds, A. Hansen, and K. Fuller, Black carbon content and vertical structure to 7 km above sea-level, *J. Geophys. Res.*, *98*(D2), 2651–2666, 1993.

Pio, C. A., L. M. Castro, M. A. Cequeira, I. M. Santos, F. Belchior, and M. L. Salqueiro, Source assessment of particulate air pollutants measured at the southern European coast, *Atmos. Environ.*, *30*(19), 3309–3320, 1996.

Polissar, A. V., Surface-level carbon-containing aerosol concentration in the North Atlanticn, *Izv. Acad. Sci. USSR Atmos. Oceanic Phys. Engl. Transl.*, *28*(7), 520–525, 1992.

Polissar, A. V., Measurements of the soot mass concentration and particle-size distribution of the atmospheric aerosol in the eastern Arctic, *Izv. Acad. Sci. USSR Atmos. Oceanic Phys. Engl. Transl.*, *29*(1), 66–73, 1993.

Polissar, A. V., P. K. Hopke, P. Paatero, Y. J. Kaufmann, D. K. Hall, B. A. Bodhaine, E. G. Dutton, and J. M. Harris, The aerosol at Barrow, Alaska: long-term trends and source locations, *Atmos. Environ.*, *33*(16), 2441–2458, 1999.

Prather, M. J., Numerical advection by conservation of second-order moments, *J. Geophys. Res.*, *91*(D6), 6671–6681, 1986.

Puxbaum, H., J. Rendl, R. Allabashi, L. Otter, and M. C. Scholes, Mass balance of the atmospheric aerosol in a south african subtropical savanna (Nylsvley, May 1997), *J. Geophys. Res.*, *105*(D16), 20,697–20,706, 2000.

Ramanathan, V., P. J. Crutzen, J. T. Kiehl, and D. Rosenfeld, Aerosols, climate, and the hydrological cycle, *Science*, *294*(5549), 2119–2124, 2001a.

Ramanathan, V., P. J. Crutzen, J. Lelieveld, A. P. Mitra, D. Althausen, J. . Anderson, M. O. Andreae, W. Cantrell, G. R. Cass, C. E. Chung, A. D. Clarke, J. A. Coakley, W. D. Collins, W. C. Conant, F. Dulac, J. Heintzenberg, A. J. Heymsfield, B. Holben, S. Howell, J. Hudson, A. Jayaraman, J. T. Kiehl, T. N. Krishnamurti, D. Lubin, G. McFarquhar, T. Novakov, J. A. Ogren, I. A. Podgorny, K. Prather, K. Priestley, J. M. Prospero, P. K. Quinn, K. Rajeev, P. Rasch, S. Rupert, R. Sadourny, S. K. Satheesh, G. E. Shaw, P. Sheridan, and F. P. J. Valero, Indian Ocean Experiment: An integrated analysis of the climate forcing and effects of the great Indo-Asian haze, *J. Geophys. Res.*, *106*(D22), 28,371–28,398, 2001b.

Rasch, P. J., M. C. Barth, J. T. Kiehl, S. E. Schwartz, and C. M. Benkovitz, A description of the global sulfur cycle and its controlling processes in the National Center for Atmospheric Research Community Climate Model, Version 3, *J. Geophys. Res.*, *105*(D1), 1367–1385, 2000.

Raunemaa, T., K. Kuuspalo, T. Alander, E. Tamm, A. Mirme, and V. Laine, Black carbon and aerosol in Boistö island, *J. Aerosol Sci.*, *24*, S29–S30, 1993.

Raunemaa, T., U. Kikas, and T. Bernotas, Observation of submicron aerosol, black carbon and visibility degradation in remote area at temperature-range from -24 to 20-degrees-C, *Atmos. Environ.*, *28*(5), 865–871, 1994.

Rind, D., and J. Lerner, Use of on-line tracers as a diagnostic tool in general circulation model development: 1. horizontal and vertical transport in the troposphere, *J. Geophys. Res.*, *101*, 12,667–12,683, 1996.

Roberts, D. L., and A. Jones, Climate sensitivity to black carbon aerosol from fossil fuel combustion, *J. Geophys. Res.*, *109*, D16202, doi:10.1029/2004JD004676, 2004.

Roelofs, G. J., J. Lelieveld, and L. Ganzeveld, Simulation of global sulfate distribution and the influence on effective cloud drop radii with a coupled photochemistry sulfur cycle model, *Tellus*, *50B*(3), 224–242, 1998.

Ruellan, S., H. Cachier, A. Gaudichet, P. Masclet, and J.-P. Lacaux, Airborne aerosols over central Africa during the experiment for regional sources and sinks of oxidants (EXPRESSO), *J. Geophys. Res.*, *104*(D23), 30,673–30,690, 1999.

Russell, G. L., J. R. Miller, and L.-C. Tsang, Seasonal ocean heat transports computed from an atmospheric model, *Dynam. Atmos. Oceans*, *9*, 253–271, 1984.

Sander, R., Compilation of Henry's law constants for inorganic and organic species of potential importance in environmental chemistry (version 3), http://www.mpch-mainz.mpg.de/ sander/res/henry.html, 1999.

Saxena, P., and L. M. Hildemann, Water-soluble organics in atmospheric particles: A critical review of the literature and application of thermodynamics to identify candidate compounds, *J. Atmos. Chem.*, *24*, 57–109, 1996.

Schult, I., J. Feichter, and W. F. Cooke, Effect of black carbon and sulfate aerosols on the global radiation budget, *J. Geophys. Res.*, *102*(D25), 30,107–30,117, 1997.

Seinfeld, J. H., G. B. Erdakos, W. E. Asher, and J. F. Pankow, Modeling the formation of secondary organic aerosol (SOA). 2. the predicted effects of relative humidity on aerosol formation in the α-pinene-, β-pinene-, sabinene-, Δ^3-carene-, and cyclohexene-ozone systems, *Environ. Sci. Technol.*, *35*, 1806–1817, 2001.

Shine, K. P., and P. Forster, The effect of human activity on radiative forcing of climate change: a review of recent developments, *Global and Planetary Change*, *20*, 205–225, 1999.

Shu, Y., and R. Atkinson, Atmospheric lifetimes and fates of a series of sesquiterpenes, *J. Geophys. Res.*, *100*, 7275–7281, 1995.

Smith, D. J. T., R. M. Harrison, L. Luhana, C. A. Pio, L. M. Castro, M. N. Tariq, S. Hayat, and T. Quraishi, Concentrations of particulate airborne polycyclic aromatic hydrocarbons and metals collected in Lahore, Pakistan, *Atmos. Environ.*, *30*(23), 4031–4040, 1996.

Taylor, K. E., and J. E. Penner, Response of the climate system to atmospheric aerosols and greenhouse gases, *Nature*, *369*, 734–737, 1994.

Tegen, I., D. Koch, A. A. Lacis, and M. Sato, Trends in tropospheric aerosol loads and corresponding impact on direct radiative forcing between 1950 and 1990: A model study, *J. Geophys. Res.*, *105*(D22), 26,971–26,989, 2000.

Toon, O. B., J. B. Pollack, and B. N. Khare, The optical constants of several atmospheric aerosol species: Ammonium sulfate, aluminum oxide, and sodium chloride, *J. Geophys. Res.*, *81*, 5733–5748, 1976.

Turpin, B. J., P. Saxena, and E. Andrews, Measuring and simulating particulate organics in the atmosphere: Problems and prospects, *Atmos. Environ.*, *34*, 2983–3031, 2000.

Wang, C., A modeling study on the climate impact of black carbon aerosols, *J. Geophys. Res.*, *109*, D03106, doi:10.1029/2003JD004084, 2004.

Wang, S., S. E. Paulson, D. Grosjean, R. C. Flagan, and J. H. Seinfeld, Aerosol formation and growth in atmospheric organic/NO_x systems–I. Outdoor smog chamber studies of C_7- and C_8-hydrocarbons, *Atmos. Environ.*, *26A*, 403–420, 1992.

Wang, Y., D. J. Jacob, and J. A. Logan, Global simulation of tropospheric O_3-NO_x-hydrocarbon chemistry: 1. model formulation, *J. Geophys. Res.*, *103*, 10,713–10,725, 1998a.

Wang, Y., J. A. Logan, and D. J. Jacob, Global simulation of tropospheric O_3-NO_x-hydrocarbon chemistry: 2. model evaluation and global ozone budget, *J. Geophys. Res.*, *103*, 10,727–10,755, 1998b.

Wang, Y., J. A. Logan, and D. J. Jacob, Global simulation of tropospheric O_3-NO_x-hydrocarbon chemistry: 3. origin of tropospheric ozone and effects of nonmethane hydrocarbons, *J. Geophys. Res.*, *103*, 10,757–10,767, 1998c.

Wesely, M. L., Parameterization of surface resistances to gaseous dry deposition in region-scale numerical models, *Atmos. Environ.*, *23*, 1293–1304, 1989.

Wesely, M. L., and B. B. Hicks, Some factors that affect the deposition rates of sulfur dioxide and similar gases in vegetation, *J. Air Pollut. Contr. Assoc.*, *27*, 1110–1116, 1977.

Wolff, E. W., and H. Cachier, Concentrations and seasonal cycle of black carbon in aerosol at a coastal Antarctic station, *J. Geophys. Res.*, *103*(D9), 11,033–11,041, 1998.

Wolff, G. T., M. S. Ruthkosky, D. P. Stroup, P. E. Korsog, M. A. Ferman, G. J. Wendel, and D. H. Stedman, Measurements of SO_x, NO_x, and aerosol species on Bermuda, *Atmos. Environ.*, *20*(6), 1229–1239, 1986.

Yaaqub, R. R., T. D. Davies, T. D. Jickells, and J. M. Miller, Trace-elements in daily collected aerosols at a site in southeast England, *Atmos. Environ.*, *45A*, 985–996, 1991.

Yu, J. Z., D. R. Cocker, R. J. Griffin, R. C. Flagan, and J. H. Seinfeld, Gas-phase ozone oxidation of monoterpenes: Gaseous and particulate products, *J. Atmos. Chem.*, *34*(2), 207–258, 1999.

Zappoli, S., A. Andracchio, S. Fuzzi, M. . C. Facchini, A. Gelencsér, G. Kiss, Z. Krivácsy, Á. Molnár, E. Mészáros, H.-C. Hansson, K. Rosman, and Y. Zebühr, Inorganic, organic, and macromolecular components of fine aerosols in different areas of Europe in relation to their water solubility, *Atmos. Environ.*, *33*, 2733–2743, 1999.

Zwiers, F. W., and H. von Storch, Taking serial correlation into account in tests of the mean, *J. Clim.*, *8*, 336–351, 1995.